PHD

Positron Studies of Defects in Thin Films and Semiconductors

Edwardson, Charlene

Award date:
2013

Awarding institution:
University of Bath

Positron Studies of Defects in Thin Films and Semiconductors

Charlene Joanne Edwardson

A thesis submitted for the degree of Doctor of Philosophy

University of Bath

Department of Physics

March 2013

Table of Contents

To my family

Acknowledgments

I would like to express my thanks to the following people, who made the completion of this thesis possible.

To my supervisor Prof. Paul Coleman, whose guidance, support, humour and kindness has made it such a great honour to work with him. He has taught me about many important things, like how to solve cryptic crosswords. I aspire to be just half the person he is.

In the Bath positron group I'd like to thank Dr. Alexis Kallis and Dr. Sam Townrow for their advice and help, and honorary member Harry Bone BSc for his support and unique humour.

To everyone I have collaborated with over the past three years, your expertise and help was invaluable. For their work on oxide films I'd like to thank Dr. David Keeble, Dr. Andrew Li, Prof. Andres Cuevas, Dr. Simon Ruffell, Anbang Zhang, Xiangyang Ma, Dr. Xiaodong Pi and Prof. Deren Yang. For their work on semiconductors I'd like to thank Dr. Andrew Knights, Deborah Nash, Prof. Russell Gwilliam, Dr. Kei Takashina, David Tregurtha, Dr. A. Fujiwara, Dr. Huda El Mubarek, Dr. Amy Gandy, D. J. Paez, J. K. Doylend, J D B Bradley, O Hulko, D V Stevanovic, Dr. I F Crowe and Prof. M P Halsall. For their work on the other materials in this thesis I'd like to thank Dr. Michael Grogan, Prof. Timothy Birks, Dr. Alexander Romanenko and Prof. Peter Simpson.

Eternal thanks to Peter and Brian Moreton for all their love and support. Thanks to my friends, particularly Richard Gaisford and Rachael Ward. Finally, I would like to thank the Nanoscience and Underwater Acoustics Social Group for their friendship.

Abstract

Positron studies of defects in thin films and semiconductors are reviewed. The results obtained from experimental studies of Doppler broadening of annihilation radiation (DBAR) from variable energies are presented. Normalisation methods for the DBAR parameters *S* and *W* have been developed, allowing for direct comparisons of the results for different samples taken over long periods of time. The evaluation of the *P*:*V* parameter, the peak-to-valley ratio in a full annihilation spectrum, has been improved via a correction method that produced a fourfold increase in sensitivity to o-Ps annihilation. The spectrum ratio curve technique was improved and developed to investigate the chemical composition of the environment surrounding a positron-trapping defect. By fitting to multiple-element and/or defect-type responses the percentage of that particular element or defect contained within the sample could be found. Ratio curves were found to rely on the positron affinity to different vacancy types. Beam-based Doppler broadening spectroscopy, variable-energy positron annihilation spectroscopy (VEPAS), was used as a probe of oxide film and film/substrate interface characteristics. Different film growth methods were found to play a significant role in defining the features of films and their interfaces. Vacancies have a profound effect on the properties of semiconductor-type devices. A range of different structures and the effects of implantation have been investigated. VEPAS has been found to be useful in studying the more exotic types of materials, silica aerogel and niobium.

Chapter 1

Introduction

"So perhaps the best thing to do is to stop writing Introductions and get on with the book."

- A.A. Milne, Winnie-the-Pooh

Even simple atomic defects can contribute to the many physical processes and macroscopic properties of a material. In both elemental and compound semiconductors, atomic defects can be electrically active and consequently strongly affect electrical and optical properties in addition to the desired dopant effects.[1] Device fabrication processes such as doping via ion implantation can create many point defects.[1] Studying these atomic structures and the electronic properties of point defects is essential in the development of semiconductor materials for device applications.

There are several methods currently used to study small vacancy defects. One such technique is Electron Spin Resonance (ESR). An F-Centre (or colour centre) is a type of defect in which a missing negative ion in a crystal (such as a missing Cl^- ion in KCl) is filled by one or more unpaired electrons (depending on the charge of the missing ion) to create charge neutrality. Colour changes occur when a photon is absorbed, exciting these electrons into states in the band gap created as a result of the defect. When an external magnetic field is applied the states are split, due its paramagnetism and the Zeeman Effect, so the unpaired electrons can move between either state by absorbing or emitting a photon. This can then be studied by ESR techniques. Limitations of this technique are that it can only be used to study bulk (homogeneous) materials that contain paramagnetic defects.[2] Another technique is High-Resolution Transmission Electron Microscopy (HRTEM). It is similar to TEM in that an image is formed through the interaction of the electrons with the sample, but measures the interference pattern created by the electrons which is the Fourier transform of the periodic potential. Individual atoms and crystalline defects can be imaged but the technique has various limitations. It is destructive - due to the high magnification imaging requiring a high electron dose; by itself it provides very limited chemical information, and it is relatively slow

and difficult, requiring intricate specialist equipment and highly-trained operators.[3] One other technique to study vacancies is Deep Level Transient Spectroscopy (DLTS). DLTS uses the capacitance of a p-n junction or Schottky barrier as a probe to monitor the changes in the charge state of nonradiative centers. The DLTS technique has a higher sensitivity than almost any other semiconductor diagnostic technique but it is destructive, limited to charged defects and only works with very low defect concentrations.[4] Optical microscopy, x-ray scattering, regular TEM, neutron scattering, X-ray scattering and photoluminescence are also all used to study point defects, but typically (although not always) these are interstitial-type, mainly in bulk materials and usually for large (> few nm) cavities. Some can also be destructive.

In defect physics, positron annihilation is used as a spectroscopic tool to study vacancies in semiconductors, metals and alloys. Positron spectroscopy is a non-destructive technique which is highly sensitive to near-surface vacancies, and can provide semi-quantitative information on defect depth profiles. It does have limitations in that it is only sensitive to negative and neutral vacancies and the results obtained with the form of spectroscopy described below are sensitive to both defect size and concentration, thus requiring prior knowledge if these are to be separated. The positron technique is the basis for this thesis and will be investigated in further detail.

The existence of positrons was first predicted by Dirac in the early 1930s as a result of developing his quantum theory of the electron.[5] The theory allowed states of negative kinetic energy as well as the usual states of positive kinetic energy (from $E = \pm mc^2$) and also allowed transitions from one kind of state to the other. Particles in states of negative kinetic energy had never been observed in practice. To overcome this Dirac theorised that nearly all the states of negative kinetic energy were occupied, with one electron in each state in accordance with Pauli's exclusion principle, and thought it would be unobservable due to its uniformity. Any unoccupied states however, would be observable as holes and appear as positively charged particles. Such particles were originally assumed to be protons. Dirac realised soon after that this was incorrect since it was found that the holes must correspond to particles with the same rest-mass as electrons.

The discovery of the positron followed shortly after in 1933 when Anderson was photographing cosmic-ray tracks produced in a vertical Wilson "cloud" chamber. Tracks were obtained with a curvature which could only be explained by a positively charged

particle having a mass with the same order of magnitude as an electron, the recently predicted positron.[6]

In positron physics, there are three main types of techniques used to study materials. These are annihilation lifetime, angular correction of annihilation radiation (ACAR) and Doppler broadening. Annihilation lifetime measures the time between when a positron is first created and when it annihilates, which is characteristic of the type of material probed and can give an indication of the size of open volume defects in the material; a longer lifetime usually associated with larger voids. ACAR measures the small deviation from π radians in the angle between two annihilation gamma rays. This method measures directly the electron momentum, looking at Fermi surfaces with high resolution.

For the research described in this thesis, the Doppler broadening technique is used. If a positron and electron pair in a singlet spin state are at rest, the two gamma-rays produced in their annihilation would each have an energy of 511 keV with an angle between them of π radians. However, when in matter there is a centre of mass motion which creates a Doppler shift in the gamma-ray energies. Thermalisation of positrons in matter before annihilation means that this momentum is mostly that of the electron as a result of the Pauli exclusion principle. Measuring this shift in momentum gives an indication of the environment in which the electron annihilated, including open volume defect size and concentration and the chemical environment. Positrons can be used as a probe of defects due to the nature of these open volume vacancies.

This thesis explores various ways that the Doppler broadening technique can be used. After an introduction to the theory of slow positron beams the methods associated with the technique are described. These techniques, having been developed or improved, are used to investigate oxide films and vacancies in silicon-type structures as well as other more exotic materials.

[1] A. Dupasquier and A. P. Mills Jr. (ed.), Positron Spectroscopy of Solids. IOS Press (1995).

[2] S. A. Altshuler and B. M. Kozirev, Electron Paramagnetic Resonance. New York: Academic Press. (1964).

[3] D.J. Smith, Reports Prog. Phys., 1513 (1997).

[4] D. V. Lang, J. Appl. Phys. **45**, 3023 (1974).

[5] P. A. M. Dirac, Discussion of the infinite distribution of electrons in the theory of the positron. Mathematical Proceedings of the Cambridge Philosophical Society **30**, 150 (1934).

[6] C. D. Anderson, Phys. Rev. **43**, 491 (1933).

Chapter 2

Theory and Experimental Principles

"If the facts don't fit the theory, change the facts."

- Albert Einstein

2.1 The positron and positronium

The positron is the antiparticle of the electron, in that it has the same mass (511 keV/c^2), spin (1/2), and the same magnitude of electric charge, though with the opposite sign. In a vacuum it is stable, having the same lifetime as an electron. When in normal matter the positron will thermalise in (1-3) ps at 300K, a much shorter time than a typical positron lifetime of (100-200) ps.[1, 2] In semiconductors this process mainly occurs via phonon scattering.[3] When a positron reaches thermal energies, it will start to diffuse through the lattice and behave like a positively charged particle. The positron eventually annihilates with an electron after traversing an effective diffusion length L_{eff} influenced by crystal defects and electric fields

$$L_{eff} = \frac{1}{\sqrt{\frac{\lambda_{eff}}{D_+} + \left(\frac{eE_{drift}}{2k_BT}\right)^2 - \frac{e|E_{drift}|}{2k_BT}}} \tag{2.1}$$

where E_{drift} is the electric field strength, e the elementary charge, k_B the Boltzmann constant, T the temperature, and D_+ the positron diffusion constant given by

$$D_+ = \tau_r \frac{k_BT}{m^*} \tag{2.2}$$

where τ_r is the relaxation time for the dominant scattering mechanism and m^* is the effective positron mass (which is different from the rest mass because of phonon scattering, screening by electrons and the effect of a periodic lattice[4]); λ_{eff} is the effective annihilation rate given by

$$\lambda_{eff} = \frac{1}{\tau_b} + \kappa(\underline{r}) \tag{2.3}$$

where τ_b is the mean lifetime of positrons in a defect-free bulk material and $\kappa(\underline{r})$ is the positron trapping rate.[2] Note that in the absence of an electric field to drift the positrons equation (1) simplifies to $L_{eff} = [D_+/\lambda_{eff}]^{1/2}$.

Annihilation of the positron and electron can occur via a number of mechanisms, the most probable of which is when the positron and electron are in a singlet spin state resulting in two-gamma-ray annihilation. In certain situations when the positron has thermalised in an area of low local electron density, such as at surfaces, in voids or in the bulk of insulators and polymers, there is a chance to form positronium. Positronium is a hydrogen-like quasi-stable neutral bound state of an electron and a positron. It can exist in the two spin states, $S = 0, 1$. Positronium in a ground state with spin S and orbital angular momentum $L = 0$ can only annihilate into n gamma rays where

$$(-1)^n = (-1)^{L+S}. \tag{2.4}$$

The singlet state ($^1S_0$), called para-positronium (p-Ps), occurs when the electron and positron spins are antiparallel. This state has a vacuum lifetime of ~125 ps, primarily decaying into two gamma rays of 511 keV.

The triplet state ($^3S_1$), called ortho-positronium (o-Ps), occurs when the electron and positron spins are parallel. o-Ps has a vacuum lifetime of ~142 ns. This state primarily decays into three gamma rays, usually comprising of two gamma rays just below 511 keV and another much smaller, although any continuous energy distribution up to 511 keV is possible.[5] With one possible state for p-Ps and three possible for o-Ps in general there is a 3:1 ratio of o-Ps to p-Ps formation in the absence of quenching.[6]

An individual vacancy is the deficiency of one positive ion core, which usually constitutes an attractive potential well for positrons. If the vacancy is negatively-charged the deep potential well efficiently traps positrons, increasing the probability that the positron will annihilate with conduction or valence electrons and decreasing the chance of annihilation with inner-shell core electrons.[7] The net charge of a vacancy in a semiconductor however is not always negative. By superimposing the square-well potential on a long-range Coulomb potential additional repulsion or attraction is created in the vacancy[8]:

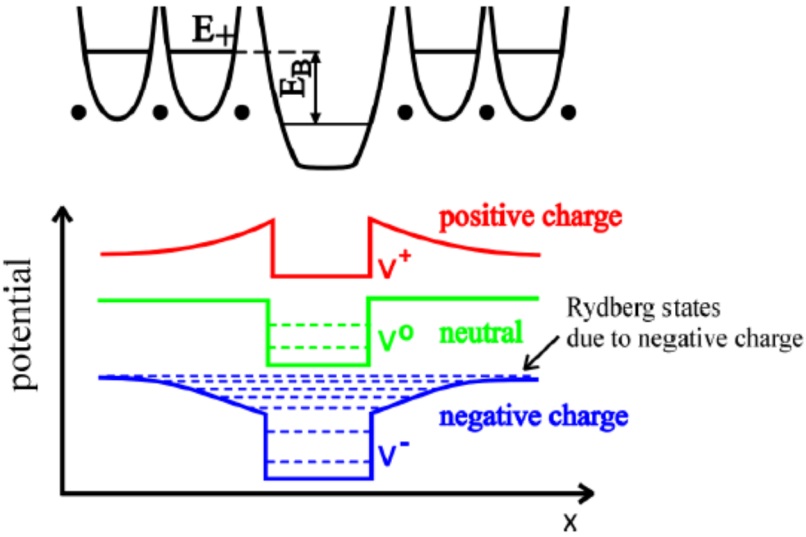

Figure 2.1.1: Scheme of the positron potential for negative V^-, neutral V^0 and positive V^+ vacancies in a semiconductor where E_B is the positron binding energy (E_+) in the trap.

Positively charged vacancies cannot effectively trap positrons during their lifetime in a semiconductor. For neutral vacancies the dominant trapping mechanism is found to be electron excitation from a localised state at the vacancy to the conduction band. The negatively charged vacancy's attractiveness is enhanced by the occurrence of extended Rydberg states induced by the long range Coulomb potential. These states trap the positron in a more extended volume compared with a neutral vacancy.[2]

2.2 Slow Positron Beam

Over the past forty five years the development of positron beams has improved greatly as an experimental technique. Positron beam spectroscopy is now used all over the world in many different scientific areas.[9]

Modifying the Doppler broadening technique by controlling the depth to which the positrons are implanted gives a depth profile of the material. This technique is called variable energy positron annihilation spectroscopy (VEPAS) and its methodology will now be discussed.

Fig. 2.2.1 shows the entire magnetic-transport positron beam system used throughout this work at the University of Bath to perform VEPAS.

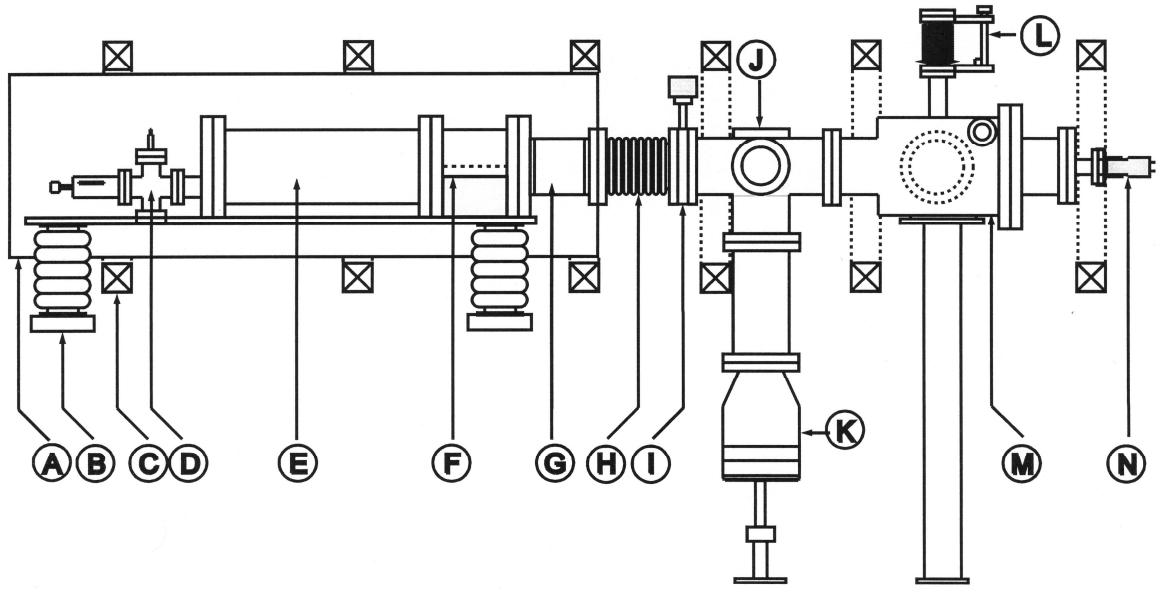

*Figure 2.2.1: A magnetic-transport positron beam system. A-Grounded shield; B-Standoff insulators; C-Helmholtz coils; D-^{22}Na source and W moderator; E-**E**x**B** plates; F-Lead shielding; G-Accelerator; H-Bellows; I-Aperture; J-Trim coils; K-Turbo pump; L-Sample manipulator; M-Sample chamber and HPGe detector; N-CEMA plates and CCD camera.*

Positron source

Positrons can be produced either through the beta decay of radioactive isotopes or by pair production. The source of choice here is ^{22}Na for its balance of long half-life (2.6 y) and cost per Bq. To maximise the beta positron output the source capsule has a backing made of a high-Z material, backscattering positrons in the forward direction. Positrons are emitted from this source with a large continuous energy spectrum, extending to 0.54 MeV. A variable-energy, monoenergetic beam can be achieved through moderation.

Moderator

When a beta positron enters a metal with an energy greater than a few keV it will reach thermal equilibrium with its surroundings (~40 meV) in ~1 ps at 300 K. The average distance travelled by a diffusing thermalised positron in its lifetime (~150 ps) is L_+ (~100 nm). If the positron thermalises within L_+ from the surface then there is a possibility of diffusion back to it. The probability of this occurring can be increased if the moderating material contains no open volume defects to trap the diffusing positrons. Once the positron has reached the surface it can then either fall into the surface well and eventually annihilate, pick up an electron and leave as positronium or, ideally for a moderator, leave as a free positron into the vacuum with

an energy determined by the positron work function φ_+, as long as φ_+ is negative. φ_+ is defined as the minimum energy required to remove a positron from a point inside to one far from the surface. For different materials φ_+ has a range of values about zero. It is a balance between the repulsive surface dipole *D*, arising from the spilling of electrons into the vacuum, and the attractive correlation potential V_{CORR} from conduction electrons. This can be seen schematically in Fig. 2.2.2 where V_0 is the repulsive interaction with ion cores (black disks).[4]

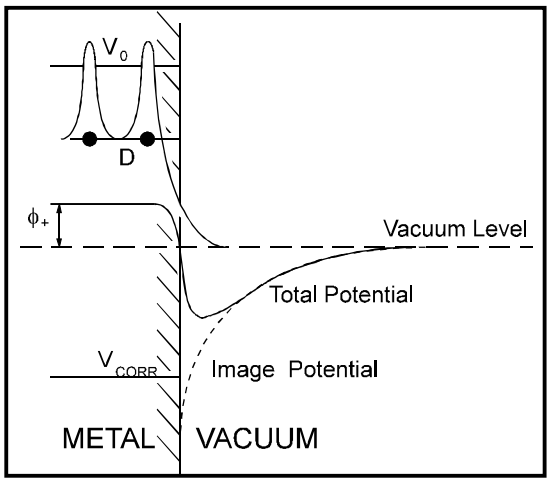

Figure 2.2.2: The single-particle potential for a thermalised positron in a metallic lattice.[4]

The moderator used here is made from a tungsten mesh as tungsten has a relatively high negative φ_+ of ~ 2.7 eV. The mesh is annealed to remove defects that otherwise would trap the positrons and so reduce its efficiency. It can also be re-annealed in situ to improve its moderation efficiency further. A small potential (10 V) applied between the mesh and the source ensures that positrons leaving the irradiated back side of the moderator are turned away from the source, back through the mesh, into the beam line.

Transport

The 1 in 10^4 positrons/sec surviving the moderation (~$2x10^4$ positrons/sec) are then transported from the moderator to their target through a series of quasi-Helmholtz coils and ***E*x*B*** filters.[10] The coils are used to control the transverse momentum of the positrons while the ***E*x*B*** filters remove fast positrons from the beam and shield the detector from the positron source, the principle of which will now be discussed. An electrostatic field ***E*** applied in a direction perpendicular to that of the axial magnet field ***B*** causes the positrons to drift up with a constant drift velocity (*E/B*) in the direction of ***E*x*B***. The deflection distance $y = (E/B) \times (L/v_z)$ where v_z is the constant axial speed of the positrons as seen in Fig. 2.2.3.

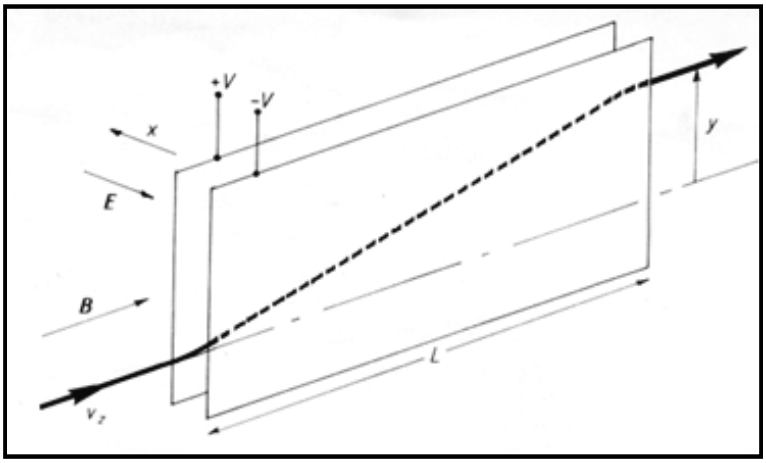

*Figure 2.2.3: Planar-geometry **E**x**B** filter.*[11]

The displacement through the plates is therefore inversely proportional to the positrons' momentum, and the eV positrons experience a deflection orders of magnitude greater than that of unmoderated positrons. In the usual ***E***x***B*** filter the electric field is produced by two planar electrodes at potential ±*V* so chosen that a positron entering the filter midway between the two plates has no longitudinal acceleration. However distortion of the beam profile arises in this system because the typical beam diameter (4-10 mm) is not negligible compared to the plate separation. The potential gradient across the beam produces a spread in longitudinal velocities and, in consequence, a spread Δ*y* in the deflections *y* (Fig. 2.2.4.a). To overcome this problem cylindrical plate geometry is used (Fig. 2.2.4.b).[10] Longitudinal momentum dispersion is still present but the accelerating negative potential is applied to the electrode with smaller radius so that the faster positrons are in a higher electric field, in which their higher transverse velocity can compensate for their shorter transit time.

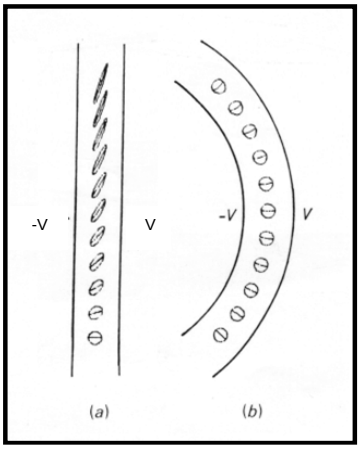

*Figure 2.2.4: Progressive distortion of positron beam profile passing through planar (a) and cylindrical-geometry (b) **E**x**B** plates.*[11]

The eV positrons are transported to the sample chamber through an aperture at the top of the plates while the unmoderated positrons are annihilated at a shielded barrier.

Acceleration

Once the positrons have passed through the velocity filter they then have an accelerating potential applied. A potential is applied between two plates separated by ten discrete smooth metallic rings. The rings are resistively connected to force equipotential differences between adjacent rings. The potential applied can be varied between 0.5 and 30 keV where the source/moderator end of the beam is raised to the accelerating potential and the sample chamber end is at ground. Positrons are accelerated with an incident energy E (keV) into a sample and scatter off the electrons and ion cores eventually becoming thermalised with a characteristic implantation profile $P(z,E)$. The motion of thermal positrons, before eventual trapping into a defect site or annihilating from an unlocalised bulk state, is described by a diffusion equation.[12] The positron implantation profile for the monoenergetic positron beam in a semi-infinite solid can be expressed by the derivative of a Gaussian, which in general terms is described by the Makhovian profile[13, 14]

$$P(z,E) = \frac{m z^{m-1}}{z_0^{\,m}} . e\left[-\left(\frac{z}{z_0} \right)^m \right] \tag{2.5}$$

where m is an adjustable parameter, usually taken as 2. z_0 is a material dependent parameter, depending on density and implantation energy E:

$$z_0(nm) = \frac{40}{\rho(g/cm^3)} . E(keV)^n \tag{2.6}$$

where n is usually taken as 1.6. Fig. 2.2.5 shows this profile at various energies in Si. The mean implantation depth $\bar{z}(nm)$ calculated from Monte Carlo simulations[15] is similar to that in Eqn. 2.6:

$$z_0(nm) = \frac{33}{\rho(g/cm^3)} . E(keV)^{1.6} \tag{2.7}$$

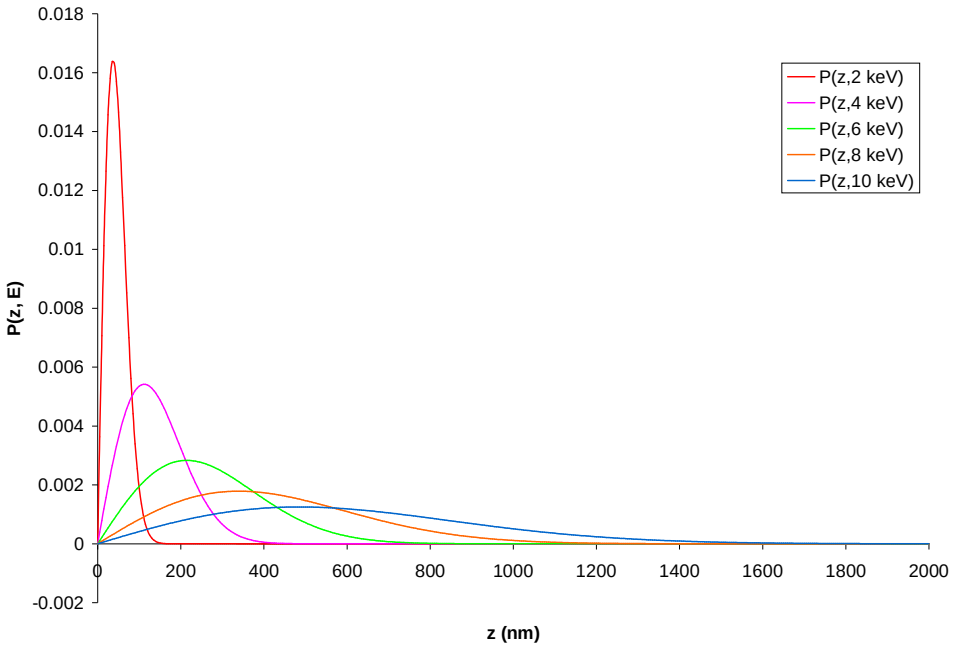

Figure 2.2.5: Implantation profiles for various positron energies in Si

The resolution of the positron beam is effectively increased at lower implantation energies because the positrons are implanted in more localised regions. At higher energies this implantation region covers a wider area.

Sample Chamber

Samples are placed in a high vacuum chamber that can reach pressures of below ~10^{-7} Torr. The chamber can be cut off from the rest of the beam by a gate valve allowing the high voltage end to remain at vacuum. A sample is mounted on a holder that can be manipulated in the *x* and *y* directions with micrometers. The samples are supported thin (~ 0.1mm diameter) tungsten wires so the positron beam essentially hits only the sample. Channel electron multiplier arrays (CEMAs)[9] are used to obtain an image of the positron beam. They consist of arrays of ~10^{1} μm diameter tubes ~500 μm long, with a maximum effective open area of ~70%. Two of these CEMA plates, each with ~10^{4} gain, in series, with 1 kV across each are used. This plate assembly is then held in front of a phosphor screen with an additional 2 kV acceleration potential between, which is viewed by a camera. Not only does this help to correctly position the sample, it is also used to correct for focusing and off-axis shift effects.[16]

Focusing effects occur when the positron beam energy is increased or decreased causing the beam to go in and out of focus with a shrinking and expanding diameter. At certain energies the beam is seen as a distinct circle of a similar size to the aperture that shaped the incoherent beam after moderation and determines the relative phases of the individual positron paths at that point. When in a magnetic field a positron will follow a helical path down the line of travel of the beam. The focused condition occurs when all of the individual positron helices have undergone an integer number of complete periods between the aperture and detector. Maintaining a focused beam at the sample position is possible by adjusting the intensity of the guiding magnetic field for each value of ***E***; however this would result in secondary unwanted consequences such as changes in ***ExB*** deflections. The only consequential effect of the focusing effect of the positron beam is the beam's diameter. A larger spot size could result in positrons missing the sample but the average sizes of the samples are large enough for this not to be an issue. Focusing the beam is only used to image the sample itself for positioning purposes. It can be shown that, for a charged particle moving in an axial magnetic field which varies slowly along the axis,

$$\left(\sin^2 \alpha\right)/ B = a\ const. \tag{2.8}$$

where α is the angle pitch of the helical trajectory.[17] Therefore, a solenoid is used between the sample chamber and the CEMA to apply a variable ***B*** field to change the pitch of the positron's helical motion, focusing the beam.

Off-axis shifts occur as the energy ***E*** is increased, causing the beam to move in small spirals about a centre point. As the energy is increased further the radius of the spiral increases to a point where the beam may completely miss the sample. An ***ExB*** field effect would usually push the beam off in one direction only. It is difficult to explain why, in this case, the beam is seen to spiral about a centre point. Chilton and Coleman[16] theorise that as the acceleration energy is increased, the effective length of the accelerator is increased by end effects. As the magnetic field is not uniform (because of the distinct coils) the ***ExB*** vector may change with energy and so produce such a motion. These beam shifts therefore can be corrected for each value of ***E*** by using two trim coils in the x and y direction. The magnitudes of the coil currents required in the two trim coils for each positron energy are recorded in a set-up file and are changed automatically for each implantation energy to ensure the beam hits the target sample.

A single high-purity germanium (HPGe) detector is used to measure the Doppler broadening of the 511 keV gamma line from annihilations in the sample. Up to ~900 gamma rays are detected per second. About 20% of gamma rays incident on the detector interact with the Ge crystal, giving all or part of their energy to a single electron (via the photoelectric effect or Compton scattering, respectively). The electron then produces a large number of electron-hole pairs, the number of which is proportional to the energy deposited in the Ge crystal by the radiation. An electric field is applied to the detector to sweep the electrons to the anode, creating a detectable current pulse there. As the amount of energy required to create an electron-hole pair is known (~2 eV), measuring the size (height) of this pulse allows the energy of the incident radiation to be found using an amplifier and pulse height sorter. Cooling the germanium crystal to liquid nitrogen temperatures reduces thermal excitations of valence electrons so that only a gamma ray interaction can give an electron the energy necessary to cross the band gap and reach the conduction band.

[1] A. Dupasquier and A. P. Mills Jr. (ed.), Positron Spectroscopy of Solids. IOS Press (1995).

[2] R. Krause-Rehberg and H. S. Leipner, Positron Annihilation in Semiconductors. Solid-State Sciences Vol. 127 (Springer, Berlin, 1999).

[3] A. Perkins and J. P. Carbotte, Phys. Rev. B **1**, 101 (1970).

[4] P.J. Schultz and K.G. Lynn, Rev. Mod. Phys. **60**, 701 (1988).

[5] A. Ore and J. L. Powell, Phys. Rev. **75**, 1696 (1949).

[6] M. Charlton and J. W. Humberston, Positron Physics (Cambridge University Press, Cambridge, 2001).

[7] I. K. MacKenzie, T. L. Khoo, A. B. McDonald, and B. T. A. MacKee, Phys. Rev. Lett. **19**, 946 (1967).

[8] M. J. Puska, C. Corbel, and R. M. Nieminen, Phys. Rev. B **41**, 9980 (1990).

[9] A. van Veen, H. Schut, and P. E. Mijnarends, Positron Beams and their Applications ed P G Coleman (World Scientific: Singapore) p 191 (2000).

[10] S M Hutchings et al., J. Phys. E: Sci. Instrum. **19**, 282 (1986).

[11] A. van Veen, H. Schut, and P. E. Mijnarends, Positron Beams and their Applications ed P G Coleman (World Scientific: Singapore) p 24 (2000).

[12] E. Tandberg, P. J. Schultz, G. C. Aers, and T. E. Jackman, Can. J. Phys. **67**, 275 (1989).

[13] S. Valkealahti and R. M. Nieminen, Appl. Phys. A **32**, 95 (1983).

[14] S. Valkealahti and R. M. Nieminen, Appl. Phys. A **35**, 51 (1984).

[15] V. Ghosh, Appl. Surf. Sci. **85**, 187 (1995).

[16] N. B. Chilton and P. G. Coleman, Meas. Sci. Technol. **6**, 53 (1995).

[17] T. C. Griffith, G. R. Heyland, K. S. Lines, and T. R. Twomey, J. Phys. B: Atom. Molec. Phys. **11**, 20 (1978).

Chapter 3

Methods and Parameters

"Though this be madness, yet there is method in't."

-William Shakespeare, Hamlet

The following parameters are specific to the positron beam at the University of Bath used for the work throughout this thesis.

3.1 *S* and *W* Parameters

Each of the 4096 channels in the pulse height sorter (multi-channel analyser, MCA) corresponds to a gamma ray annihilation energy, with an average of 35.81 eV/channel. Doppler broadening ΔE is detected when the transverse momentum p_t of the electron is parallel to the sample-to-detector direction; $\Delta E = p_t c/2$.[1] Whether this momentum is away from or towards the detector determines if the 511 keV annihilation line energy is decreased or increased. A Doppler profile is then created for each incident implantation energy as seen in Fig. 3.1.

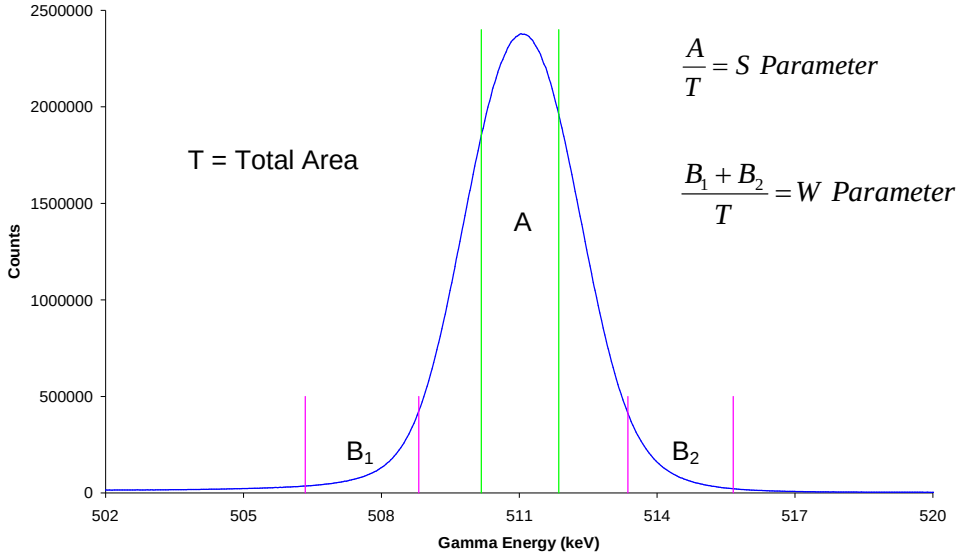

Figure 3.1: A Doppler broadened 511 keV peak in Al at 30 keV incident implantation energy. S and W Parameter windows are shown

The resolution of the germanium detector is ~1 keV which is typically of the same magnitude as the line broadening; this causes the Doppler profile to be relatively smooth and featureless.[2] The characteristic features of interest in a Doppler profile are the low-momentum central part of the peak and the high-momentum tails. The central parameter *S* is defined as the ratio of the counts in the central region of annihilation profile to the total number of the counts in the profile. Positrons will preferentially annihilate with low-momentum valence electrons due to the repulsive nature of the nucleus and contribute to this central region. In the same way as *S*, the wing parameter *W* is the relative fraction of the counts in the wing regions of the profile. Mainly core electrons have momentum values high enough to contribute to the *W* parameter - because of a small overlap in the positron wavefunction with the core electron wavefunctions[3] - and so *W* is therefore sensitive to atomic chemistry. The *S* and *W* parameters have characteristic values for each material, depending on the electron momentum distribution. When positrons are trapped, the profile is characteristic of the trapping defect. In a vacancy-type defect, the absence of core electrons means there is less high-momentum broadening, causing an increase in *S*. Because the positron has less overlap with core electrons, it also causes a decrease in *W*. The *S* and *W* parameters are measured using the Doppler profile at each positron implantation energy. This gives an idea of the electron momentum distribution for each implantation profile and therefore for an average depth. The relative changes in *S* are used to obtain the defect size and

concentration. If *S* changes rapidly over a small change in the implantation energy then the positron diffusion length, *L*, must be short in comparison with its implantation profile. Likewise if *S* does not vary then *L* can be much longer. Fitting of plots of *S* parameter vs positron implantation energy is thus used to obtain information on the average defect size and concentration as a function of depth, via the parameters *S* and *L*. The fitting program is called VEPFIT (Variable Energy Positron Fit).[4]

VEPFIT is a program which takes the experimental data and translates it into the relevant depth dependent parameters characterising the material by solving the positron transport equation. This equation takes into account the implantation, diffusion, drift, and trapping of positrons. By applying the appropriate boundary conditions surface related processes such as positron emission, positron surface trapping and positronium formation can be included.[5] VEPFIT fits the average *S* parameter and the diffusion length *L* in a chosen number of layers below the surface. The layer boundaries can be fixed or fitted. Any known *S* or *L* values for any layer can be input into the program and the program will fit the remaining parameters with a statistical accuracy measured by chi-square. To translate *S* and *L* into defect size and concentration in, for example, silicon, an *S*-*L* plot like the one in Fig. 3.2 is used. The curves in this plot are calculated assuming trapping in Si and only one type of defect. The measured *S* parameter (S_M) comes from a superposition of the *S* parameters from the defect (S_D) and the bulk (S_B), this can be written as

$$S_M = f_D S_D + (1 - f_D) S_B \tag{3.1}$$

where f_D is the fraction trapped in defects. If S_B is normalised to 1 then Eqn. 3.1 can be rewritten as

$$f_D = \frac{(S_M - 1)}{(S_D - 1)}. \tag{3.2}$$

f_D can also be written as the trapping rate ($\kappa = \nu C$) over the total annihilation rate,

$$f_D = \frac{\nu C}{(\lambda + \nu C)} \tag{3.3}$$

where ν is the specific trapping rate for the positron in a specific defect, λ is the annihilation rate in bulk Si and *C* is the defect concentration per atom. Combining Eqn. 3.3 into Eqn. 3.2 gives

$$S_M = 1 + \frac{(S_D - 1)}{\left(\frac{\lambda}{\nu C} + 1\right)} \tag{3.4}$$

The diffusion length can be handled in a similar way with

$$\left(\frac{L_M}{L_+}\right)^2 = \frac{\lambda}{(\lambda+\nu C)} \tag{3.5}$$

where L_M is the measured diffusion length and L_+ is the diffusion length in perfect Si. Eqn. 3.5 can be rewritten as

$$\frac{1}{\left(\frac{L_+}{L_M}\right)^2 - 1}. \tag{3.6}$$

Putting Eqn. 3.6 into Eqn. 3.4 then gives

$$S_M = 1 + \frac{(S_D - 1)}{\left(\frac{1}{\left(\frac{L_+}{L_M}\right)^2 - 1} + 1\right)} \tag{3.7}$$

which can then be rearranged to give

$$S_M = S_D - (S_D - 1)\left(\frac{L_M}{L_+}\right)^2. \tag{3.8}$$

This is plotted in Fig. 3.2 for various defect sizes. Further detail on this derivation can be found in Ref. 3 pages 491-528.

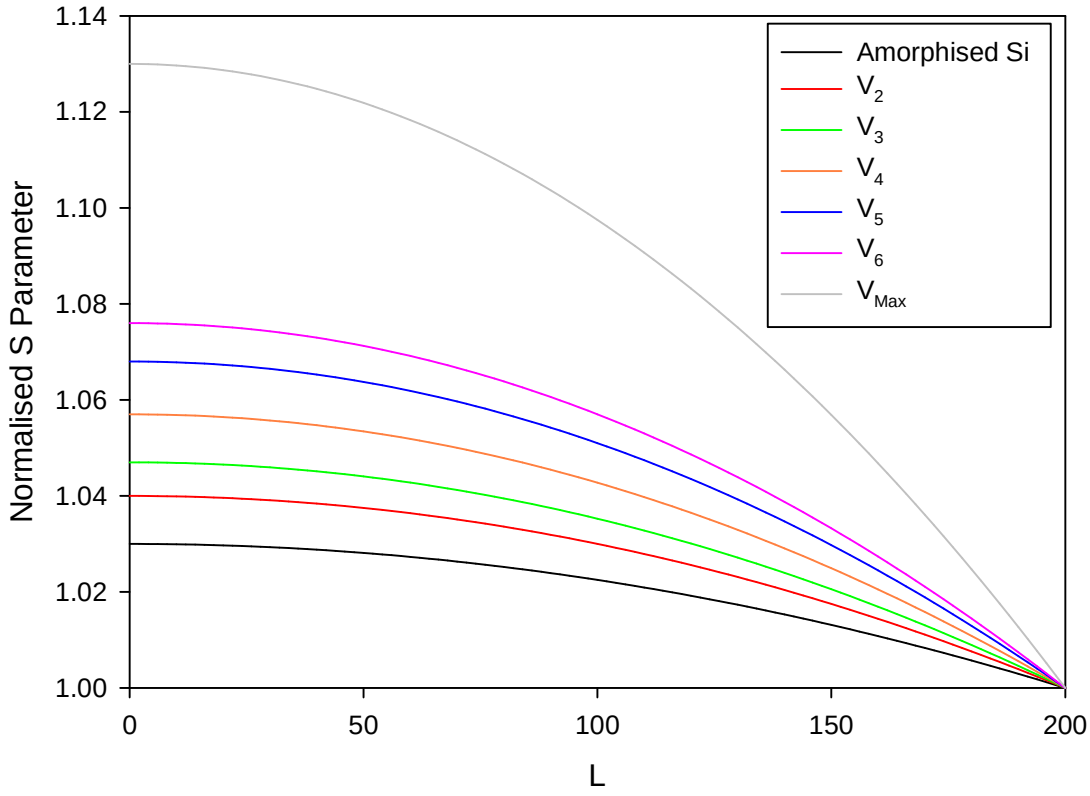

Figure 3.2: S-L plot for various defect sizes and concentrations in Si

Each line on the plot represents a different vacancy cluster size. Amorphous Si is likely to contain the smallest sized vacancies and so is the lowest line on the plot. V_2 to V_6 represent vacancy clusters of 2 to 6 missing atoms respectively. V_{max} is the starting cluster size in which the *S* Parameter will not be able to distinguish between this and larger defect sizes due to the finite positron lifetime. The *S* and *L* calculated by VEPFIT can be then plotted on this graph to determine (a) whether the combination is realistic, by the point lying on one of the lines, (b) the size of defect, by which of the lines it lies on, and (c) the defect concentration, which decreases with increasing diffusion length. The defect concentration, C_D, can be found if the *S* parameter or f_D is known:

$$C_D = 5x10^{22}.\frac{\lambda f_D}{\nu(1-f_D)} \text{ in cm}^{-3} \tag{3.9}$$

$$C_D = 5x10^{22}.\frac{\lambda(S-S_B)}{\nu(S_D-S)} \text{ in cm}^{-3} \tag{3.10}$$

The *S* parameter in this plot and in general is not used in its raw form because of its dependency on the window position (as seen in Fig. 3.1) which are not standard and because of time-drift effects caused by the resolution of the HPGe and the amplifier gain. It is the *relative* changes in the parameter which are of interest. Normalisation of the *S* and *W* parameters is achieved by dividing these values by a reference value, normally a defect-free bulk measurement of the same material.

3.2 Normalisation Method for *S* and *W* Parameters

Doppler broadening parameters can be affected by drifts in the Ge detector resolution and electronic instabilities. The resultant changes in both the *S* and *W* parameters can be larger than the real changes within and between data sets, rendering comparisons meaningless. In order to minimize the effect of such drifts the sample is positioned on the holder above a reference sample – usually crystalline Si - in the vertical plane with a ~3 mm gap between. The two orthogonal trim coils, normally used to position the beam at different energies, then deflect the ~8 mm diameter 30 keV beam by ~11 mm from the base of the sample of interest to the top of the reference sample, and spectra are collected (and *S* and *W* evaluated) alternately for the two bulk samples. The average ratio between the parameters at 30 keV is then used to evaluate normalised *S* and *W* relative to the reference sample. An example of this

method can be seen Figs. 3.3 and 3.4 which show the difference between the results before and after this procedure.

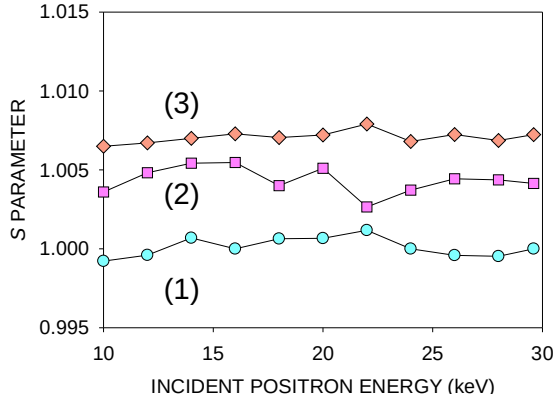

Figure 3.3: S parameters for samples (1)-(3) normalised to bulk S value for sample (1).

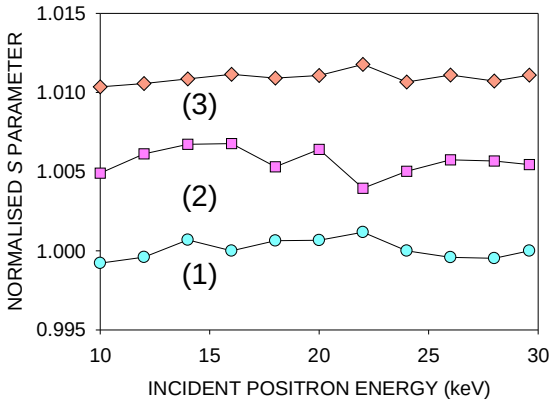

Figure 3.4: S Parameter data normalised using the alternating sample method.

This example, from chapter 6.1, shows a significant change in *S* (and *W*) parameters allowing for direct comparisons of different samples over long periods of time. All data normalised in this thesis uses this method to do so.

3.3 *P:V* Ratio

A measure of the positronium formed is another parameter used to obtain information about a sample. Positronium formation in semiconductors, such as porous silicon, can only exist at the surface or in large open volume defects. In general there is a 3:1 ratio of o-Ps to p-Ps formation. This ratio can be reduced by competing processes such as pick-off annihilation, in which the positron annihilates with an electron of opposite spin from one of the surrounding atoms.[2]

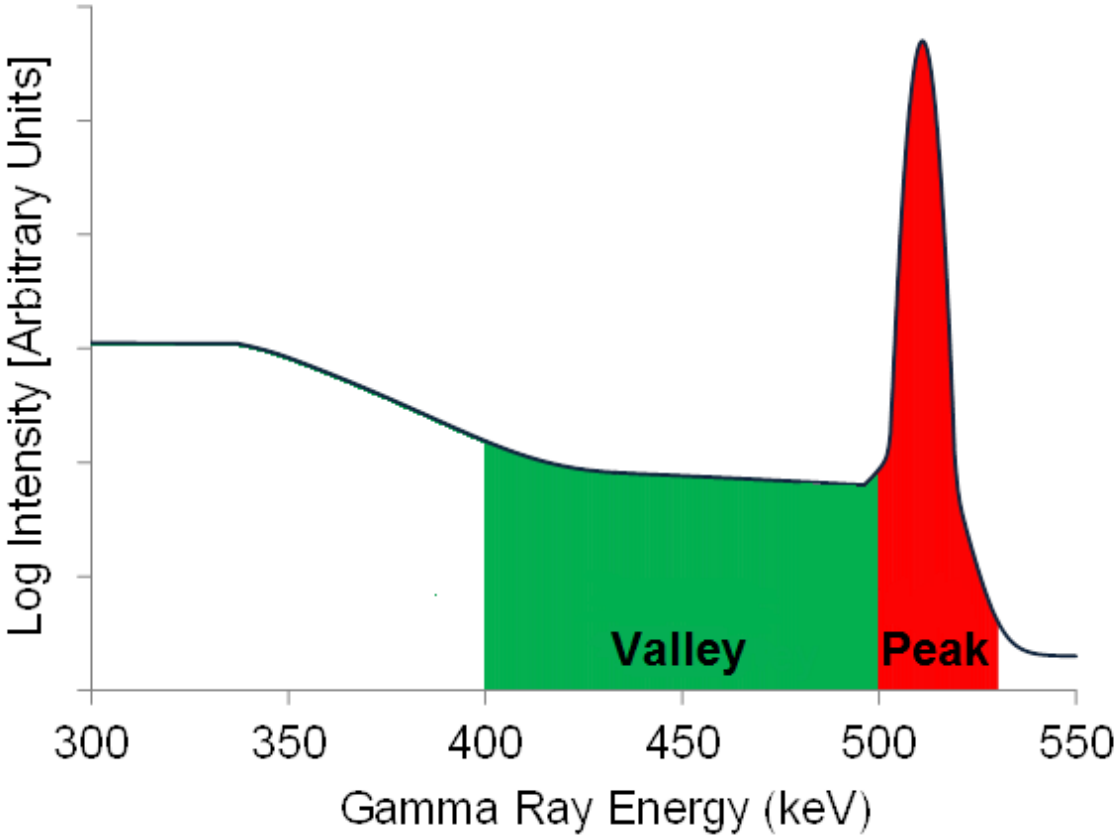

Figure 3.5: Valley and peak regions in the full annihilation spectrum.

The *P:V* ratio is the ratio of the total number of spectrum counts in the 511keV annihilation photopeak (Fig. 3.1) to those in the valley region between ~400-500 keV, seen in Fig. 3.5. It is particularly sensitive to the probability that ortho-positronium (o-Ps) is formed and survives to decay into three gamma photons. A higher *P:V* means less o-Ps as the third smaller o-Ps decay photon contributes to the valley counts *V*.

3.4 Correction Method for *P:V* Ratio

The *P:V* ratio is particularly sensitive to the probability that ortho-positronium (o-Ps) is formed in the aerogel and survives to decay into three gamma photons. (Higher *P:V* means less o-Ps.) o-Ps decay photons contribute to the valley counts *V*.

V, however, also contains a background contribution associated with the peak *P* (due to incomplete charge collection in the Ge detector) as well as from other background sources. In total for an o-Ps producing sample $V = V_{Ps} + V_P + V_B$ where V_{Ps} is o-Ps contribution to the

valley. To correct for this a background spectrum (collected with the slow positron beam switched off) was measured and background counts V_B subtracted from a Si spectrum (with no Ps so $V = V_P + V_B$) to find the contribution V_P to V from incomplete charge collection as a fraction of P. Using this information, V_B and V_P were computed and subtracted from each measured V, which was then used to calculate the 'true' $P:V$ ratio = P / V_{Ps}. The counts in the peak are many orders of magnitude greater than background and other peak contributions so no correction to P was made for 1st order calculations.

An example of this correction method can be seen in Figs. 3.6 and 3.7, taken from chapter 6.1.

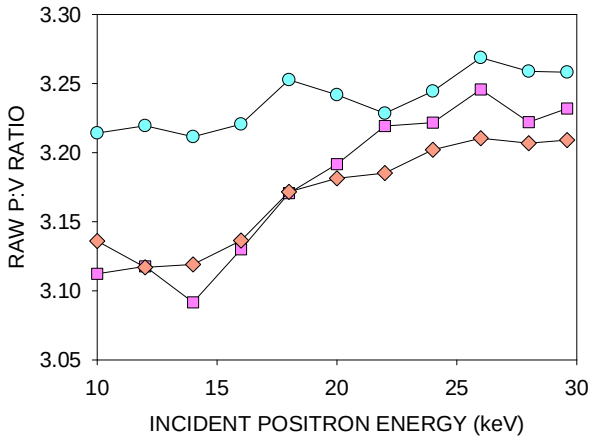

Figure 3.6: Raw bulk measurements for P:V ratio for all samples.

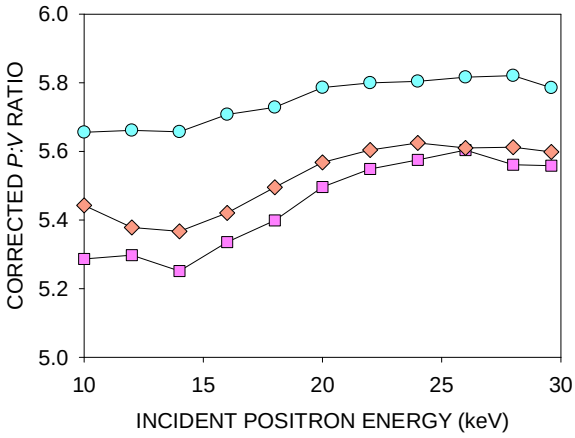

Figure 3.7: P:V ratios after correction method was applied.

Fig. 3.6 shows the raw $P:V$ ratios for the three samples. The corrected ratios in Fig. 3.7 show a fourfold increase in sensitivity to o-Ps annihilation between samples 1 and 2. The raw P:V for Cz Si had an average P:V = 8.4 whereas when the corrected ratio was 18.9.

3.5 Spectrum Ratio Curves

The ratio curve technique measures – also with a single Ge detector - the annihilation line, or spectrum, peaked at 511 keV with high precision to extract further information from the higher momentum components contained in its wings. Core electrons have a characteristic momentum associated with their atom enabling chemical analysis of the species that surround the annihilation site.[6] Positrons are implanted at a single energy where the response is the greatest for the region of interest. The spectrum, collected typically for ~ 48h, is normalised

to an area of 1.5 x 10^8 counts (chosen because it is just under the number of counts taken after ~48h) between 491-531 keV and divided by a reference spectrum, usually undefected Si, to reveal any differences in the high momentum content between 511-531 keV.

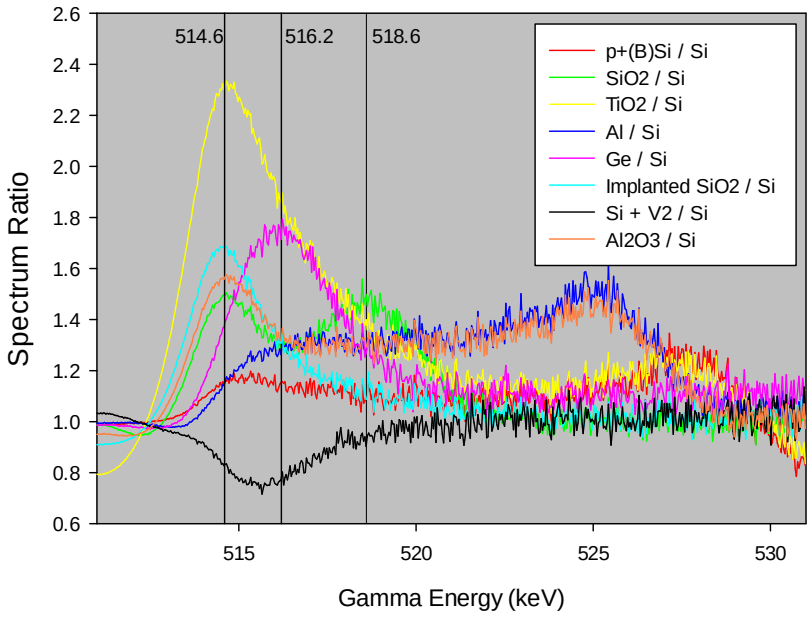

Figure 3.8: Examples of spectrum ratio curves.

This difference is the response to the chemical composition of the environment surrounding a positron-trapping defect such as a vacancy. Fig. 3.8 shows various spectrum ratio curves. A reoccurring peak can clearly be seen at 514.6 keV for TiO_2, SiO_2 and Al_2O_3 which is known to be caused by the presence of oxygen.[7, 8] It is also the only difference when comparing Al to Al_2O_3. Divacancies also leave a unique signature as a deficit of high-momentum content.

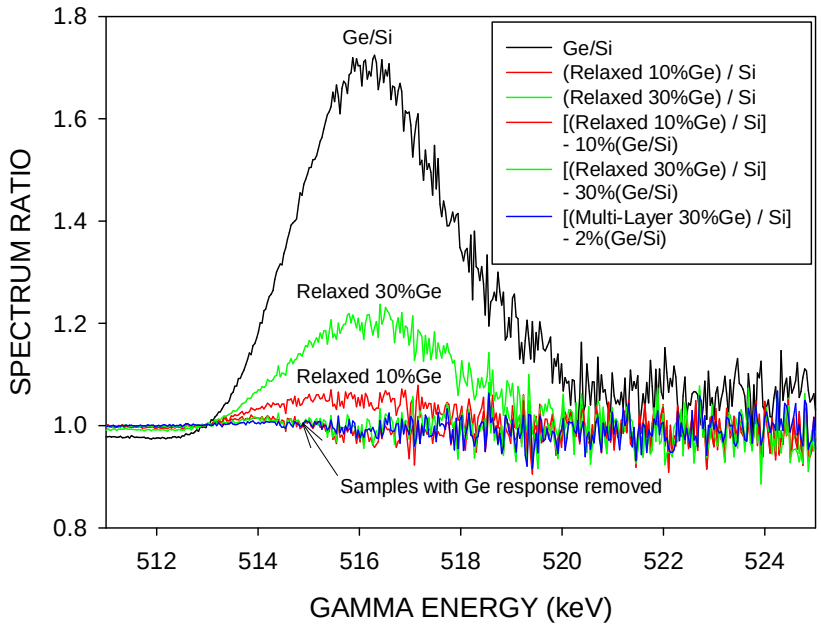

Figure 3.9: Spectrum ratio curves for samples of SiGe with 10%, 30% or 100% Ge. Curves with their Ge response removed are also shown.

The heights of the peaks contain information about the strength of the response. In Fig. 3.9, from chapter 5.3, the ratios of the SiGe peak heights to the Ge peak height are equivalent to the percentage of Ge contained within them.

The response can be due to the presence of one type of atom or defect type but in more complex systems it can be formed from combinations of all the pure states that lie within the region of the implantation profile e.g. F, V_2 in Si, Ge and O. By fitting combinations of these pure states, each with its own unique signature, a more detailed picture of the vacancy complexes in the region of interest can be found.

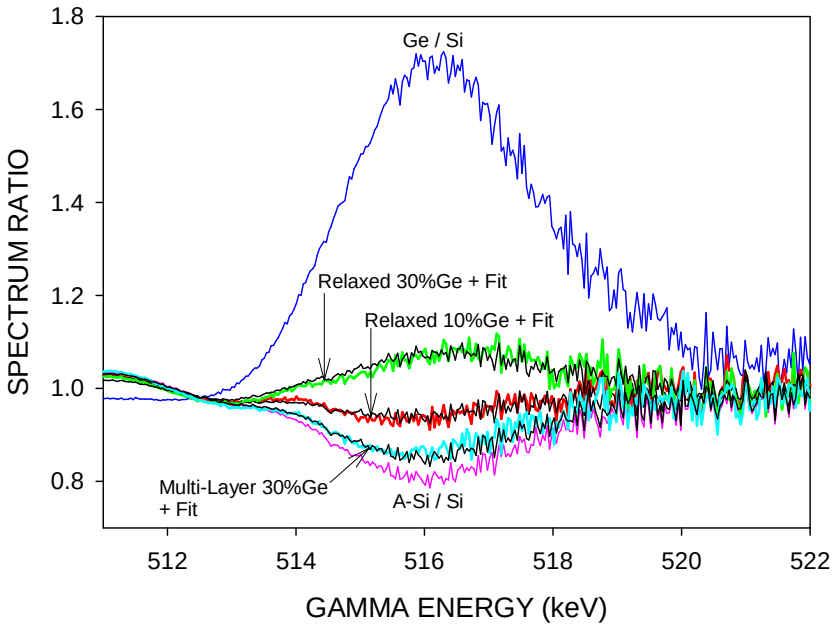

Figure 3.10: Spectrum ratio curves with fits.

This example, again from chapter 5.3, shows that spectra of Ge and amorphous Si (A-Si) can be combined together in certain percentages to recreate each sample spectrum.

[1] H. P. Hotz, J. M. Mathiesen, and J. P. Hurley, Phys. Rev. **170**, 351 (1968).

[2] A. van Veen, H. Schut, and P. E. Mijnarends, Positron Beams and their Applications ed P G Coleman (World Scientific: Singapore) p 191 (2000).

[3] A. Dupasquier and A. P. Mills Jr. (ed.), Positron Spectroscopy of Solids. IOS Press (1995).

[4] H. Schut A. van Veen, J.de Vries, R.A. Hakvoort, M. R. Ijpma, AIP Conf. Proc. **218**, 171 (1990).

[5] H. Schut and A. van Veen, J. Phys. IV **5 C1**, 57 (1995).

[6] K. G. Lynn and A. N. Goland, Solid State Commun. **18**, 1549 (1976).

[7] U. Myler and P.J. Simpson, Phys. Rev. B **56**, 14303 (1997).

[8] W. Deng R.S. Brusa, G.P. Karwasz, A. Zecca and D. Pliszka, Appl. Phys. Lett. **79**, 1492 (2001).

Chapter 4

Oxide Films

"If my film makes one more person miserable, I've done my job."

- Woody Allen

The purposeful creation of thin film oxides on semiconductor and other various substrates have been shown to exhibit various interfacial properties such as surface passivation,[1] electro-luminescence[2] and, when grown with a different method on the same substrate, produce a higher quality oxide.[3]

Variable energy positron spectroscopy is an ideal tool for looking at thin films because it allows the positron mean implantation depth to be gradually increased through the film into the substrate. The method is sensitive to oxygen deficiency and to vacancy defects introduced by doping and growth procedures. As well as film characterization, positrons are particularly sensitive to the interface between the film and substrate.

4.1 Positron annihilation studies of the $AlO_x/SiO_2/Si$ interface in solar cell structures

4.1-I Introduction

Surface recombination in crystalline Si (c-Si) solar cells has a high impact on efficiency.[4] Aluminum oxide (AlO_x) films have been found to provide excellent surface passivation.[1] However, neither the AlO_x/Si interface properties nor the charge trapping mechanism in the dielectric films are fully understood.[5] It has been found that the surface passivation mechanism of sputtered AlO_x films is the same for those deposited by other methods. It is not the bulk of the AlO_x film, or the O/Al ratio, that passivates but the formation of a silicon oxide (SiO_2) layer at the interface during annealing.[6] The AlO_x/Si interface and the effect of different growth methods, film thickness and annealing are investigated using variable-

energy positron annihilation spectroscopy (VEPAS) and Doppler-broadened spectra ratio curves. Positrons are an ideal probe due to high sensitivity to interfaces enabling defect and chemical analysis of this region.[7, 8, 9]

4.1-II Experimental Procedure

AlO_x was deposited on 0.8 Ω.cm FZ p-Si by T.-T. A. Li at Australia National University using two different methods. The first was thermal atomic layer deposition (ALD)[10], used to grow 30 or 60 nm–thick films. Samples were deposited using a Cambridge Nanotech thermal ALD reactor. A cycle in the reactor consisted of a 15 ms injection of $Al(CH_3)_3$ vapour followed by a 5 s N_2 purge. The oxidation step consisted of a 15 ms injection of H_2O vapour followed by a 5 s purge with N_2 resulting in a deposition rate of 1.06 Å/cycle (0.6 nm/min). The second method was RF magnetron sputtering[6], used to grow 30 nm–thick films. Material from an Al target was deposited onto a rotating silicon substrate (40 rpm) at 25ºC for ~5 mins. The sputtering gases used were Ar (20 sccm) and O_2 (2 sccm) (where sccm = flow in standard cubic centimeters per minute) in a working pressure of 3 mTorr (< $7x10^{-7}$ Torr base pressure). RF power was 300W (~130V). A Maxtek TM-350 quartz crystal thickness monitor was used to measure a rate of deposition of 4.3 nm/min. Thicker (740 nm) sputtered films were also deposited on 0.8 Ω.cm FZ p-Si and 1 Ω.cm Cz n-Si. All samples were studied in the as-deposited state and after annealing at 425°C in N_2 for 30 min.

4.1-III Results and Discussion

30 and 60nm thermal ALD films

Differences were investigated between the four thermal ALD samples - 30 or 60 nm AlO_x films on 0.8 Ω.cm FZ pSi - before and after annealing at 425°C in N_2 for 30 min. Fig. 4.1.1 shows $S(E)$ results for these samples.

The S parameter is normalised to unity for the bulk material. The mean positron implantation depth ($\bar{z}$) is also shown where $\bar{z} \approx (40/\rho)E^{1.6}$ nm, ρ being the density of the material in gcm^{-3} and E in keV. A response to the film can be seen in the 60 nm film samples as an inflection in the $S(E)$ curve at around 1.5 keV. This response is not as clear in the 30 nm film samples. All four plots show a rapid rise in the S parameter until ~6 keV, an indication that the effective positron diffusion length (L) is quite short (L ~ 10 nm from VEPFIT) in this region. VEPFIT

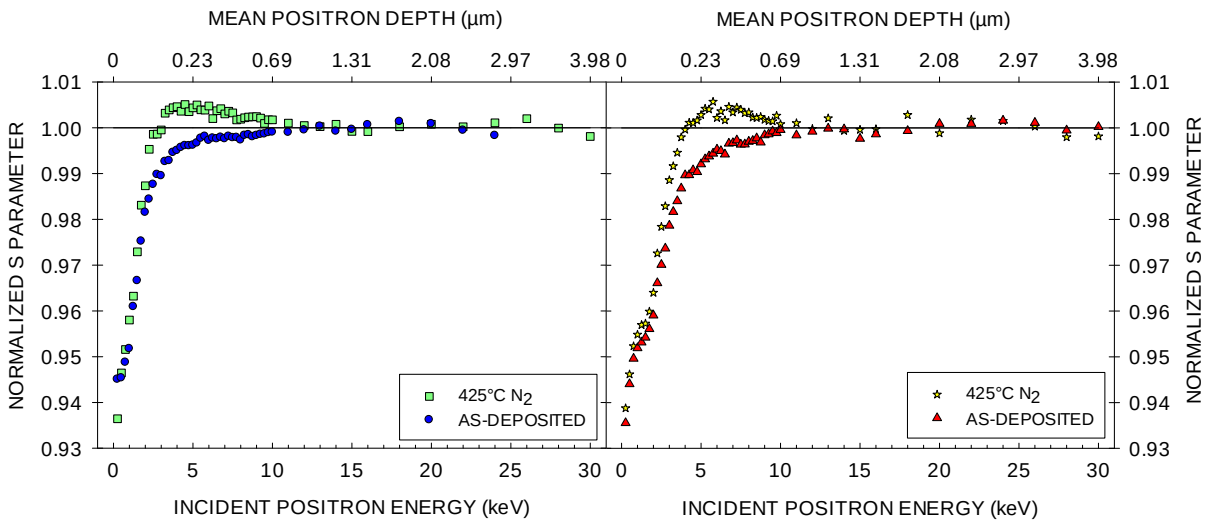

Figure 4.1.1: Normalized S(E) plot for AlO_x films deposited by thermal ALD before and after annealing at 425°C in N_2 for 30 min. Left: 30 nm film. Right: 60 nm film.

also finds that positrons are being efficiently trapped, i.e L ~ 0 nm, in the AlO_x/Si interface (~1 nm) and are allowed to freely diffuse in the Si, i.e L ~250 nm. Before annealing, this trapping interface has an S parameter very close to that of bulk Si. The interface S parameters of both samples, found by VEPFIT, rise to ~1.01 after annealing; to have this kind of response positrons must be annihilating on the Si side of the AlO_x/Si interface, because the oxide – and vacancy defects in the oxide – have characteristic S parameters which are significantly lower than bulk Si.[11] This is feasible as it has been shown that there is a high negative charge density in the AlO_x within ~1 nm of the interface created by a high oxygen-to-aluminum ratio from the incomplete ALD process during the first deposition cycles.[12] Furthermore, this negative charge significantly increases following the low temperature annealing, usually by a factor of 100.[1] A high negative fixed charge density strongly reduces the electron concentration, thus inducing a positive charge on the Si side of the thin insulating SiOx layer formed during the first ALD cycles.[13] It is proposed that this positive charge stops the positrons from diffusing back into the AlO_x and SiO_x so that annihilation occurs in the Si at the SiO_x/Si boundary. Ratio curves were used to further investigate the defects within the two regions of interest here - the AlO_x film and the interface – by collecting spectra at E = 1.5 keV and 6 keV, respectively.

Fig. 4.1.2 shows the results at E = 1.5 keV for the 60 nm film samples, which were used because of the larger positron response to the AlO_x film.

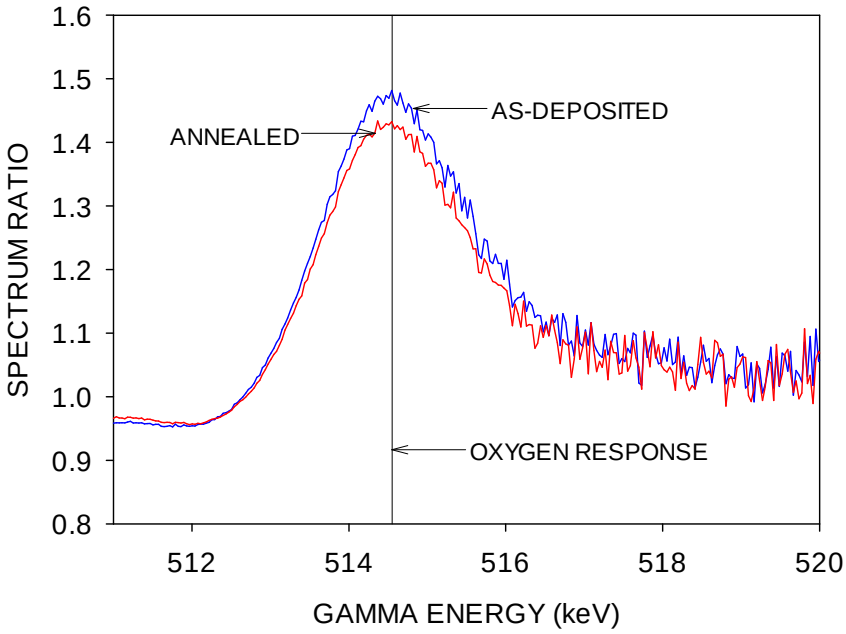

Figure 4.1.2: Ratio of the 60 nm AlO_x film sample spectra at 1.5 keV, before and after annealing, divided by a c-Si spectrum.

The sample spectra are divided by a reference spectrum, in this case that for Cz Si, and plotted against gamma energies from 511 keV. The peak at ~514.6 keV in these samples is caused by the presence of oxygen.[14, ENREF 9 15] Using the absolute peak heights and assuming a linear response, there appears to be ~9±2 % less oxygen response after annealing. Open volume defects in the AlO_x film may be being annealed away, reducing the likelihood of positrons trapping next to oxygen atoms, but oxygen may also be diffusing out of the film. Other studies[5, 6] have shown that annealing causes the growth of an SiO_2 interface, consistent with oxygen out-diffusion from the AlO_x film. Fig. 4.1.3 shows the ratio curve results using E = 6 keV. The 30 nm film samples were used because their $S(E)$ response is dominated by the interface. Small oxygen peaks are present here not because there is oxygen present in the interface but because of the small overlap of the positron implantation profile with the surface/film. The dip in the ratio curves is believed to be a response to V_2 as vacancies result in a reduction of high-momentum content.[16] To confirm this a sample of Si was implanted with 160 keV Ge to a fluence of 5 x 10^{15} cm^2. A saturated V_2 type defect response was observed in $S(E)$ at 6 keV; similar results were seen in Ref. [17]. A lineshape was thus taken at 6 keV and the resulting V_2 ratio curve is shown for reference.

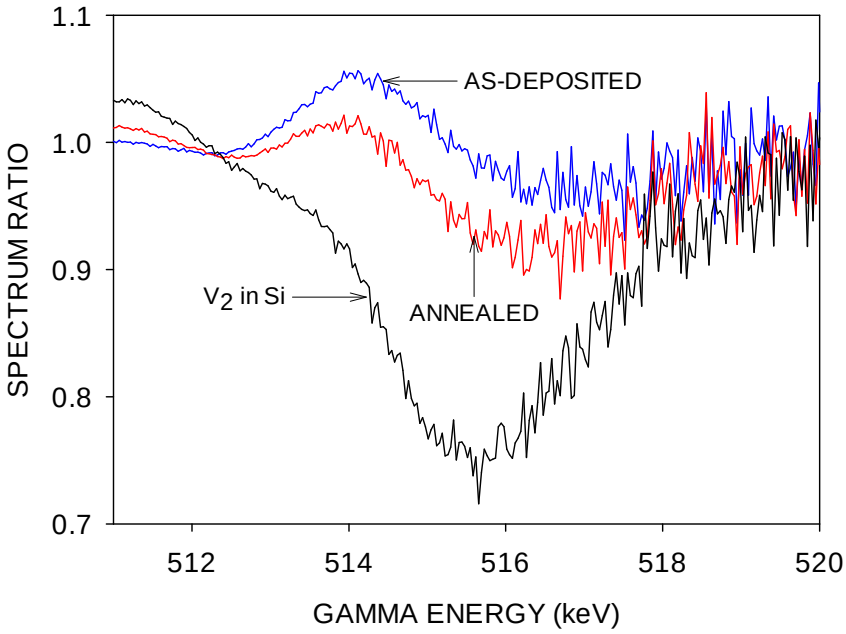

Figure 4.1.3: Ratio of the 30 nm AlO_x film sample spectra at 6 keV, before and after annealing at 425°C in N_2 for 30 min, divided by a c-Si spectrum. The ratio for a saturated di-vacancy response in Si is shown for reference.

Both samples show some response to V_2, which is increased by annealing. By scaling the saturated V_2 response to overlap with the two sample responses a percentage of the positrons annihilating in V_2 in the Si at the SiO_x/Si boundary can be obtained: 20±2 and 47±2 % before and after annealing, respectively. This increase in vacancy response is either caused by an increase in the number of defects, possibly by the growth of the SiO_2 interface during annealing, or by an increase in the probability of trapping by vacancies already present. The oxygen responses deduced for both samples after removing the V_2 responses were found to be identical (~3%), as expected from the overlap of the positron implantation profile with the oxide film. It is therefore unlikely that an increased sensitivity to V_2 would be due to a reduction of positron trapping in the oxides; the increase could, however, be caused by a change in the charge state of the vacancies (i.e., from positive to neutral or negative).

The *S*-*W* plots[18] in Fig. 4.1.4 reveal the states in which positrons are annihilated and how the sensitivity to each state changes with varying *E;* each specific annihilation site has an associated point on the *S*-*W* graph. The *W* parameter here is also normalised to unity for the bulk material. The large circles indicate the different states, as found with VEPFIT, within the samples.

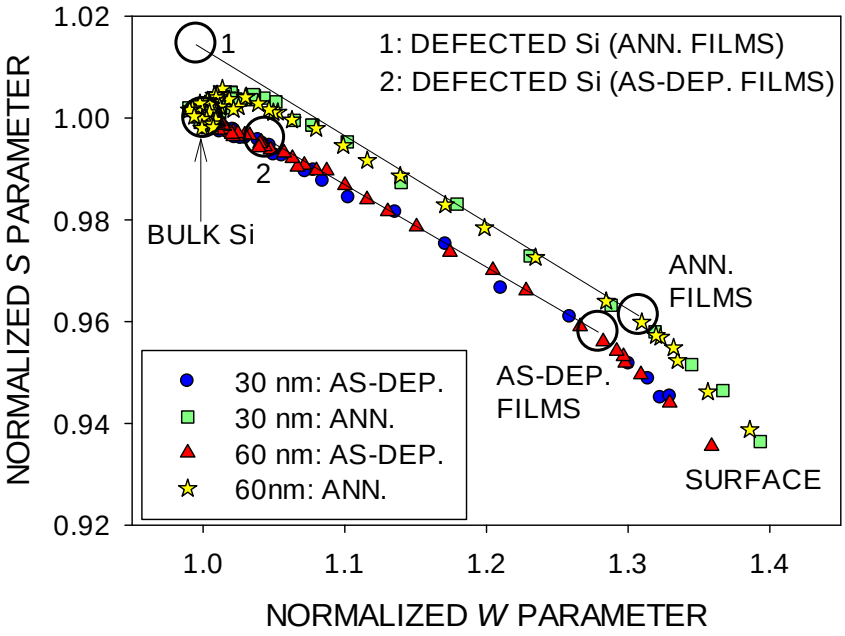

Figure 4.1.4: Normalized S-W plot for 30 and 60 nm AlO_x films deposited by thermal ALD before and after annealing at 425°C in N_2 for 30 min. The large circles denote different states within the samples.

Both as-deposited and annealed samples have different surface and film states in which positrons are annihilated, where the different film response is thought to be due to varying oxygen content. Both also have some response to what is believed to be the defected Si. The annealed samples exhibit the most prominent response to vacancy-type defects, but the as-deposited samples also have a slight defect response, agreeing with the ratio curves and *S*(*E*) plots.

Different AlO_x Growth Methods

To look at the differences between $AlO_x/SiO_2/Si$ samples grown by thermal ALD and sputtering on 0.8 Ω.cm FZ pSi, 30 nm-thick film samples were compared before and after annealing at 425°C in N_2 for 30 min. The *S*(*E*) plot for the as-deposited sputtered film rises much more slowly towards unity with increasing *E* than for the ALD film, with a much reduced trapping response, as shown in Fig. 4.1.5.

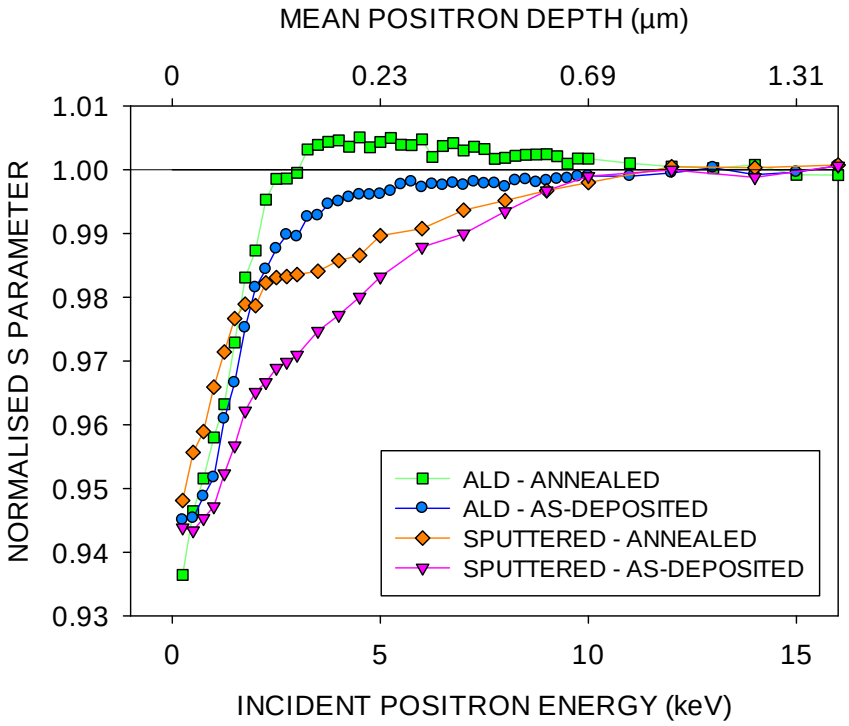

Figure 4.1.5: Normalized S(E) plot for 30 nm AlO_x films deposited by thermal ALD or by sputtering, before and after annealing at 425°C in N_2 for 30 min.

Once annealed, however, the response rapidly increases towards that of the thermal ALD samples, although it does not have the same defected Si interface feature. The *S*-*W* plot in Fig. 4.1.6 is used to determine the nature of the interface in the sputtered sample before and after annealing, in comparison with the ALD sample.

The data for the sputtered sample shows little or no response to the film or the defected Si state. The sputtered film/Si interface is highly trapping, particularly after annealing, but this appears not to be caused by defects in Si, but rather perhaps by an oxide response at the interface. The *S*-*W* plot shows this interface state, as found with VEPFIT (thickness ~1 nm). The as-deposited sputtered film has an interface state that does not lie on the Si-AlO_x *S*-*W* line. This, along with the low *S* and high *W* parameters, indicates a high oxygen response – viz, a defected oxide state. Upon annealing the interface response now lies along the Si-AlO_x line. This is still an oxide response, but the higher *S* and lower *W* parameters suggest an annealed oxide response – i.e., undefected oxide. The high negative fixed charge density seen in the thermal ALD samples appears to be either much weaker or not present in the sputtered samples, reducing the positron response to the film and increasing it in the SiO_2 layer. These

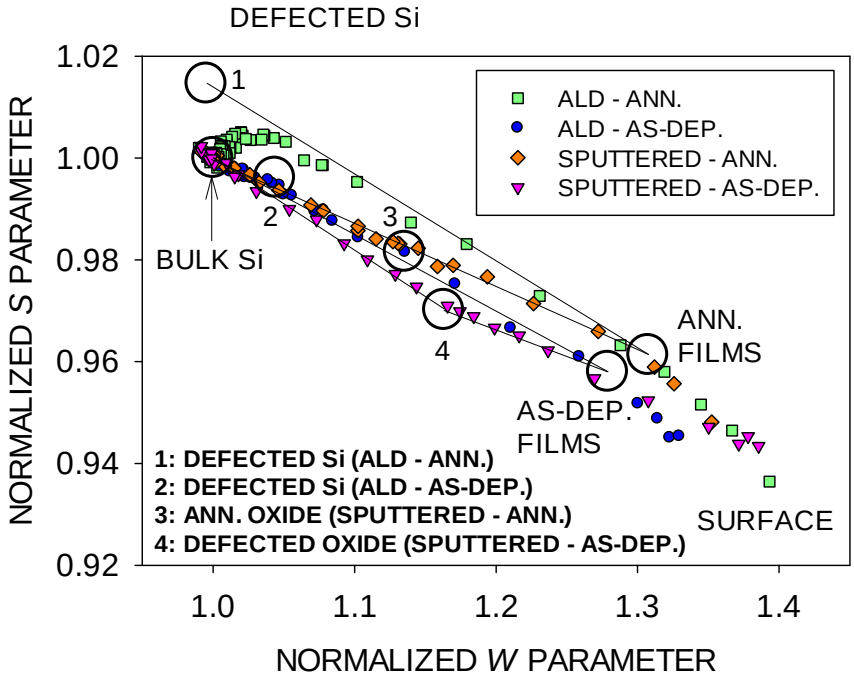

Figure 4.1.6: Normalized S-W plot for 30 nm AlOx film deposited by thermal ALD or by sputtering, before and after annealing at 425°C in N2 for 30 min. The large circles denote different states within the samples.

differences may be the reason why ALD films are generally better passivating than those sputtered.[19]

Thick Films

The sputtering growth method was further investigated with thicker (740 nm) films to look better at the differences between the positron responses to the as-deposited and annealed films, and additionally the effects of the substrate type on *S*(*E*). The *S* parameter in the thick films appears to be on average lower than in all the thin films, indicating a greater response to oxygen, as seen in TiO_2 films.[9] As in the thin-film sputtered samples there is a difference in the positron response to the AlO_x film after annealing, made more directly observable by the increased thickness, as shown in Fig. 4.1.7.

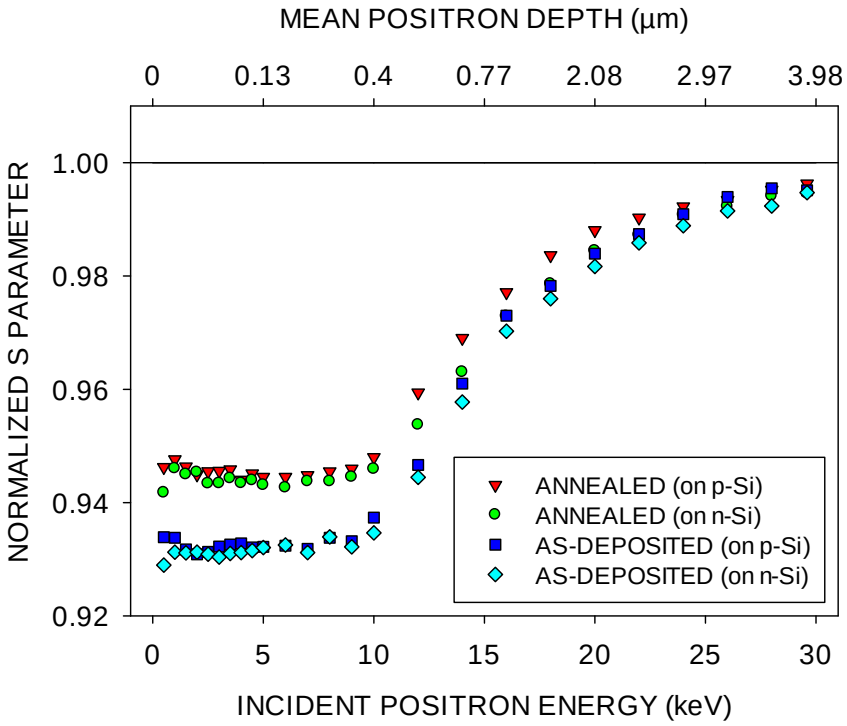

Figure 4.1.7: Normalized S(E) plot for 740 nm AlOx film deposited by sputtering on p or n-type Si, before and after annealing at 425°C in N2 for 30 min

The annealed films have a higher average *S* parameter, which can also be seen on the *S-W* plot in Fig. 4.1.8.

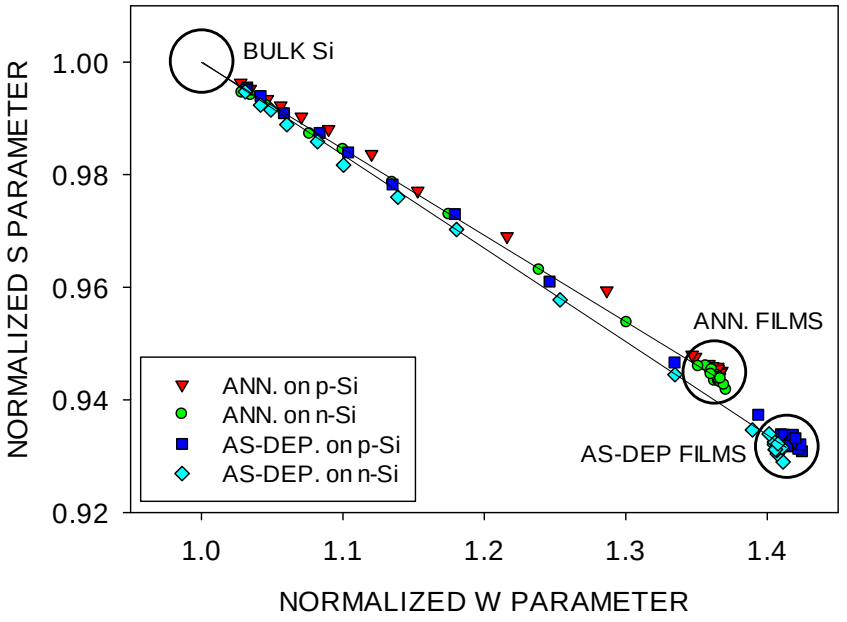

Figure 4.1.8: Normalized S-W plot for 740 nm AlO_x film deposited by sputtering on p or n-type Si, before and after annealing at 425°C in N_2 for 30 min. The large circles denote different states within the samples.

This plot shows no evidence of any trapping interface state as seen in the thin ALD films (Figs. 4.1.4 and 4.1.6). It can also be seen in Fig. 4.1.8 that the films have a higher *W* parameter *before* annealing, indicative of a higher oxygen content. This was verified in the ratio curves taken at E = 5 keV, shown in Fig. 4.1.9, where annealing causes a decrease in the size of the oxygen-related peak.

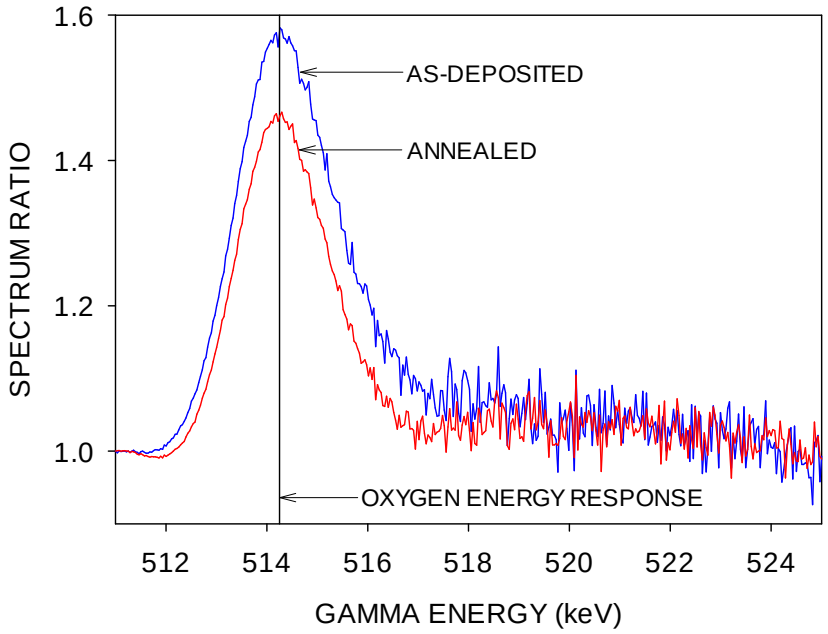

Figure 4.1.9: Ratio of the 740 nm AlOx film sample spectra at 5 keV, before and after annealing, divided by a c-Al spectrum. The vertical line indicates the mean energy associated with annihilation by oxygen valence electrons.

Compared to the thin films the observed decrease in O response is much larger with a 21±2% drop after annealing. The thick films start with a much greater O response than the thin films, caused either by more O atoms or by more vacancies. After annealing the thick film's O response drops to a level similar to that in the thin films. There also appears to be some difference between samples with p and n-type substrates. The p-type samples have a slightly higher *S* in the film and appear to have a lower effective positron diffusion length in the bulk Si. This last observation could be a result of band-bending at the SiO_2/Si interface.[20]

4.1-IV Conclusions - AlO_X/SiO_2/Si Interfaces

This work has shown that positron techniques are an excellent probe of AlO_x film and film/substrate interface characteristics. Here the films were grown by thermal ALD and sputtering methods, to different film thicknesses and with different substrate dopant types,

and their evolution was studied after annealing at 425°C in N_2 for 30 min. All samples have an interface which traps positrons, and annealing has the effect of increasing this trapping response, regardless of growth method. The cause of this trapping, however, is different in the samples grown by the two methods. Thermal ALD creates an $AlO_x/SiO_x/Si$ interface with positron trapping and annihilation occurring in the Si side of the SiO_x/Si boundary. Thermal ALD is known to cause a high negative charge density in the AlO_x within ~1 nm of the interface, inducing positive charge in the Si next to the interface. This positive charge reduces diffusion into the oxides and increases annihilation in the Si. In this region there is a V_2 response (20±2%) before annealing which increases to 47±2% after annealing. The data for both thin and thick sputtered films do not show any evidence for electrostatic shielding or positron trapping in defects in Si near the interface, but rather trapping occurs directly in the SiO_x interface in the as-deposited sample, and the positron response to it increases after annealing, as an SiO_2 layer is formed. Annealing the film has the effect of lowering the film oxygen response in all film types.

4.2 Defects in TiO_2 films on p^+-Si studied by positron annihilation spectroscopy

4.2-I Introduction

Much attention has been focused on titanium dioxide (TiO_2) in recent years because of its optical and electronic properties.[21, 22] Electro-luminescence (EL) is a potentially important tool in the development of silicon-based opto-electronics. Zhang et al.[2] demonstrated for the first time EL from TiO2/p^+Si heterostructures, attributing the EL to recombination between electrons at V_O (oxygen vacancy) levels and holes in the valence band. Consequently Zhang et al.[23] found a correlation between EL from these heterostructures and the concentration of V_O in the oxide film produced by argon plasma treatment.

As room-temperature luminescence from TiO_2 is associated with defect-related light-emitting centers, it is to be expected that positron annihilation spectroscopy (PAS) – a technique with exceptional sensitivity to open-volume point defects – should be applied to investigate the

defect structure of TiO_2. Information on V_O in plasma-treated TiO_2/p^+Si samples was gained by the application of the variable-energy form of PAS (VEPAS)[23].

VEPAS is well suited to the study of films of ~102 nm thickness, as in the present case. It has, for example, been used to investigate the defect structure of high-*k* TiO_2 films on SiO_2/SiC substrates.[7, 8, 24]

The present work was motivated by preliminary observations of EL enhancement by annealing TiO_2/p^+Si structures in vacuum or hydrogen ambient, with EL intensity also increasing with oxide film thickness, and to investigate (using VEPAS) whether these observations were also related to V_O concentration.

4.2-II Experimental Procedure

TiO_2/p^+-Si heterostructures were prepared by the thermal oxidation (500ºC, 2h) of sputtered Ti films on heavily boron-doped silicon (p^+-Si) substrates. The TiO_2 film thicknesses were 100, 150 and 220 nm; there was a thin SiO_2 layer between film and substrate. The samples were annealed in vacuum or in hydrogen at 500ºC for 1h. The pressures for the annealing in vacuum and in hydrogen were 8×10^{-3} and 2 Pa, respectively, and the samples were cooled in the same ambients at 0.7 ℃/min. until the temperature dropped to below 100ºC.

Examination of the 100 and 220 nm-thick films after H_2 annealing by scanning electron microscopy (SEM) showed no discernible difference in microstructure between the samples. Structural characterization of similar films was reported[23] but, as standard methods were found to be insensitive to vacancy point defects, the present study focused on the application of VEPAS.

The samples were investigated by VEPAS in the as-grown state and after annealing in vacuum and in hydrogen. The positron parameter *S* was measured as a function of incident positron energy *E* from 0.25 to 30 keV, and annihilation lineshapes were recorded for samples 1-4 and 7 at 1.5/2.0 keV, and sample 1 at 2.5 keV. *S* was also measured for a sample of bulk single-crystal TiO_2. The data were all normalized to the parameter values for bulk Si. As no extra information was gleaned from measurement of other positron parameters (e.g., *W* - see Ref.[18]), this report will focus only on *S*. Annihilation lineshapes were recorded for a number of the samples 1-4 at *E* chosen to correspond to depths of interest.

4.2-III Results

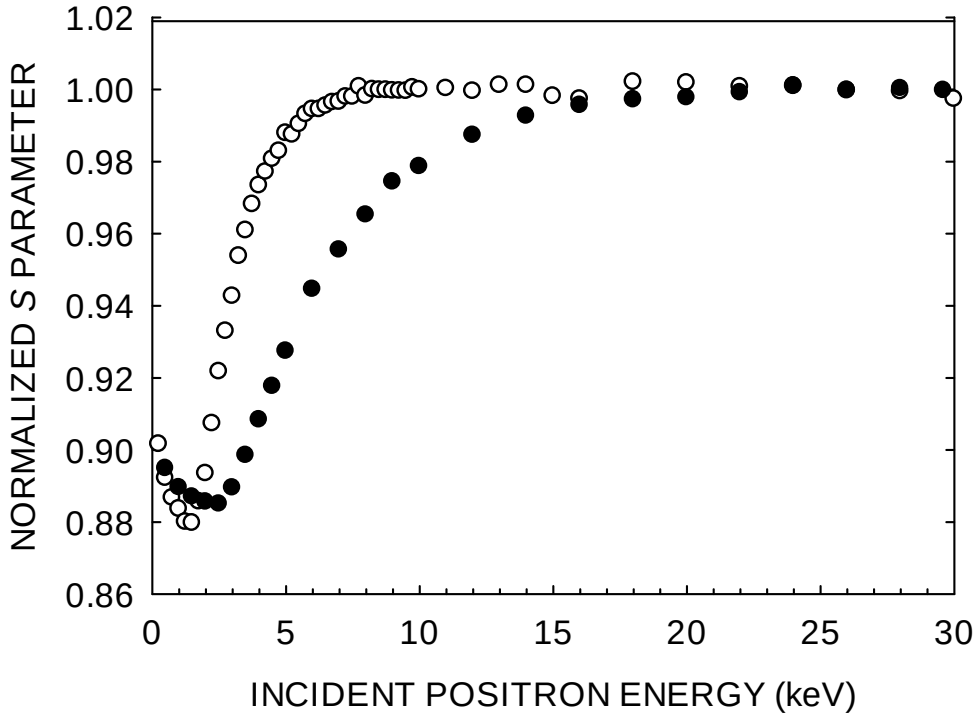

Figure 4.2.1: Normalized S(E) for 100 nm-thick films on Si substrates. Open circles: current TiO_2/p^+Si structure; solid circles: TiO_2 film on a different Si substrate.

S falls from the surface value (at $E \sim 0$) towards the value characteristic of the oxide film. Because the film thickness is comparable to the spread of the positron implantation profile, and positrons can additionally diffuse after thermalization, the measured minimum value of *S* does not equal that characteristic of the oxide film (that would only be recorded if all the implanted positrons were annihilated in the film). The film *S* is extracted using the code VEPFIT[25]. *S* then rises again towards the substrate value (here unity) as an increasing fraction of the implanted positrons reach depths so far distant from the film that a negligible fraction are able to diffuse back to it, and instead are annihilated in the silicon.

The nature of the increase to the substrate *S* value is evident in the raw data; the rapid increase seen in the current data indicates that any positron implanted into the silicon substrate is annihilated with an *S* parameter equal or approximately equal to that of silicon – i.e., unity. The back diffusion of positrons to the low-*S* film region is thus prevented by a significant electric field (similar to that existing at the surface of p^+-Si as a result of band bending[20]), or by virtue of efficient interface trapping in large open volumes whose *S* value is unity or above, or a mixture of the two. For comparison in Fig. 1 are data for a similar 100

nm-thick film formed on the surface of a different silicon substrate. In contrast, data fitting for this second sample with VEPFIT shows that the positron diffusion back to the low-*S* film region is hardly affected by the above-mentioned factors, indicating that the dopant concentration is lower and/or there are few large trapping sites at the interface. However, for the purposes of this study, the exact cause of the rapid rise towards unity is not important, as it is the state of the TiO_2 film and the oxide-substrate interface which are of interest.

Fig. 4.2.2 shows raw data for 100 and 150nm TiO_2/p^+-Si films, as-grown and after annealing at 500ºC in vacuum and in hydrogen.

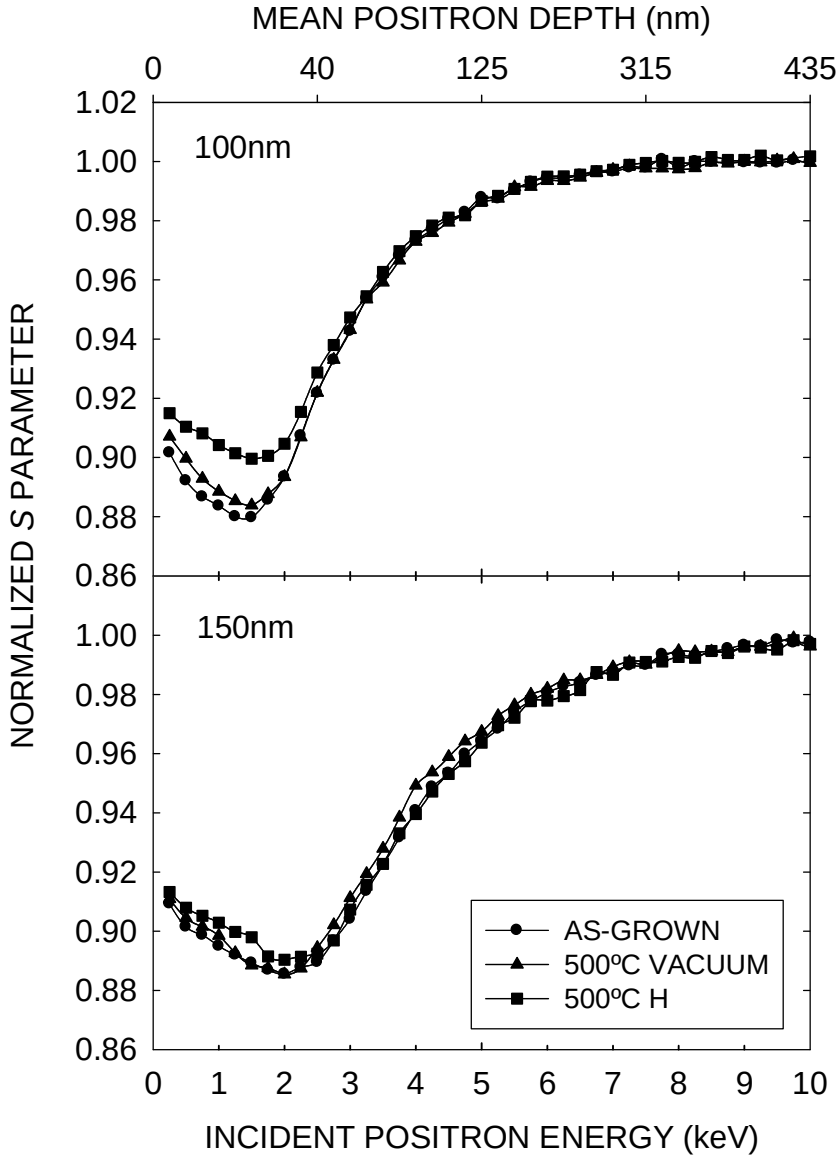

Figure 4.2.2: Normalized S(E) for 100 nm and 150 nm-thick films on p^+Si substrates, as-grown and after annealing at 500 ºC for 1 h in vacuum and in hydrogen.

The data were reproducible and the plots shown are the average of many individual measurements. The top axis shows the estimated mean positron implantation depths, taking account of the different densities of the films and substrate (4 and 2.32 gcm^{-3}, respectively); these are for guidance only, as the final data are influenced both by the spread of the positron implantation depth profile and post-implantation diffusion. All data were fitted using VEPFIT, which is especially useful for layered structures and which assigns annihilation parameters and effective positron diffusion lengths to each layer after assuming a positron implantation profile and solving the diffusion equation; interface traps and electric fields can be incorporated into the fits.

High-precision annihilation line spectra were measured for the 100nm-thick oxide sample for E = 1.5 keV – i.e., at the minimum in the $S(E)$ data of Fig. 4.2.2, for the as-grown film and after annealing in hydrogen at 500ºC. Additionally, a reference spectrum for defect-free silicon was measured. The ratios of the sample spectra to that for silicon are shown in Fig. 4.2.3. The peaks are centered at a gamma energy ~ 514.6 keV, close to that previously assigned to oxygen electrons (see, e.g., Refs. 14, 16).

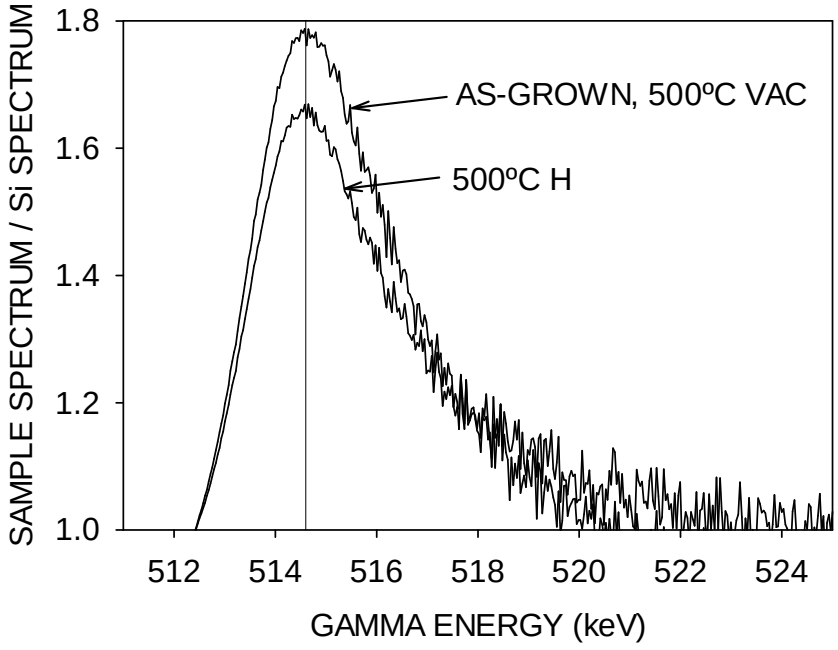

Figure 4.2.3: Ratio of annihilation line spectrum for 100 nm-thick TiO_2/p^+Si sample at 1.5 keV to that for defect-free silicon; total counts in both spectra are the same. The vertical line indicates the mean energy associated with annihilation by oxygen electrons.

4.2-IV Data Analysis and Discussion

Data for all samples could only be fit by assuming that all positrons entering the Si substrate are annihilated in the substrate – ie, they do not diffuse out of it once implanted, or they diffuse to $TiO_2/SiO_2/Si$ interface traps whose characteristic *S* value is ≥ 1, as described above. All the data were consequently fit with zero effective diffusion length in the substrate. Although satisfactory fits could be obtained by assuming that positrons diffusing in the film to the SiO_2 interface are annihilated with a high *S* – similar to that characteristic of large vacancy clusters in Si (ie ~1.13) – this is seen as much less likely, as (a) the only difference between samples whose data are shown in Fig. 4.2.2 is the dopant level in the substrate, and (b) large defects in SiO_2 are not expected to have high *S* values. Electric fields in the film or interface regions could not fit the data.

Film *S* parameters given by VEPFIT are shown in Fig. 4.2.4.

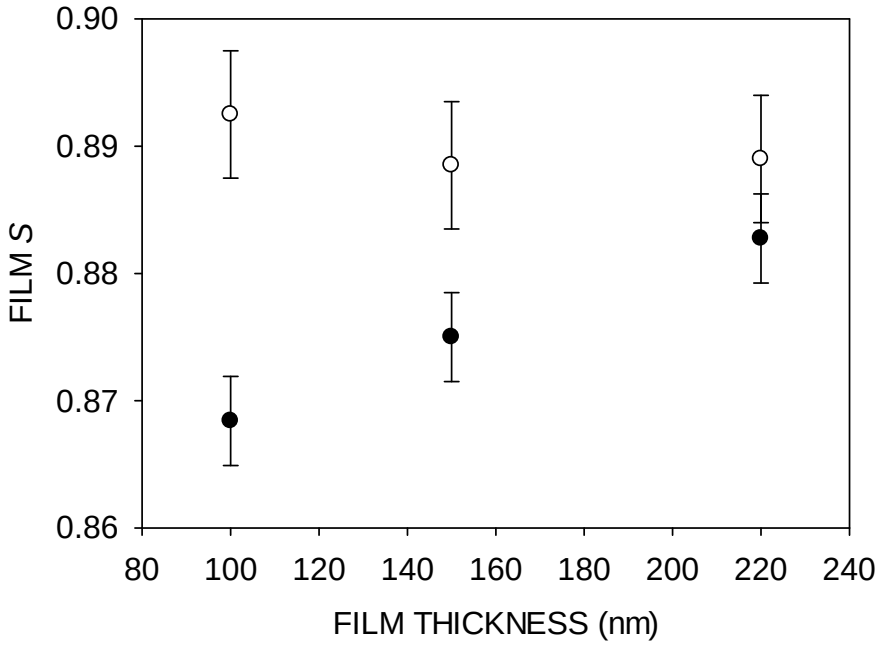

Figure 4.2.4: Fitted film S values for each film thickness. Black circles - average of as-grown and vacuum annealed samples; white circles – H_2-annealed samples.

Statistical errors on the values are negligible in the numbers as shown, but fitting uncertainties are relatively large. The film *S* value varies if small electric fields assigned to the film, with film thickness, and with fitted positron diffusion lengths. These variations arise because the films are thin and because the raw value of *S* never reaches the 'actual' bulk film

value, but rather exhibits a minimum. To account for all of these uncertainties, a systematic error bar of ± .005 is attached to each of the values shown in Fig. 4.2.4.

All the *S* values for the as-grown and vacuum-annealed samples overlap within uncertainties for each film, and so averages have been taken.

Fig. 4.2.4 shows that there is generally an increase in film *S* after annealing in H_2 (but not measurably after vacuum annealing), the increase being greatest for the thinnest film, and that there is an increase with film thickness for the as-grown and vacuum-annealed samples, but not measurably in the H_2-annealed samples.

The decrease in the oxygen peak intensity as the film is annealed, an example of which is shown in Fig. 4.2.3, is consistent with the observed increase in film *S* for the H_2-annealed sample (there is little change in the spectrum ratios for the as-grown and vac-annealed samples), confirming that the increase in *S* is associated with a decreasing sensitivity to O electrons.

This observation could be explained by the passivation of Ti vacancies, V_{Ti}, by H, with a resultant decrease in positron exposure to O electrons – positrons are expected to be trapped by V_{Ti} but not by the positively-charged V_O. However, V_O, are expected to be present in much higher concentrations than V_{Ti}[26], the latter normally being produced by prolonged oxidation. Additionally, the passivation of V_{Ti} would mean that the films would appear to the positrons to be of higher quality, and the measured *S* would thus decrease towards the value previously measured for bulk TiO_2, 0.8285. Therefore, the present observation is much more likely to reflect an increase in V_O concentration in the film after annealing in H_2. Similar increases have been seen in a number of previous studies – for example in TiO_2 nanowires after H_2 treatment between 200 and 500ºC [27] and in Cr-doped TiO_2 films.[28]

While annealing in vacuo and in H_2 have both previously been shown to lead to the creation of V_O, it is perhaps not surprising that the latter is a more efficient process. The formation energy of V_O is sample-dependent but, at a few eV,[29] suggests that annealing in vacuo at higher temperatures and for much longer times than those used in the current study would be required to produce significant concentrations of V_O in the films.[30] This provides an

explanation for the null results in the present measurements for the vacuum-annealed samples.

An increase in S has previously been attributed to an increase in oxygen vacancies in TiO_2 films.[23] It is unwise to place too much credibility on the film positron diffusion length values thrown up by VEPFIT (they do not vary much - between 12 and 20nm), so instead the values of *S* are used to estimate oxygen vacancy concentrations. The value for bulk crystalline TiO_2 was accepted to be that previously measured - 0.8285, and the defect *S* value of 0.895 derived in Ref. [2], a value which is consistent with the very low diffusion lengths measured in the films. Then the defect concentration per atom, C_D, is given by

$$\frac{(S-S_B)\lambda}{(S_D-S)\nu} \tag{1}$$

where *S* is the fitted film parameter, S_B is the bulk value (0.8285), S_D is the defect parameter (0.895), λ is the positron decay rate in undefected TiO_2 (6.76×10^9 s^{-1}) and ν is the specific trapping rate for the defect, which was assumed previously to be 10^{15} s^{-1}.

Thus C_D is obtained by

$$C_D = \frac{6.8(S-0.8285)}{(0.895-S)} x\ 10^{-6} \text{ per atom} \tag{2}$$

and, assuming an atomic number density of 3×10^{22} cm^{-3},

$$C_D = \frac{2(S-0.8285)}{(0.895-S)} x\ 10^{17}\ \text{cm}^{-3}. \tag{3}$$

This gives semi-quantitative values for C_D for the 100, 150 and 220 nm films of 3, 5 and 9 x 10^{17} cm^{-3} (as-grown/vacuum-annealed) and 5, 2 and 2 x 10^{18} cm^{-3} (H_2-annealed). The uncertainties in the absolute values of these numbers may be as high as 50%, but they give an indication of the relative changes seen.

4.2-V Conclusions - TiO_2 Films on p^+-Si

VEPAS studies of TiO_2 films grown on p^+Si substrates indicate the presence of oxygen vacancies V_O at concentrations C_D between 10^{17} and 10^{18} cm^{-3} in as-grown films, with C_D increasing with film thickness from 100 to 220 nm. No significant change in C_D is observed

after annealing at 500ºC in vacuum, but after annealing at 500ºC in a hydrogen ambient C_D increases by over an order of magnitude for the 100 nm film, by a factor of ~ 4 for the 150 nm film, and marginally for the 220 nm film. These conclusions are largely, but not totally, in agreement with a model which links V_O concentration with EL efficiency; preliminary measurements of the latter show an increase with film thickness and after annealing in vacuum or hydrogen. The enhancement of V_O concentrations in TiO_2/p^+Si heterostructures by appropriate plasma or annealing treatments thus appears to hold promise for the development of efficient solid state devices in silicon-based opto-electronics, and further work in this area is warranted.

4.3 Defects in $SrTiO_3$ films grown under different conditions

4.3-I Introduction

Thin films of perovskite oxide (ABO_3) titanate such as strontium titanate ($SrTiO_3$) are of great interest due to their use in oxide electronics such as tunable microwave devices.[31, 32, 33] The structural quality of the $SrTiO_3$ is affected by the presence of electrically active point defects, impurities and stoichiometry.[34, 35, 36]
Atomic force microscopy (AFM) is normally used to study the surface morphology. X-ray diffraction is often used to determine the c-axis parameter for the film, an indicator of the presents of defects.[36]

Variable energy positron annihilation lifetime spectroscopy (VEPALS) has previously been used to study a series of undoped $SrTiO_3$ thin films grown with varying laser fluence (energy). The positron lifetime spectra for films grown with laser energies between 90-120 mJ showed only two de-convoluted lifetime components, one attributed to the B-site cation monovacancy, the Ti-vacancy, the other to the A-site vacancy, the Sr-vacancy.[36] The intensity of trapping varied systematically towards V_{Sr} trapping with increasing laser fluence.

$SrTiO_3$ films grown by a hybrid source MBE technique have been shown to exhibit below saturation positron trapping concentrations of vacancy defects.[37] However, the use of higher growth temperatures for the series studied here may provide similar or improved film quality.

Doping has been shown to reduce the mean lifetime in VEPALS measurements. A preliminary study of Fe-doped $SrTiO_3$ has observed an unexpected low mean lifetime value from a highly doped (10%) film, the c-axis expansion is large so the film is defective but the lifetime of the dominant positron trapping vacancies must be low.[38] Nb-doped $SrTiO_3$ crystals can provide a potentially superior alternative to undoped $SrTiO_3$ single crystals, which are known to still contain cation vacancies.[39]

VEPAS has been used to investigate vacancy-type defects in the model perovskite oxide $SrTiO_3$. A main focus is the characterisation of the pulsed laser deposited (PLD) $SrTiO_3$ thin films grown at Forschungszentrum Jülich.

4.3-II Experimental Procedure

Measurements were performed on thin films (~200 nm) of $SrTiO_3$ deposited by PLD on $SrTiO_3$.

Samples created using an older PLD system include a series of doped (2% Fe) $SrTiO_3$ thin films grown with varying laser fluence (60, 80, 100, 120 mJ) and an Fe-doping sequence varying from 0.1 to 10% Fe using a laser fluence of 100 mJ. As-received and Nb-doped substrates were measured for reference. The new PLD system samples, grown at Forschungszentrum Jülich, also contained an Fe-doped series grown at 800ºC varying from 0.5 to 5%. Two undoped series were also measured, one where the growth pressure was varied 10^{-1} to 10^{-6} Torr, and one where the substrate temperature was varied from 650ºC to 1050ºC. A series of $SrTiO_3$ substrates with varying Nb-doping levels was also studied.
All samples were investigated with VEPAS with incident positron energies, *E*, varying from 0.25 to 30 keV. Both *S* and *W* parameters were used to analyse data with *S*-*W* plots revealing different trapping states. The data were all normalized to the same count rate as all sample sizes were comparable to the beam width.

4.3-III Results and Discussion

Old PLD System

Differences in the quality of the $SrTiO_3$ films with varying laser fluence was investigated with four samples created with laser energies 60, 80, 100 and 120 mJ. All four samples were

doped with the same 2% Fe so differences were due only to the laser energy. *S*(*E*) results can be seen in Fig. 4.3.1.

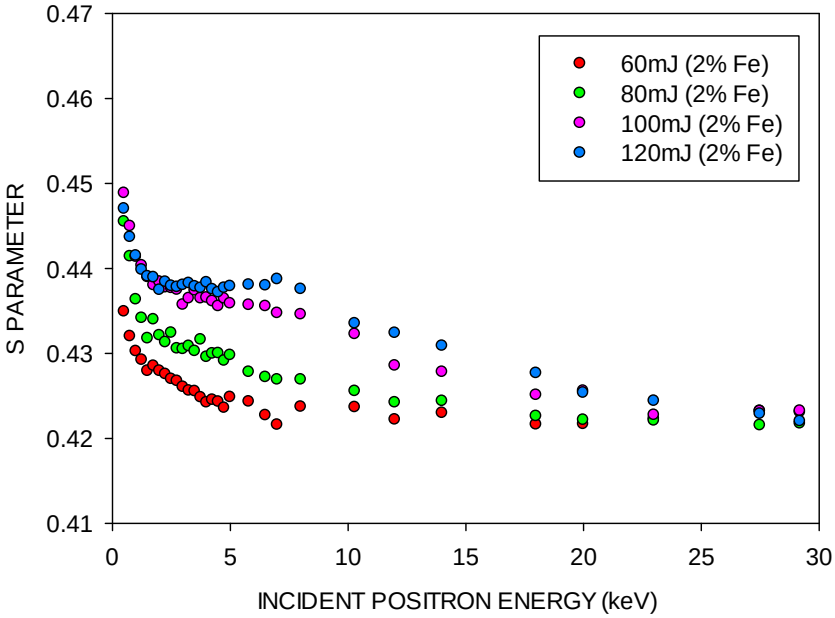

Figure 4.3.1: S(E) data for 2% Fe-doped $SrTiO_3$ thin films grown with varying laser fluence.

A response to the film can be seen in all samples as an inflection in the *S*(*E*) curve at around 4 keV. At higher energies this inflection becomes a plateau meaning that all positrons implanted between 2 and 6 keV are trapped and annihilate within the film. The lower the laser fluence the less pronounced, or trapping, the film seems to become. To investigate further the changes in the films, the *S*-*W* data was plotted and can be seen in Fig. 4.3.2.

Although the actual state points cannot be deduced from the plot, there are still three distinct states visible – surface, bulk $SrTiO_3$ and open-volume defects in $SrTiO_3$. The surface and open-volume points lie on the same line meaning that positrons trapping in open-volume are annihilating with oxygen electrons, as is normal for a surface response, but with a higher probability since the *S* parameter is depressed. The 60 mJ film that appeared to be the least defected in the *S*(*E*) plot still has some response to open-volume defects and also shows a defected bulk response.

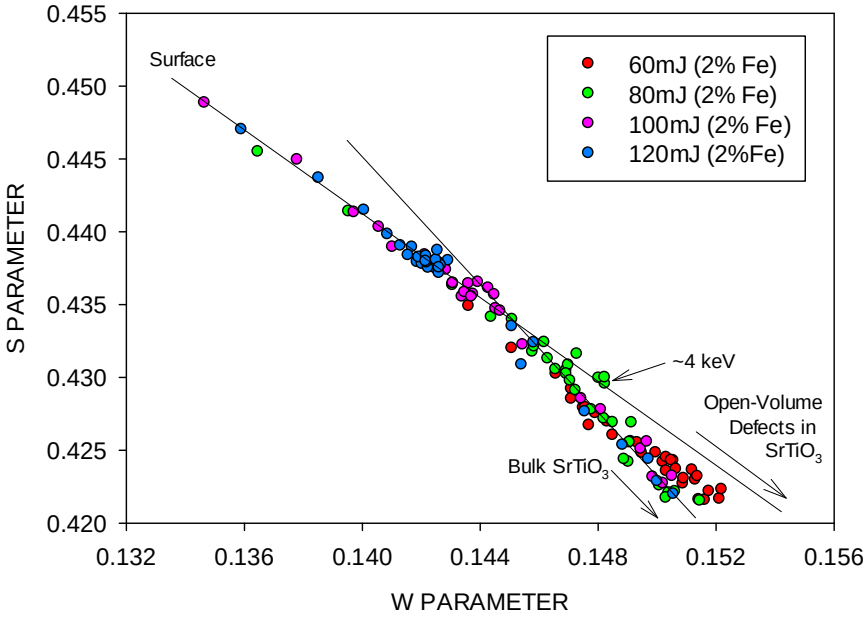

Figure 4.3.2: S-W data for 2% Fe-doped $SrTiO_3$ thin films grown with varying laser fluence.

Two reference samples, created with the old PLD system, one undoped and one Nb-doped are compared in the *S*(*E*) plot in Fig. 4.3.3.

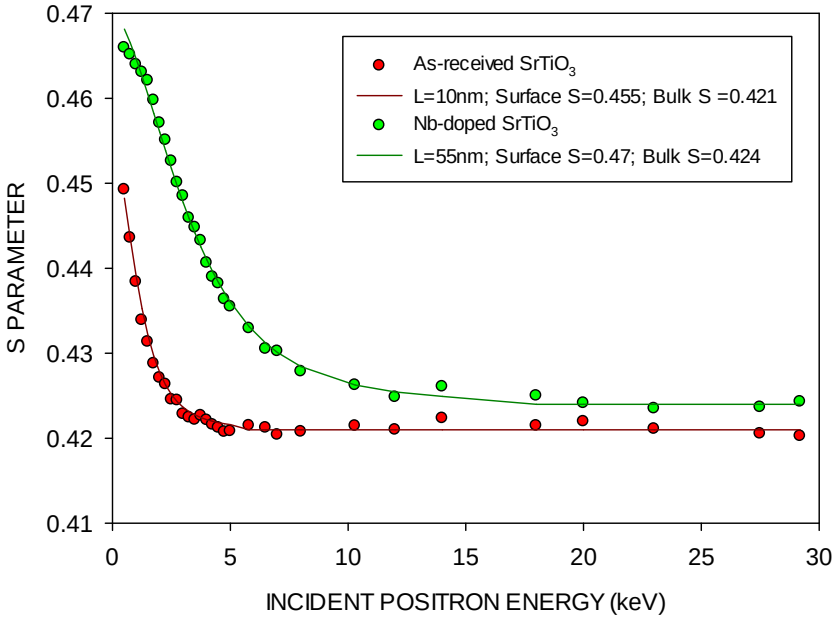

Figure 4.3.3: S(E) for standard and Nb-doped $SrTiO_3$ substrates.

Both samples can be fit as a single-layer but Nb-doping has the effect of increasing the positron diffusion length, *L*, indicating an improved film quality.

Comparison between old and new PLD system

Using two Fe-doped series, one created with the old PLD system and one created with the new PLD system, a direct comparison into the quality of the films each produced was performed. Figs. 4.3.4 and 4.3.5 show results from the old PLD system.

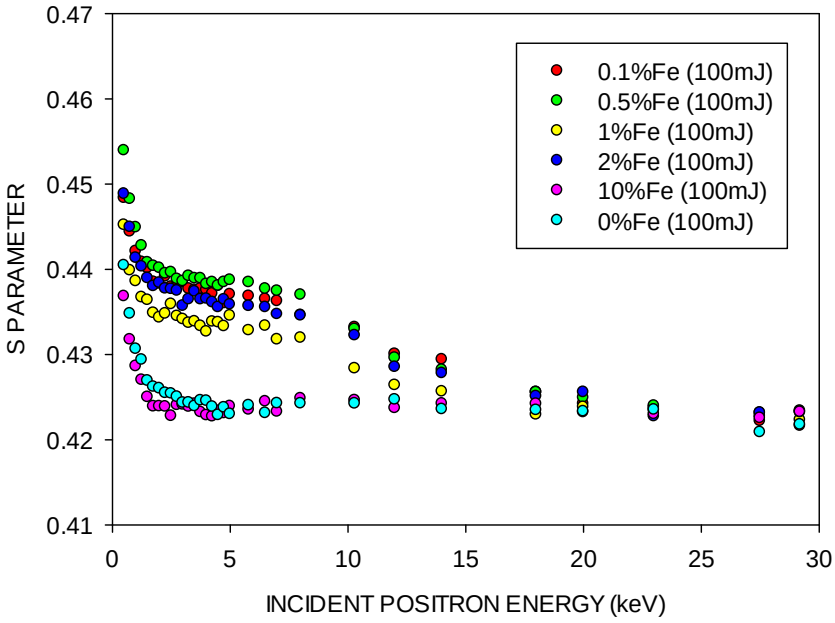

Figure 4.3.4: S(E) for the set of samples studying Fe-doping with the old PLD system.

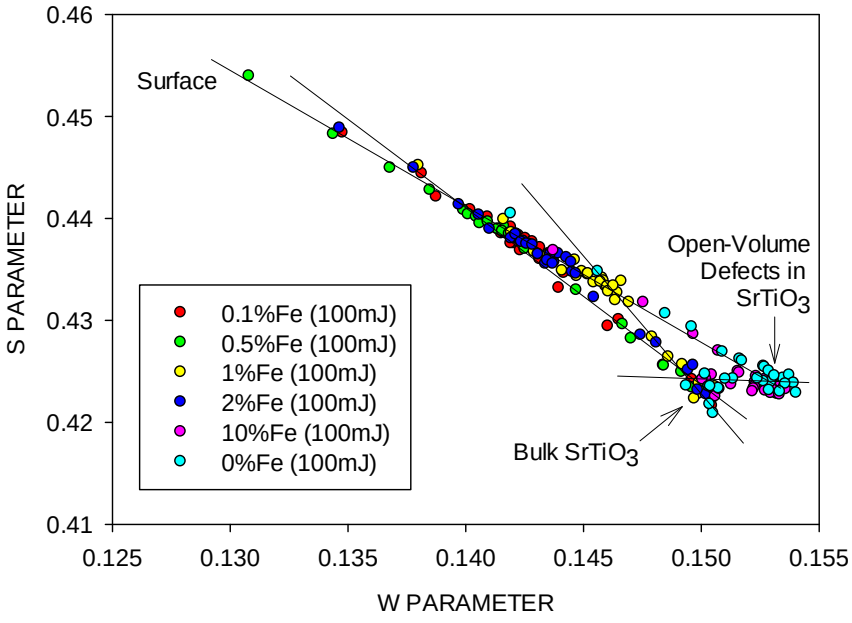

Figure 4.3.5: S-W plot for the set of samples studying Fe-doping with the old PLD system.

Samples were doped with Fe ranging from 0 – 10% and all samples were created using a laser fluence of 100 mJ. There appears to be little correlation between the % doped and *S*

parameter. While 0 and 10% Fe appear to have the least film response, Fig. 4.3.5 shows that these films contain the greatest response to open-volume defects.

Figs. 4.3.6 and 4.3.7 show results from the new PLD system.

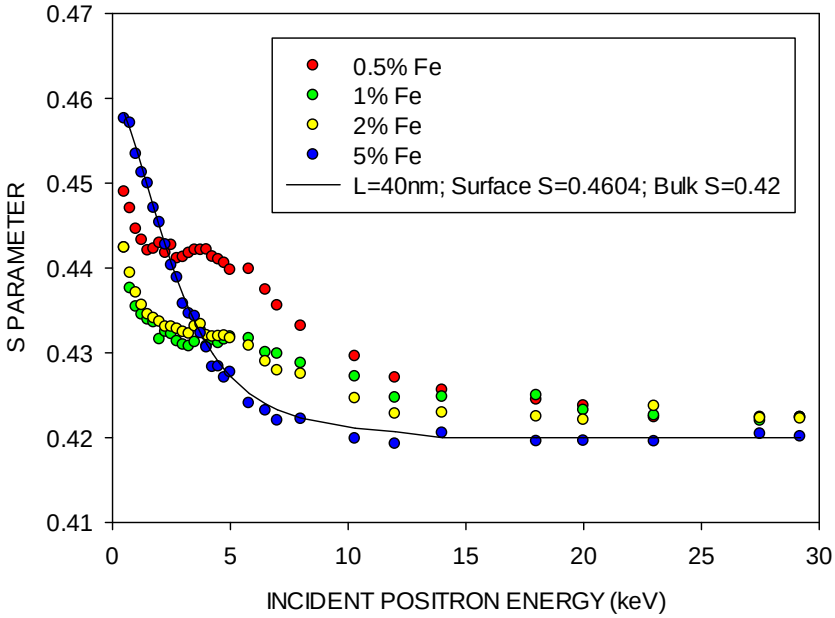

Figure 4.3.6: S(E) for the set of samples studying Fe-doping with the new PLD system; best-fit positron diffusion length, L, is shown for 5% Fe.

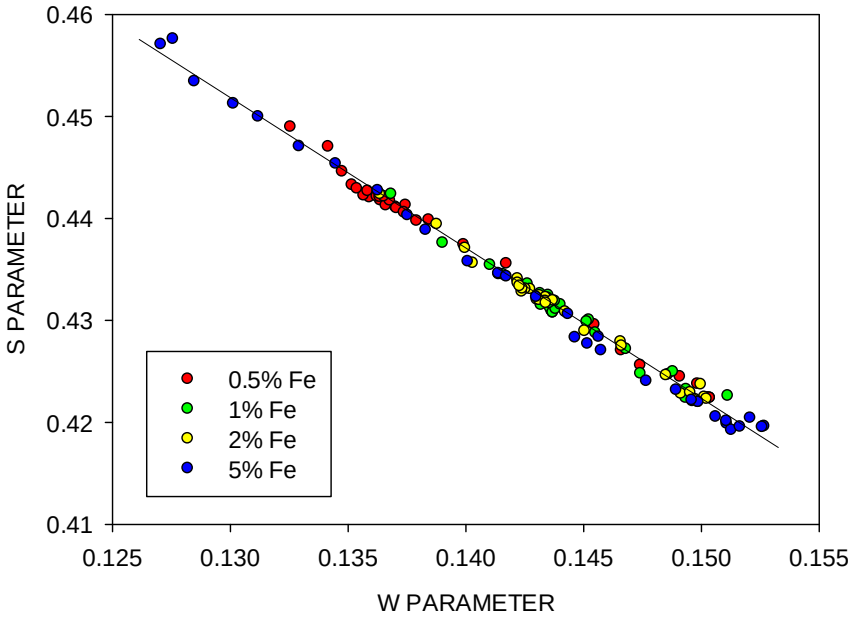

Figure 4.3.7: S-W plot for the set of samples studying Fe-doping with the new PLD system.

Samples doped between 0.5 – 2% Fe have $S(E)$ curves, seen in Fig. 4.3.6, similar to those created with the old PLD system. However, doping at 5% Fe appears to create a film that

positrons can no longer distinguish from bulk. Fitting to a single layer gives a positron diffusion length, *L*, of ~40 nm, consistent with previous studies of perovskite oxide materials.[40] Another difference can be seen when plotting the data as an *S*-*W* plot, seen in Fig. 4.3.7.

All data points lay on same line, meaning that the samples only have two states - surface and bulk $SrTiO_3$. There is no evidence of open volume defects in any of the films, as was the case with the old PLD system. The new PLD system produces films of a higher quality, with Fe doping increasing the quality further.

New PLD System

The effects of film growth ambient pressure were investigated with samples created with the new PLD system. Films were grown under pressures ranging from 10^{-1} to 10^{-6} Torr, resulting *S*(*E*) data can be seen in Fig. 4.3.8.

At the highest and lowest pressures, 10^{-1} and 10^{-4} to 10^{-6} Torr, inflections in the *S*(*E*) curve can be seen at ~4 keV. The lowest pressure, 10^{-6} Torr, also shows damage much further into the sample. At 10^{-2} and 10^{-3} Torr the ambient pressure starts to enable the growth of better

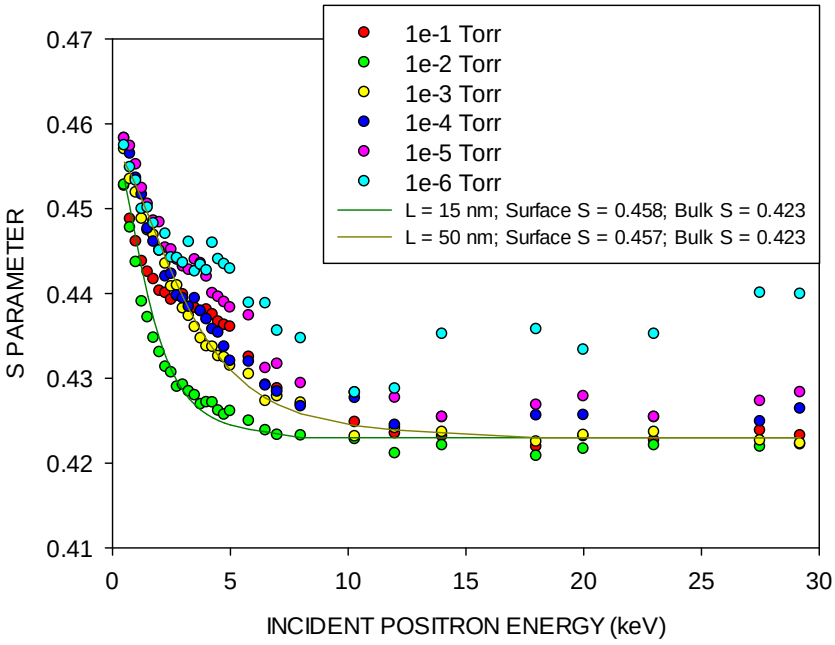

Figure 4.3.8: S(E) plot for samples involving systematic variation in the growth ambient pressure for pure $SrTiO_3$ on $SrTiO_3$ using the new PLD system.

quality films, with 10^{-3} Torr being the optimal pressure. Fig. 4.3.9 shows that only at the highest pressure, 10^{-1} Torr, open volume defects were created. The *S-W* data was normalized for minor drifts in *S* parameter.

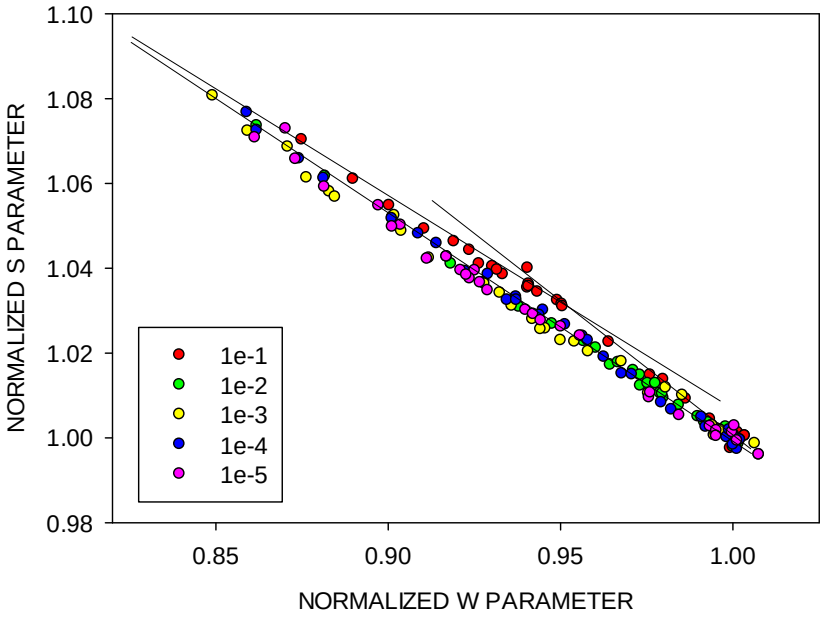

Figure 4.3.9: Normalized S-W plot for samples involving systematic variation in the growth ambient pressure for pure $SrTiO_3$ on $SrTiO_3$ using the new PLD system.

The effects of doping the $SrTiO_3$ substrate with Nb using the new PLD system were also investigated. Single crystals of $SrTiO_3$ were used for the following experiment.

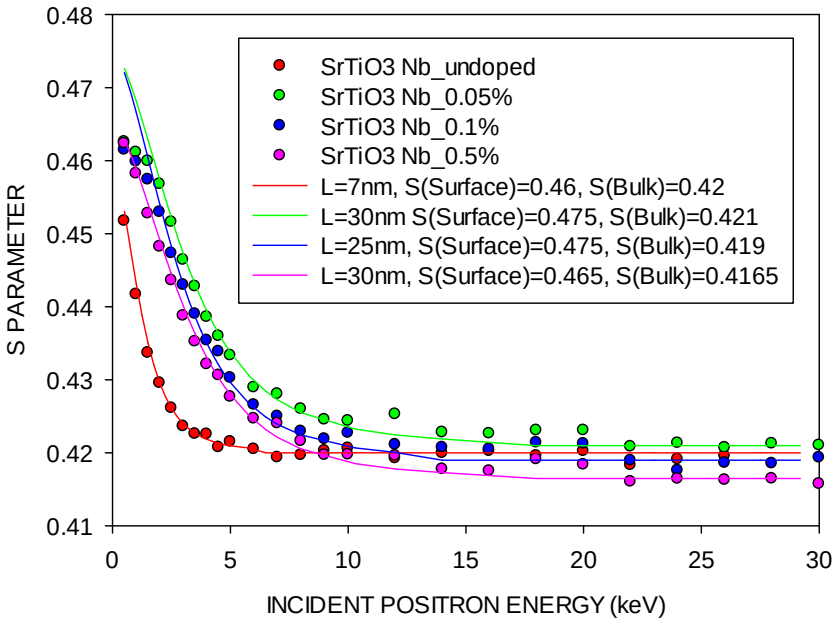

Figure 4.3.10: S(E) plot for the series of $SrTiO_3$ substrates with varying Nb-doping levels; positron diffusion lengths, L, and fitted S parameters are also shown.

Fig. 4.3.10 shows a large change in the positron diffusion length with just 0.05% doping, from ~7 nm undoped to ~30 nm. As in Fig. 4.3.3 for the old PLD system there is an increase in the quality of the film when doped with Nb. Nb-doped $SrTiO_3$ crystals contains fewer defects than the undoped $SrTiO_3$ single crystals as the Nb atoms fill cation vacancies. The effect of increasing the Nb doping levels beyond 0.05% appears to have little change on the positron diffusion length.

A previous study of high temperature PLD grown $SrTiO_3$ has shown a significant improvement in film quality.[3]

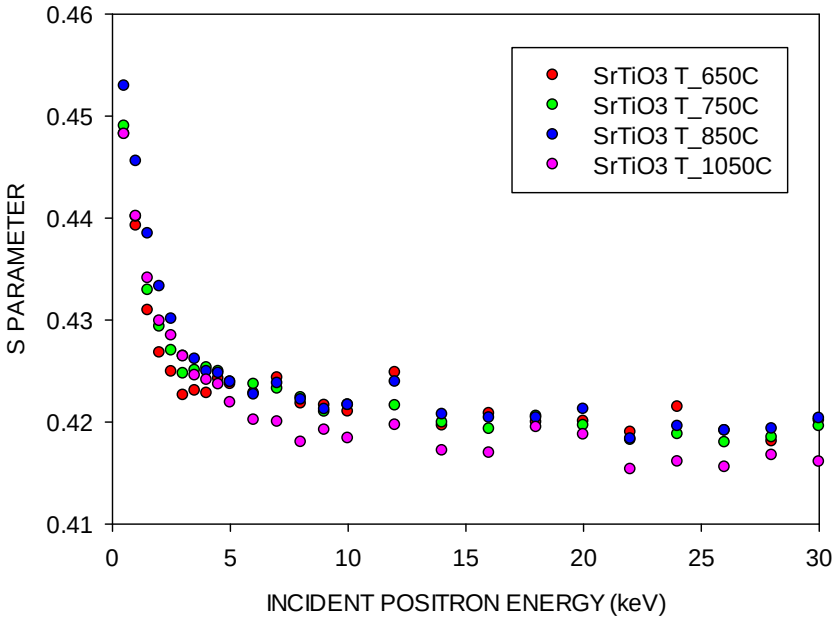

Figure 4.3.11: S(E) plot for the series where the substrate temperature was varied during film growth.

The data in Fig. 4.3.11 show very little change in the *S*(*E*) curves with temperature. Any improvements in the film quality are below the resolution of the VEPAS technique.

4.3-IV Conclusions - $SrTiO_3$ Films

The best quality pulsed laser deposited (PLD) $SrTiO_3$ thin films are those grown at Forschungszentrum Jülich. The positron diffusion length was used to determine the quality of the film where diffusion lengths of 40-50 nm indicated little trapping and the best quality. The longest diffusion lengths were obtained from films grown with a pulsed laser of lowest influence, doped with >0.05% Nb or 5% Fe at a growth ambient pressure of 10^{-3} Torr.

[1] B. Hoex, J. J. H. Gielis, M. C. M. van de Sanden, and W. M. M. Kessels, J. Appl. Phys. **104**, 113703 (2008).

[2] Y. Y. Zhang, X. Y. Ma, P. L. Chen, D. S. Li, and D. R. Yang, Appl. Phys. Lett. **94**, 061115:1 (2009).

[3] Y. Kozuka, M. Kim, H. Ohta, Y. Hikita, C. Bell, and H. Y. Hwang, Applied Physics Letters **97** (22), 222115 (2010).

[4] M. J. Chen, Y. T. Shih, M. K. Wu, and F. Y. Tsai, J. Appl. Phys. **101**, 033130 (2007).

[5] J. Benick, A. Richter, T. -T.A. Li, N. E. Grant, K. R. McIntosh, Y. Ren, K. J. Weber, M. Hermle, and S. W. Glunz, Conference Record of the 35th IEEE Photovoltaic Specialists Conference, Honolulu, USA, 891 (2010).

[6] T. -T.A. Li, S. Ruffell, M. Tucci, Y. Mansoulié, C. Samundsett, S. D. Iullis, L. Serenelli, and A. Cuevas, Sol. Energy Mater. **95**, 69 (2011).

[7] J. Dekker, K. Saarinen, H. Ólafsson, and E.O. Sveinbjörnsson, Appl. Phys. Lett. **82**, 2020 (2003).

[8] M. Mackawa, A. Kawasuso, M. Yoshikawa, A. Miyashita, R. Suzuki, and T. Ohdaira, Phys. Rev. B **73**, 014111 (2006).

[9] P. G. Coleman, C. P. Burrows, R. Mahapatra, and N. G. Wright, J. Appl. Phys. **102**, 014106 (2007).

[10] G. Agostinelli, A. Delabie, P. Vitanov, Z. Alexieva, H. F. W. Dekkers, S. De Wolf, and G. Beaucarne, Sol. Energy Mater. Sol. Cells **90**, 3438 (2006).

[11] P. G. Coleman, N. B. Chilton, and J. A. Baker, J. Phys.: Condens. Matter **2**, 9355 (1990).

[12] F. Werner, B. Veith, D. Zielke, L. Kühnemund, C. Tegenkamp, M. Seibt, R. Brendel, and J. Schmidt, J. Appl. Phys. **109**, 113701 (2011).

[13] B. Hoex, S. B. S. Heil, E. Langereis, M. C. M. van de Sanden, and W. M. M. Kessels, Appl. Phys. Lett. **89**, 042112 (2006).

[14] U. Myler and P. J. Simpson, Phys. Rev. B **56**, 14303 (1997).

[15] R.S. Brusa, W. Deng, G.P. Karwasz, A. Zecca, and D. Pliszka, Appl. Phys. Lett. **79**, 1492 (2001).

[16] S. Szpala, P. Asoka-Kumar, B. Nielsen, J.P. Peng, S. Hayakawa, K.G. Lynn, and H.-J. Gossmann, Phys. Rev. B **54**, 4722 (1996).

[17] A. P. Knights, F. Malik, and P. G. Coleman, Appl. Phys. Lett. **75**, 466 (1999).

[18] A. van Veen, H. Schut, and P. E. Mijnarends, in Positron Beams and Their Applications, ed. P. G. Coleman, p. 191 (Singapore: World Scientific, 2000).

[19] T. T. Li and A. Cuevas, Phys. Status Solidi RRL **3**, 160 (2009).

[20] J. A. Baker, P. G. Coleman, and N. B. Chilton, Vacuum **41**, 1593 (1990).

[21] T. L. Thompson and J. T. Yates Jr, Chem. Rev. **106**, 4428 (2006).

[22] X. Kong, C. Liu, W. Dong, X. Zhang, C. Tao, L. Shen, J. Zhou, Y. Fei, and S. Ruan, Appl. Phys. Lett. **94**, 123502:1 (2009).

[23] Y. Y. Zhang, X. Y. Ma, P. L. Chen, D. S. Li, X. D. Pi, D. R. Yang, and P. G. Coleman, Appl. Phys. Lett. **95**, 252102:1 (2009).

[24] R. Mahapatra, N. Poolamai, S. Chattopadhyay, N. G. Wright, A. K. Chakroborty, K. S. Coleman, P. G. Coleman, and C. P. Burrows, Appl. Phys. Lett. **88**, 072910:1 (2006).

[25] A. van Veen, H. Schut, J.de Vries, R.A. Hakvoort, and M. R. Ijpma, AIP Conf. Proc. **218**, 171 (1990).

[26] M. K. Nowotny, T. Bak, J. Nowotny, and C. C. Sorrell, Phys. Stat. Sol. B **242**, R88 (2005).

[27] Gongming Wang et al., Nano Letts. **11**, 3026 (2011).

[28] Lifeng Liu, Jinfeng Kang, Yi Wang, Xing Zhang, and Ruqi Han, Jpn. J. Appl. Phys. **47**, 8787 (2008).

[29] A. Janotti, J. B. Varley, P. Rinke, N. Umezawa, G. Kresse, and C. G. Van de Walle, Phys. Rev. B **81**, 085212 (2010).

[30] Koji Iijima et al., J. Luminescence **128**, 911 (2008).

[31] M. J. Lancaster, J. Powell, and A. Porch, Supercond. Sci. Technol. **11**, 1323 (1998).

[32] C. H. Ahn, J. M. Triscone, and J. Mannhart, Nature (London) **424**, 1015 (2003).

[33] J. H. Haeni et al., Nature (London) **430**, 758 (2004).

[34] Z. Yu, C. Ang, R. Y. Guo, A. S. Bhalla, and L. E. Cross, Appl. Phys. Lett. **80**, 1034 (2002).

[35] D. J. Keeble, R. A. Mackie, W. Egger, B. Löwe, P. Pikart, C. Hugenschmidt, and T. J. Jackson, Physical Review B **81** (6), 064102 (2010).

[36] D. J. Keeble, S. Wicklein, R. Dittmann, L. Ravelli, R. A. Mackie, and W. Egger, Physical Review Letters **105** (22), 226102 (2010).

[37] D. J. Keeble, B. Jalan, L. Ravelli, W. Egger, and G. Kanda et al., Appl. Phys. Lett. **99**, 232905 (2011).

[38] David J Keeble, presented at the Defect and Diffusion Forum, 2012 (unpublished).

[39] R. A. Mackie, S. Singh, J. Laverock, S. B. Dugdale, and D. J. Keeble, Physical Review B **79** (1), 014102 (2009).

[40] Akira Uedono, Kazuo Shimoyama, Masahiro Kiyohara, Zhi Quan Chen, Kikuo Yamabe, Toshiyuki Ohdaira, Ryoichi Suzuki, and Tomohisa Mikado, Journal of Applied Physics **91** (8), 5307 (2002).

[41] Akira Uedono, Kazuo Shimayama, Masahiro Kiyohara, Zhi Quan Chen, and Kikuo Yamabe, Journal of Applied Physics **92** (5), 2697 (2002).

Chapter 5

Vacancies in Silicon, Silicon Dioxide and Silicon-Germanium

"[He was] a solemn, unsmiling, sanctimonious old iceberg who looked like he was waiting for a vacancy in the Trinity."

- Mark Twain

While the evolution of vacancy-type defects in silicon is of fundamental interest,[1] their control has long played an important role in the development of useful device structures,[2] for example, in gettering metallic impurities,[3] wafer separation,[4] and the suppression of dopant diffusion.[5, 6, 7] In this chapter, the role vacancies play in various silicon, silica and other silicon-type devices is investigated. This includes the trapping effects of vacancies in silica; how monovacancies can survive in divacancies more readily in chain-implanted samples than in single-shot-implanted samples; how the depth profile of implanted ions creates two regions, one of undecorated vacancies and FV complexes and one of just FV complexes independently of sample structure; how lifetimes and populations of different charge states in V_2 behave in a biased diode; monitoring luminescence suppressing defects; and identifing significant structural differences between the two Si/SiO_2 interfaces in a quantum well.

5.1 Evolution of vacancy-type defects in silicon-on-insulator structures

5.1-I Introduction

Kalyanaraman et al.[8 9] used Au labeling to study the formation of nanovoids in Si. The aim of the current research is to investigate the evolution of vacancy-type defects in Si with annealing temperature, from divacancies in as-implanted samples through small clusters of *n* vacancies V_n (n = 3–6) to nanovoids, using the technique of variable-energy positron annihilation spectroscopy (VEPAS). Of particular interest is the comparison of this vacancy evolution in the equivalent topmost Si layers in Si and silicon-on-insulator (SOI) samples.

In order to optimize the creation of excess vacancies in a near-surface Si layer by Si ion implantation an SOI structure is employed, so that the Si ions which create the vacancies are implanted into the buried oxide (BOX) layer comprising SiO_2. This process creates an excess vacancy concentration in the top Si layer by isolating excess interstitials either within or beyond the BOX layer.[8, 9, 10]

5.1-II Experimental Procedure

Various Si ion doses (10^{13}, $5x10^{13}$, 10^{14} and $5x10^{14}$ cm^{-2}) were implanted at the same energy (2 MeV) into Czochralski (Cz) Si and SOI samples at the University of Surrey Ion Beam Centre. The SOI samples consist of a 1 μm layer of silica grown in-between a silicon substrate and a 1.5 μm top silicon layer. This type of sample is made by the SmartCut® technique and is generically called silicon on insulator (SOI). Using the layer information and implantation energy SRIM (The Stopping and Range of Ions in Matter) simulations[11] determine that over 90% of the Si ions are implanted into the SiO_2 layer (Figure 5.1.1) using a quantum mechanical treatment of ion-atom collisions.

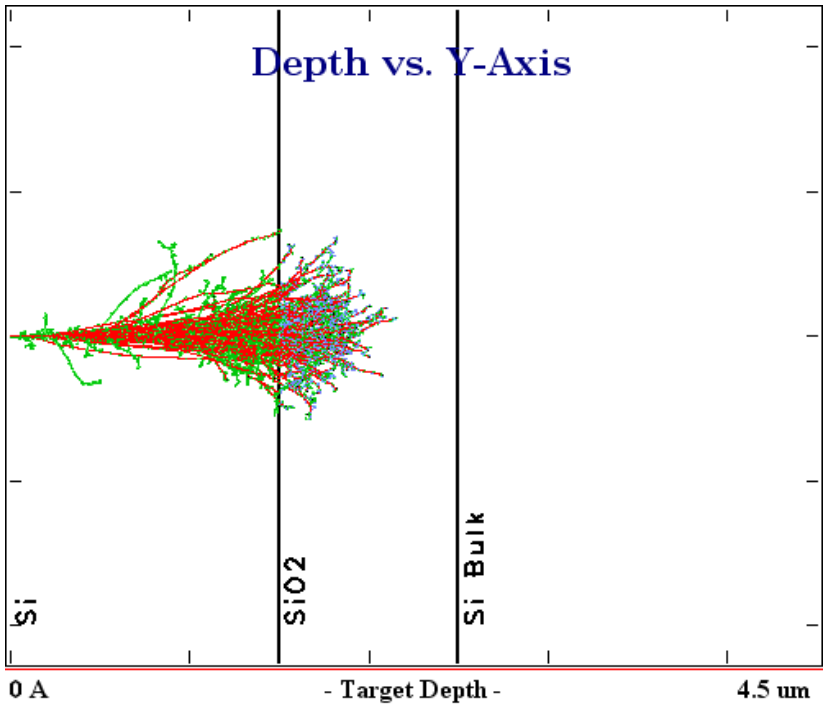

Figure 5.1.1: SRIM calculation of the Si ion implantation into the SOI samples. Ion distribution (red) with recoils (green) are shown.

The same doses were also implanted into a pure crystalline silicon sample within the same depth region. These eight samples were initially annealed to 600 ºC to study the resultant defect evolution in both types of sample (SOI and Si).

5.1-III Results and Discussion

Measurements were first taken of the SOI and Si samples with the highest Si ion dose ($5x10^{14}$ cm^{-2}) as this should have caused the most damage and therefore a greater change in the *S* parameter. Fig. 5.1.2 shows the raw data for these two samples:

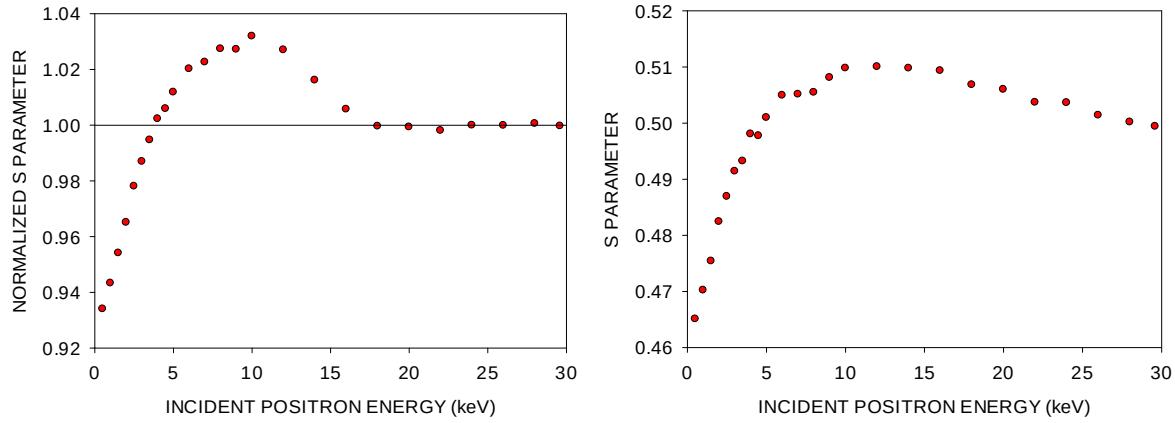

Figure 5.1.2: Normalised S parameter for SOI (left) and Si (right).
Both are for the sample implanted with 5e14 cm^{-2} Si ions after annealing at 600 ºC

In the left graph of Fig. 5.1.2 the SOI sample has a high-*S* damaged region at around 10 keV. Using the equation

$$z_0(nm) = \frac{33}{\rho(g/cm^3)}.E(keV)^{1.6} \qquad (1)$$

this region is ~0.6 μm into the sample and thus the high *S* must be a result of damage caused in the top Si layer by the ion implantation. At the higher implantation energies (25 – 30 keV) the average positron depth is beyond both the top Si and SOI layers and this is shown as a saturated unchanging *S* parameter. As the positrons are annihilating with the bulk Si substrate the average *S* parameter in this region can be used to normalise the rest of the data by setting it to unity. *S(E)* for the SOI samples implanted with Si ions at all four doses and annealed at 600 ºC can be seen in Fig. 5.1.3.

The SOI samples in Fig. 5.1.3 show that as the implantation dose decreases so too does the *S* parameter response in the top Si layer, indicating less damage being caused here. The response from the silica layer is also revealed at ~17 keV as the dose decreases. The *S* parameter is less than one in this region due to the oxygen valence electrons, which have a higher momentum than in silicon. This could be revealed due to the ability of the positrons to diffuse to the silica layer without encountering as much damage (a longer diffusion length).

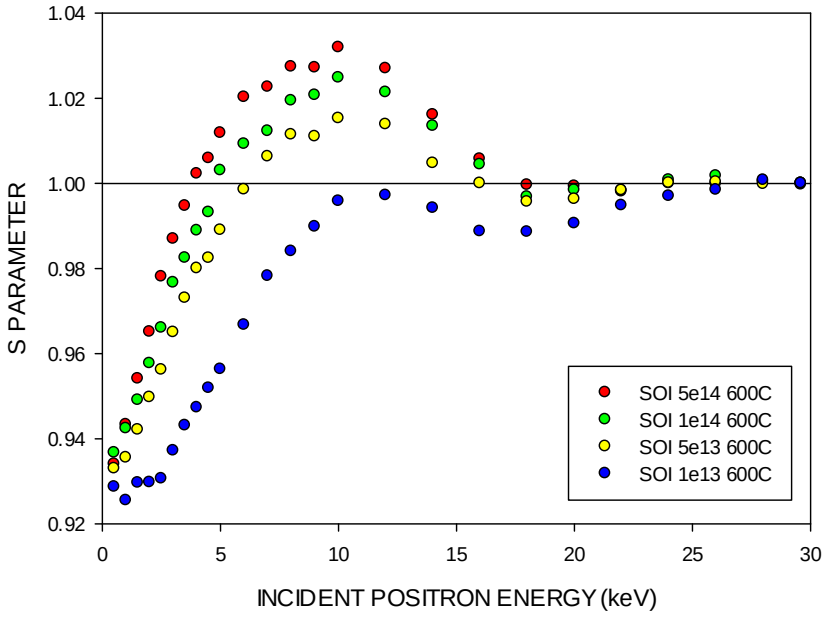

Figure 5.1.3: Normalised S parameter for SOI (all doses) after annealing at 600 ºC

S(E) for the Si samples are shown in Fig. 5.1.4. In the Si (right) graph of Fig. 5.1.2 and in Fig. 5.1.4 *S(E)* for the implanted Si sample does not reach the bulk plateau. Instead positrons are still diffusing to a damaged region at the highest energies. To normalise this data to a bulk Si *S* parameter a separate measurement for unimplanted Si was needed. It was found, however, that the changes in the *S* parameter over time were larger than the actual changes in *S* between some samples. A solution to this problem was the development of a technique to almost simultaneously measure *S* for both the implanted Si and bulk Si to find what the normalised *S* should be at 30 keV. The method for this normalisation technique can be found in Chapter 3.2 and was repeated for all four Si samples; it was applied to the data for Si in Figs. 5.1.2 and 5.1.4.

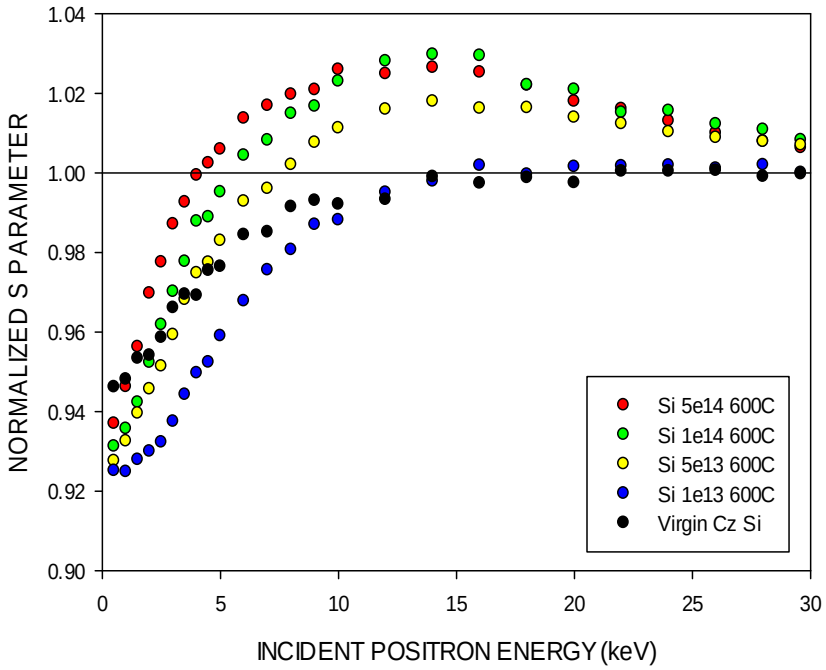

Figure 5.1.4: Normalised S parameter for Si (all doses) after annealing at 600 ºC

Fig. 5.1.4. again shows a reduced *S* parameter response with decreased dose. The lowest dose (10^{13} cm^{-2}) shown in blue actually has a similar response to crystalline Si shown in black. Annealing at 600 ºC has removed most of the little damage present within this sample. The discrepancy at 0.5 - 10 keV is probably due to a lower surface *S* parameter in the implanted Si sample from oxidation. All samples were then annealed to 700 ºC for ~20 min and re-measured:

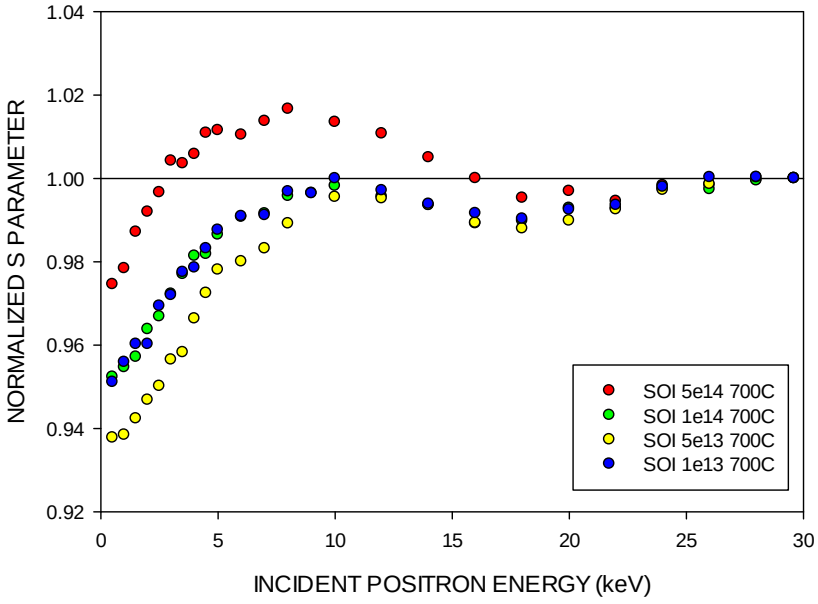

Figure 5.1.5: Normalised S parameter for SOI (all doses) after annealing at 700 ºC

The SOI samples in Fig. 5.1.5 still appear to have damage in the top Si layer, certainly for the highest dose and potentially for the lower doses where their surface *S* parameters 'pull' the average *S* below 1. The results for the highest dose sample are interesting in that the VEPFIT fitting shows a combination of low *S* and low *L* (the positron diffusion length) in the top Si layer. This unrealistic fit could be explained by large voids that trap the positrons, causing a low *L*, which would then annihilate on an inner clean Si "surface", causing the low *S*.

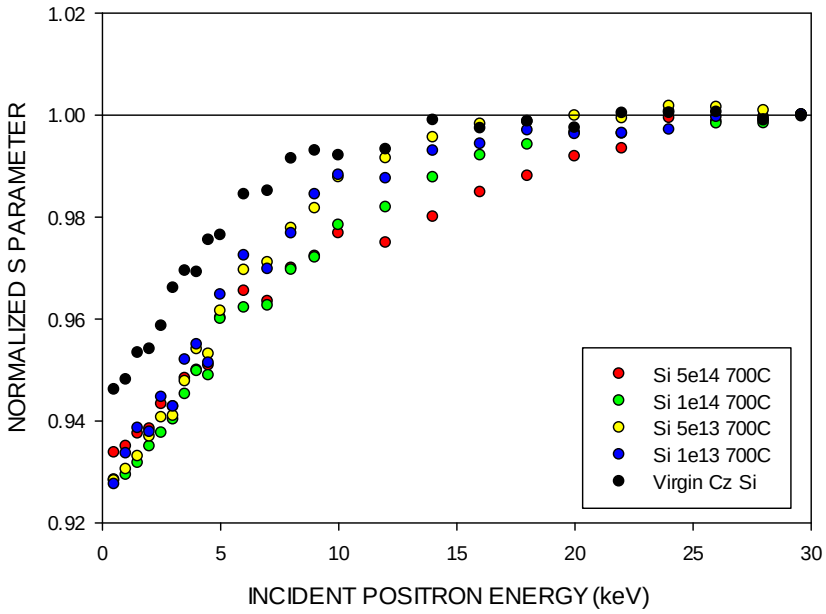

Figure 5.1.6: Normalised S parameter for Si (all doses) after annealing at 700 ºC

The implanted Si samples in Fig. 5.1.6, however, appear to have had most of their damage annealed away. Data for crystalline Si is shown to compare. The similar shapes confirm that there is very little/no damage left in the top layer, where the only differences are caused by the surface *S* parameters. Because of this, only the SOI samples were annealed further to 800 ºC for ~20 min and again re-measured:

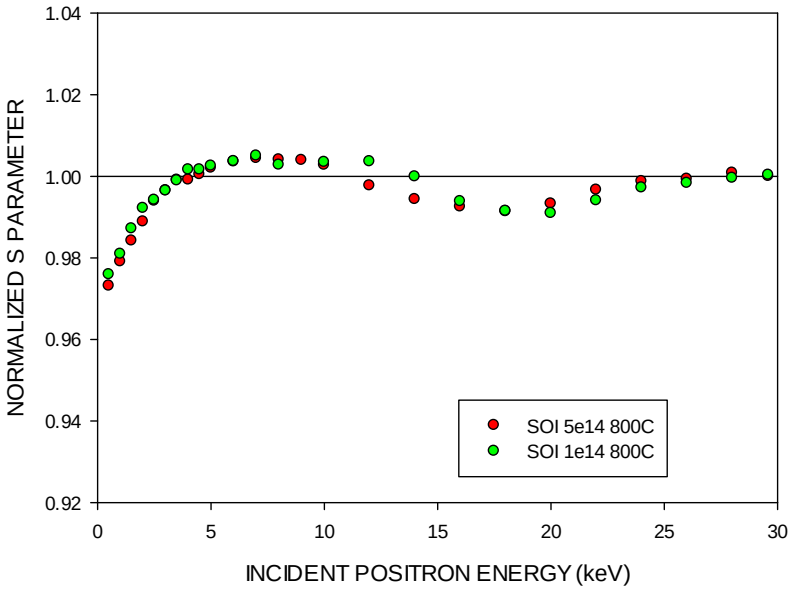

Figure 5.1.7: Normalised S for SOI ($5x10^{14}$ and 10^{14}) after annealing at 800 ºC

Only data for the two largest doses are shown in Figure 5.1.7 since their shapes are nearly identical. The *S* parameters in the top layer of both samples show little/no damage left. It was for this reason that it was assumed that the lower dose, lower damage samples would look similar. To test whether there was actually any damage left in these two samples hydrofluoric acid (HF) was used to etch off the surface oxide layer. In doing this positrons would be more sensitive to any damage in the Si rather than in the oxide. Results are shown in Figure 5.1.8:

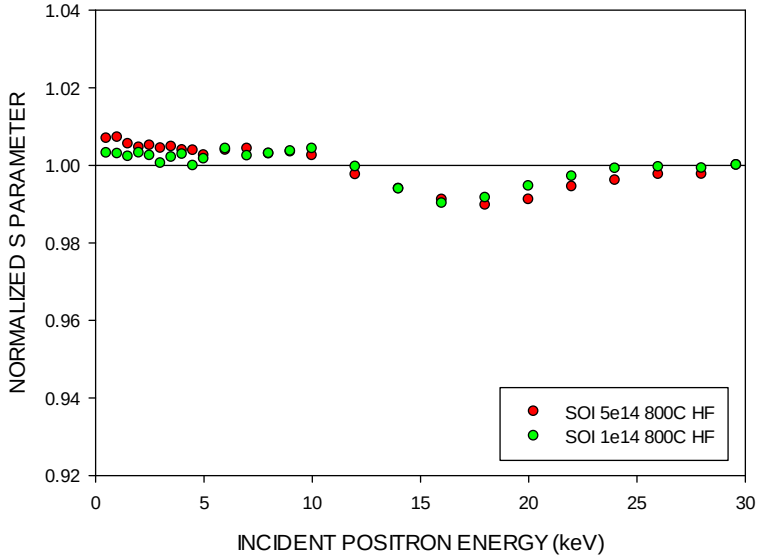

Figure 5.1.8: Normalised S parameter for SOI ($5x10^{14}$ and 10^{14}) after annealing at 800 ºC and HF etching

Removing the surface oxide confirmed that the top Si layers in both samples have no damage or such low concentrations of defects that positrons are no longer sensitive to their effects.

5.1-IV Data Analysis And Discussion

The most dramatic change was seen after annealing at 700ºC. In all Si samples there is effective annealing of all vacancy-type damage to levels below the VEPAS sensitivity limit. However, in the top Si layer in the SOI samples there is evidence of some residual vacancy response in the low-fluence samples. This is most evident in the raw data for the highest-fluence sample (Fig. 5.1.5) where the vacancy damage has evolved so that the average *S* value in the layer is 1.015, *L* = 50 nm. This combination of *S* and *L* (in which both have small values) is not consistent with trapping by defects of any size up to the maximum identifiable by VEPAS (~V_{20}). One cannot invoke near-surface or interface electric fields to explain the data, as the same short *L* is not seen in the lower fluence SOI nor in any of the Si samples. The only remaining possibility is that a high fraction of the small vacancy clusters in the top Si layer have agglomerated to form voids or small cavities. In a VEPAS and TEM study of voids in Si created by He implantation and annealing, Simpson *et al.*[12] reported that the measured *S* for positrons trapped in voids is approximately unity, i.e., close to that for undefected Si. The *S* parameter for V_n increases with *n* until saturation occurs at *n*~20 [13] but, as the cluster size grows further, the positron is no longer quantum mechanically localized but instead sees the void boundary as a clean, internal Si surface, whose characteristic *S* parameter is only slightly higher than that for bulk Si.

This model of void formation is supported further by the data after annealing at 800ºC. At this stage the data are consistent with 100% void formation (i.e., *S* ~1) with *L* = 40 nm. In order to check that the data were not obscuring a real (*S*>1) vacancy response, the native surface oxide was etched away with hydrofluoric acid; in the resultant data (Figure 5.1.8) the same *S* ~1 response is seen in the top Si layer.

In order to estimate the average size of the voids formed after annealing at 800ºC, the trapping was treated using the diffusion-limited trapping model, which is applied when the defects are large and widely separated. The positron trapping rate is then governed by the probability that a diffusing positron will encounter a defect site; once this occurs, then the positron is trapped. If the defects are homogeneously distributed and spherical then the positron trapping rate, κ, is given by, [13]

$$\kappa = 4\pi D_+ RN \quad (1)$$

where D_+ is the positron diffusion constant [=2.7 cm^2 s^{-1} in perfect Si [14]], R is the radius of the trapping site, and N is the defect concentration. κ is first obtained from knowledge of L in the Si layer (40 nm) and the maximum possible value of L (= L_+ = 250 nm) in undefected Si:

$$\kappa = \lambda[(L_+/L)^2 - 1] \quad (2)$$

where λ is the positron decay rate in undefected Si [= 4.54 x 10^9 s^{-1} [14]]. This gives κ = 1.7 x 10^{11} s^{-1} from Eq. (2) and thus, using Eq. (1), $RN \approx$ 5 x 10^9 cm^{-2}.

Assuming that all 3 x 10^{18} cm^{-3} V_3 clusters observed after annealing the sample at 600ºC agglomerate to form voids. The number of vacancies per void, n, is therefore

$$n = \frac{9x10^{18}}{N} = 180R \ (R \text{ in nm}) \quad (3)$$

Now, if one assumes that each vacancy occupies a volume, v_1, equal to that occupied by an atom of Si, v_1 = 0.02 nm^3, then a void of radius R containing n vacancies has a volume of $4\pi R^3/3 = nv_1 = (180R)(0.02)$ nm^3 which, when solving for R, gives $R \approx 0.93$ nm. This model thus implies the existence of voids of ~1.8 nm diameter containing, on average, 170 vacancies at a concentration of ~5 x 10^{16} cm^{-3}.

5.1-V Conclusions – Vacancies in SOIs

When the SOI samples were implanted with Si ions they caused damage in the form of vacancies and interstitials. This damage was situated in the Si and silica layers. The interstitials are not free to move in the silica as they would be in the Si layer. It was thought that because of this, during annealing there would be fewer interstitials able to diffuse to the Si layer to recombine with vacancies because they would 'stick' in the silica layer. As a result of this, damage could survive longer in the Si layer of the SOI samples compared to the Si samples, as seen in the data where damage survive to 700 ºC in Si and 800 ºC in SOI.

5.2 Vacancy-type defects created by single-shot and chain ion implantation of silicon

5.2-I Introduction

Vacancy engineering is an established method in front-end device processing, used for example to limit dopant diffusion, getter impurities and separate wafers[15 3 4]. A common way of introducing or 'implanting' vacancy-type defects is by ion implantation[2] in which ions of predetermined energy are implanted into a semiconductor target and create vacancies and interstitials (Frenkel pairs) along their path as they slow down. MeV silicon ions in silicon have a relatively narrow depth profile centred a few μm beneath the surface with a width of a few hundreds of nm; the vacancies (and recoil interstitials) they produce have a somewhat broader but nevertheless peaked depth profile, centred 100–200 nm below the ion range with a tail extending to the surface. The ion and vacancy profiles at the moment of implantation (i.e. before any post-implant diffusion or recombination) can be simulated using the standard code SRIM[11].

Monovacancies and Si interstitials are mobile below room temperature; it is therefore often assumed that the 5–10% of vacancies that survive room-temperature implantation are predominantly those which have encountered another vacancy to form divacancies, which are immobile at room temperature, rather than migrated to sinks or recombined with mobile interstitials. This rather simplistic model is complicated in the case of wafers doped with impurities (in which vacancy–dopant complexes may form) and in samples which have received a relatively large implantation dose in which complex defect structures may form prior to the eventual amorphization of the silicon substrate.

In order to investigate the dependence of vacancy survival on the depth profile of vacancy and interstitial defects, silicon has been implanted with either 4 MeV Si^+ ions or Si^+ ions of five different energies, each with one-fifth of the dose of the single implant, so that in the latter case the interstitial and vacancy depth profiles extend more uniformly from the surface to the maximum ion range, and the surviving vacancy-type defects studied in the as-implanted samples and after annealing at a range of temperatures. The co-implant will henceforth be referred to as a 'chain implant' and the single mono-energetic implant as a 'single-shot'.

5.2-II Experimental Procedure

Low-doped (p-type, $<10^{15}$ cm^{-3} boron) Czochralski-grown single-crystal Si was implanted with 4 MeV Si^{+} ions at the University of Surrey Ion Beam Centre at doses of 10^{12} and 10^{13} cm^{-2}. Chain implants were performed with Si^{+} ions of energies 0.4, 0.9, 1.5, 2.2 and 4 MeV, each with one-fifth of the dose of the single-shot implant so that the total numbers of implanted ions were the same in both cases.

Positrons of energies E, with an energy spread of ~1.5 eV, are implanted into the samples for E = 0.5–30 keV (in 0.5 keV steps up to 5 keV, 1 keV steps to 10 keV and 2 keV steps up to 30 keV). Ex-situ annealing was carried out on all samples at 50ºC intervals between 100 and 500ºC, and at 600ºC, and $S(E)$ measured at room temperature after each annealing - 40 sets of measurements in all. On occasion S was not measured at every value of E as this was not necessary to observe the essential features of the $S(E)$ curves.

5.2-III Results and Discussion

Fig. 5.2.1 shows simulations using the standard code SRIM[11] for the single-shot implant at 10^{13} cm^{-2} and the associated chain implants.

In both cases an estimate of the absolute divacancy distributions for each implant has been arrived at by (a) assuming that the final and initial vacancy depth profiles are similar, the latter being given by SRIM, and (b) by fixing the concentrations at half ion range to be those given by the formula developed by Coleman et al[18], which accounts for post-implantation defect recombination. Assumption (a) was shown to be reasonable by high-resolution VEPAS vacancy depth profiling measurements[19]. A similar procedure was followed to simulate the vacancy damage created by the lower-dose implants, and the result was so similar in depth dependence to Fig. 5.2.1 that it is not shown here. Procedure (b) was checked and shown to be consistent with the measured S parameters, via a calculation of the trapped positron fraction and using 1.035 for the S value of the divacancy; this value was directly measured using the current apparatus for a Si sample implanted with 2 MeV Si ions at a dose of 10^{14} cm^{-2}, which contains enough divacancies to trap all incident positrons.[18]

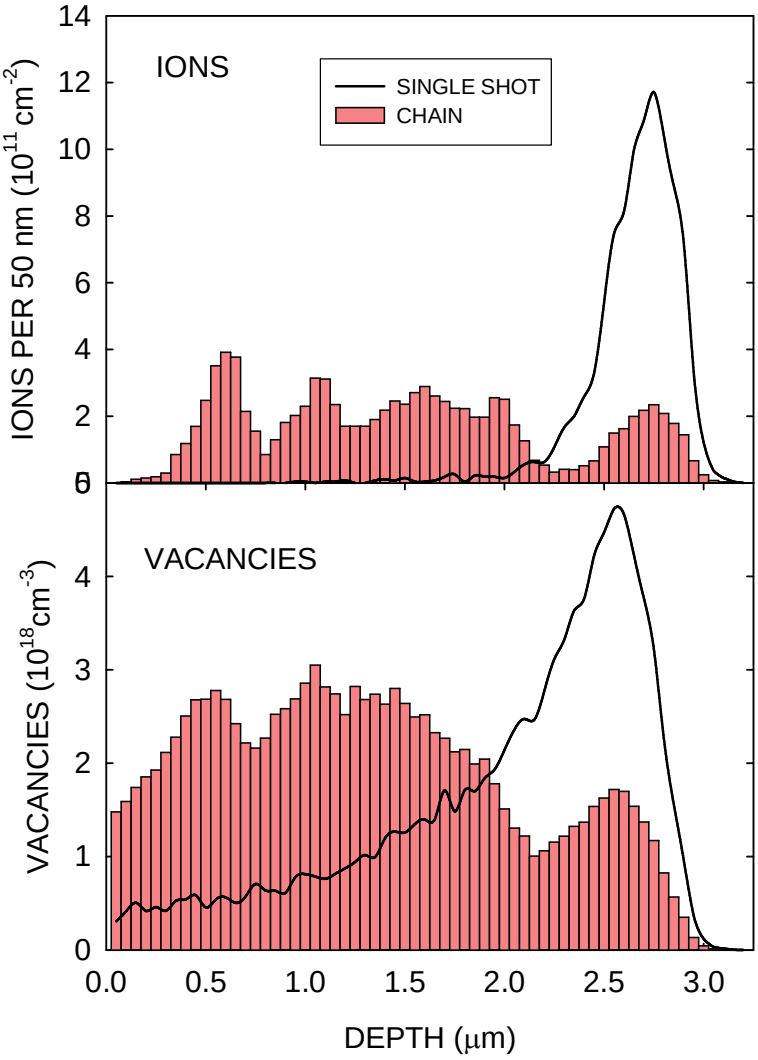

Figure 5.2.1: Depth profiles of implanted Si^+ ions (dose 10^{13} cm^{-2}) and divacancies remaining at room temperature, simulated by SRIM,[16] for both chain and single-shot implants. The divacancy distribution is assumed to be similar to the initial (time zero) monovacancy distribution, and the absolute concentrations are derived using the expression linking divacancy concentration at half-ion range with ion dose derived in Ref. 17. In the case of the chain implants this procedure was followed for each implant energy and the resulting distributions summed.

The recoil ion distribution is very similar to that of vacancies, and their total numbers are assumed to be equal. Therefore, the implanted ion distribution shown in Fig. 5.2.1 represents that of the excess interstitials, and their mean separation from divacancies is significantly greater than between the recoils and the divacancies. On the basis that vacancies are always

relatively close to recoil interstitials, and somewhat farther from the implanted Si ions, it is not clear whether the overall average separation between interstitials and vacancies is significantly different after chain and single-shot implants; hence this experimental study.
The results for $S(E)$ for samples implanted with a total of 10^{12} and 10^{13} ions cm^{-2} are shown in Fig. 5.2.2.

Three curves are shown for each sample; the data for annealing temperatures up to 350ºC were similar, and so are grouped, as are those for 400–500ºC; finally, the data after complete annealing at 600ºC are shown. These last data exhibit $S(E)$ characteristic of unimplanted Si, rising smoothly from the surface S to bulk S (unity).

Focusing on the results for the higher-dose samples in Fig. 5.2.2, one sees that $S(E)$ for the as-implanted sample and for annealing temperatures up to 350ºC shows a somewhat larger response to divacancies for the chain-implanted sample over a wider range of incident positron energies (and thus depths below the surface), becoming similar to the single-shot response only at $E \sim 20$ keV when the divacancy concentration for the single-shot-implanted sample becomes significant (see Fig. 5.2.1). Above 20 keV, S decreases towards the Si substrate value of 1 as a greater fraction of the increasingly broad positron implantation depth profile (width~mean depth) extends beyond the defected region.

The most significant difference between the positron response to the two samples in Fig. 5.2.2 can be seen in the raw data after annealing to temperatures between 400 and 500ºC. While $S(E)$ for the chain-implanted sample stays high (except at the lowest E, when the somewhat lower surviving divacancy concentration leads to enhanced positron diffusion to the surface, which has a lower characteristic S), the response for the single-shot sample is considerably lower for $E < 20$ keV. After annealing at 600ºC, essentially all of the VEPAS response to vacancy damage has been removed in all samples.

The data for the lower-dose samples show the same significant difference between chain- and single-shot-implanted samples at annealing temperatures below 350ºC; all of the measurable response is annealed away at higher temperatures.

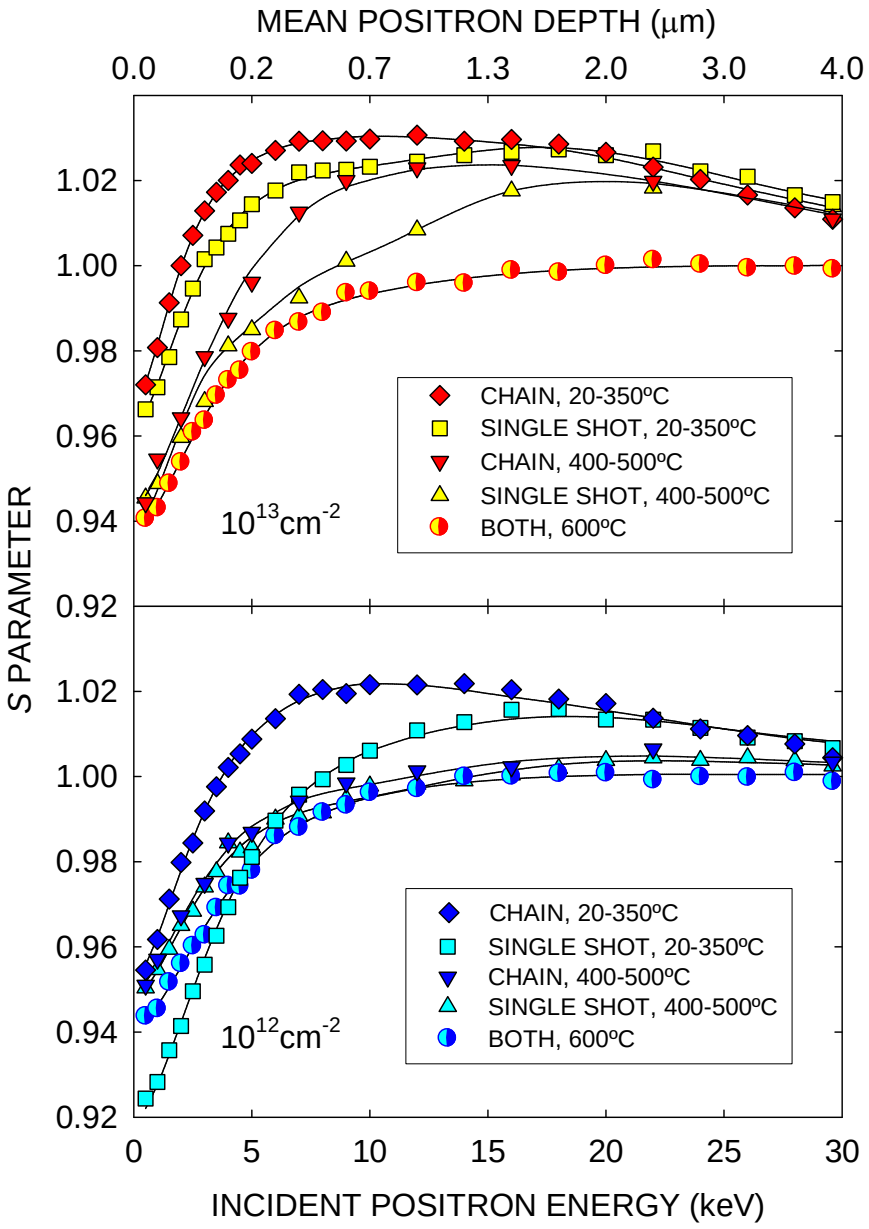

Figure 5.2.2: S(E) for high- and low-dose, chain and single-shot implants. The data shown represent those taken after annealing at temperatures between 20–350, 400–500 and 600ºC.

It is important to note that the ion doses used in this study were chosen so as not to produce vacancy concentrations high enough to trap all implanted positrons (i.e. to lead to saturation trapping), either before or after annealing, as this would severely complicate data interpretation.

The deduction that there is a higher surviving concentration of divacancies at depths below 2 μm in the chain-implanted sample before annealing - rather than, say, a tendency to form

small vacancy clusters with a higher characteristic *S* value - is supported by considering Fig. 5.2.1. The initial monovacancy concentrations in the 0–2 μm region are never more than ~50% of the peak, and are not high enough to trap all implanted positrons. Many years of VEPAS studies of Si have indicated that under these circumstances, monovacancies formed in these concentrations at the moment of implantation at room temperature either migrate to sinks, recombine with interstitials or form divacancies and become immobile, the last being only a few per cent of the initial number.

The data for the single-shot-implanted samples bear resemblance to those of Coleman et al[20] in which the persistence of VEPAS response at the vacancy peak was explained by the formation of small clusters V_n, with $n \sim 3$–4, with consequently lower mobility and higher annealing temperatures (divacancy annealing is reported to occur at 290–350ºC).[21] The significant reduction in the response at shallower depths corresponds to simple annealing of V_2. It was noted in Ref. [20] that vacancy evolution mechanisms depend to some extent on annealing methods and history, and some apparent differences between VEPAS and other techniques were discussed by the authors of that paper. For the chain-implanted samples it can therefore be postulated that the higher absolute divacancy concentrations at shallower depths (i.e. from the surface to ~2 μm) compared to the single-shot-implanted samples (Fig. 5.2.1) mean that on annealing at least some of the V_2 agglomerate to form small clusters which survive to higher temperatures.

Fits of the raw data using the standard code VEPFIT,[22] requiring self-consistency between fitted positron diffusion lengths and *S* parameters, support this model. The expressions linking defect concentrations with fitted *S* (or diffusion length) values were given in ref. 20. For example, fitting $S(E)$ for the higher-dose chain-implanted sample (top graph, Fig 5.2.2) yields a mean divacancy concentration of 3×10^{18} cm^{-3} in the first 1.5 μm below the surface in the as-implanted sample, in broad agreement with the estimated value shown in Fig 5.2.1, whereas after annealing at temperatures between 400 and 500ºC the fit is consistent with the formation of small vacancy clusters V_n (with $n \sim 4$) in the same depth range, with a mean concentration of 10^{17} cm^{-3}, implying that about 7% of the divacancies agglomerated into tetravacancies after annealing. In contrast, the mean divacancy concentration in the top 1.5μm of the higher-dose single-shot-implanted sample is ~8×10^{17} cm^{-3} (again consistent with Fig. 5.2.1), but after annealing at 400–500ºC no defect signature is detectable by VEPAS.

5.2-IV Conclusions - Single-Shot and Chain Ion Implantation

The results of this study imply that (a) monovacancies survive (in divacancies) more readily in chain-implanted samples than single-shot-implanted samples, and (b) there is a threshold concentration for divacancy clustering at 400–500ºC of between 1 and 2×10^{18} cm^{-3}. The key to these observations appears to lie in the lack of, or at best minimal, influence of interstitial silicon atoms, either from the implanted ions or from those recoiling during implantation. This may be explained by the relative lack of movement of any surviving interstitials at the temperatures employed in this study. VEPAS measurements have previously[23] shown that the migration energy for silicon interstitials was about five times smaller than for monovacancies (~0.1 eV), and therefore it is likely that at room temperature all interstitials have migrated to sinks, recombined with vacancies, or formed immobile clusters—playing no further significant role in the vacancy evolution seen here.

5.3 Positron annihilation studies of fluorine-vacancy complexes in Si and SiGe

5.3-I Introduction

The effect of fluorine on the behaviour of vacancies (V) and interstitials (I) in Si has been of great interest to researchers in the past[24] due to its effectiveness in reducing transient-enhanced diffusion of dopants such as boron. For example, limiting B diffusion would allow the formation of ultra-shallow junctions. This can be achieved via the formation of fluorine-vacancy (FV) and fluorine-interstitial (FI) complexes.[25]

Recently, strained SiGe layers have been a subject of interest as they have been shown to produce high electron mobility transistors, much higher than in relaxed materials.[26] Kögler *et al*. reported on the behaviour of V and I in SiGe, showing that ion-induced damage in SiGe is higher than in Si and increases with increasing Ge content.[27] It was found that in SiGe the Ge content impedes vacancy-interstitial defect recombination. However, not much is known about the effect of F on the behaviour of V and I in SiGe. Positron annihilation spectroscopy (PAS) has been used to investigate vacancy-dopants complexes in SiGe,[28] which concluded that the presence of Ge around a vacancy is not enough to make divacancy defects stable at

room temperature. In a previous report,[29] the effect of F in a layered HBT-type structure of Si-SiGe-Si was investigated using VEPAS with the main result showing that $F_{4n}V_n$ complexes are associated with the SiGe layer and that they preferentially accumulate at the Si/SiGe interfaces. Here this work is extended and VEPAS is used to investigate the effect of F in multiple strained Si-SiGe layers and relaxed SiGe.

5.3-II Experiment and Analysis

Relaxed SiGe layers, 1µm thick, having Ge fractions of 10, 20 or 30% were deposited by reduced pressure chemical vapour deposition onto a graded SiGe layer with linearly decreasing Ge% (10% per µm) on a p-type Si (100) substrate. Compressively strained Si-SiGe-Si multi-layers with Ge fractions of 10% (50 nm), 20% (30 nm) and 30% (10 nm) with ~100 nm of Si in between each layer. The different layer widths shown in brackets were used to retain strain in the SiGe. F ions were implanted into the samples at room temperature with an energy of 185 keV at a fluence of 2.3×10^{15} cm^{-2}. The samples were rapid thermal annealed in a N atmosphere for 20 s at 800ºC.

The ratio curve technique used throughout this work measures – also with a single Ge detector - the annihilation line, or spectrum, peaked at 511 keV with high precision to extract further information from the higher momentum components contained in its wings. A more detailed description of this technique can be found in Chapter 3.5. By fitting combinations of pure states, each with its own unique signature, a more detailed picture of the vacancy complexes in the region of interest can be found.

Initial F implantation and Si and Ge defect profiles were simulated with the program SRIM (Stopping and Range of Ions in Matter).[30] A concentration depth profile of F after annealing was measured using secondary ion mass spectrometry (SIMS).

5.3-III Results and Discussion

A. Positron affinity for Si and Ge

To investigate the chemical composition of the defect environment created by ion implantation and annealing the relative positron affinity for Ge and Si first needed to be

known. The unimplanted samples were etched in hydrofluoric acid to remove any surface oxide response and spectra were taken at a single energy where the mean implantation depth of the positrons was within the first micron. The spectra were normalised to Si. It was found that after removing a percentage of a Ge/Si peak equal to the Ge content of each sample the ratios are ~1 over all energies, meaning that only a response to Si remained - as seen in Fig. 5.3.1.

This result indicates that there is essentially the same relative positron affinity for both Si and Ge and that this technique can be used to obtain quantitative information, as discussed in ref. 31.

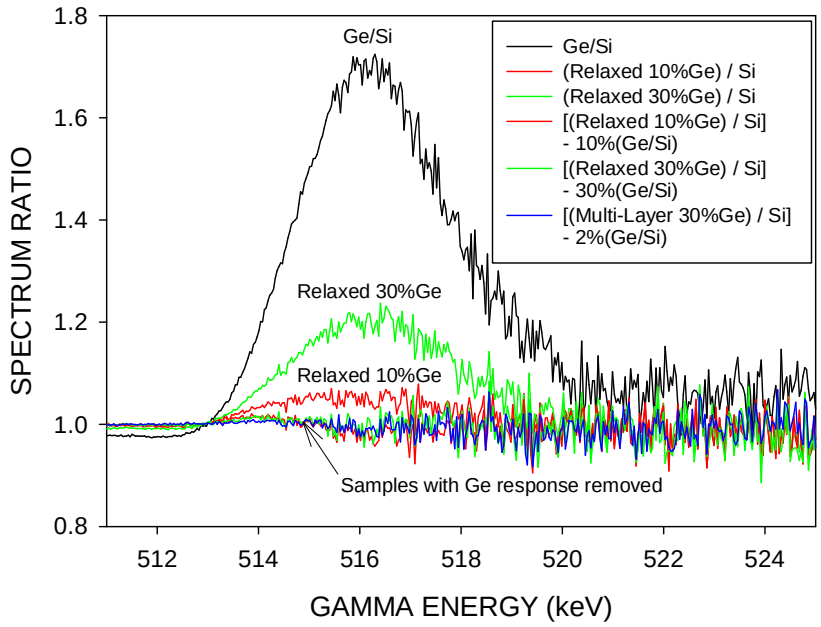

Figure 5.3.1: Ratios of the unimplanted samples of relaxed 10 and 30%Ge and multi-layer 30%Ge, before and after removal of Ge ratio response. (Multi-layer 30%Ge is not shown before Ge removal for clarity). The ratio for Ge/Si is shown for reference. All spectra are divided by a Si spectrum.

B. As-Implanted Samples

After implantation the *S*(*E*) results (Fig. 5.3.2, only 10 and 30%Ge samples shown for clarity) for the relaxed SiGe samples show that as the percentage of Ge increases the average *S* parameter in the saturated region (3-10 keV) decreases slightly. This was as expected because Ge has a lower *S* parameter than Si. However, the multi-layer samples (again only 10 and

30%Ge samples shown for clarity) show that as the percentage of Ge increases, the average *S* parameter in the saturated region (3-10 keV) increases slightly. It is believed this is due to the width of the Ge layers, where the 30%Ge sample had the narrowest SiGe layers and the widest Si layers and therefore would have the lowest response to Ge.

All the fits to the data for the as-implanted samples, obtained using VEPFIT, were similar, with only slight variations in the V-rich defected region *S* parameter, as suggested by the raw data in Fig. 5.3.2.

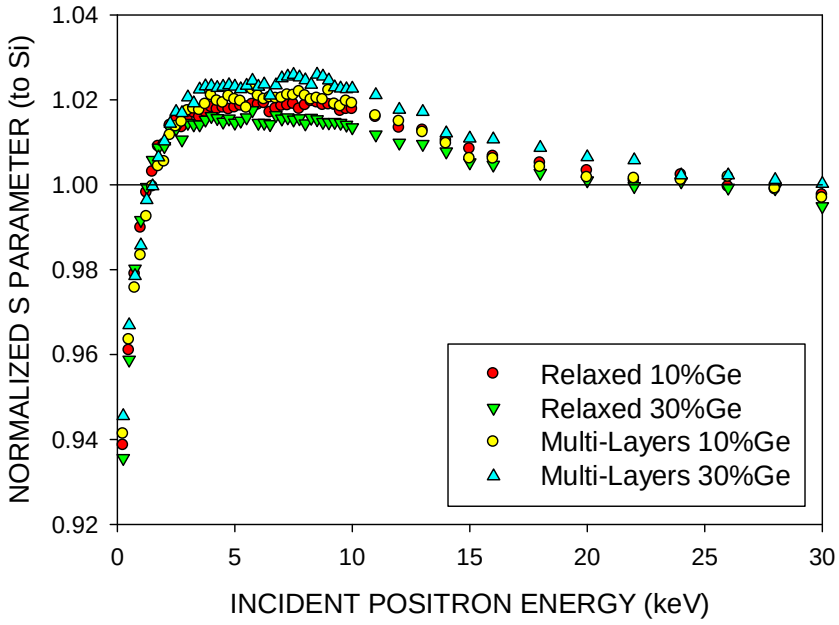

Figure 5.3.2: Normalized S(E) plot for as-implanted relaxed and multi-layer samples of 10 and 30%Ge.

The saturated region has a normalised *S* parameter below that for both di-vacancies in Si (*S* ~ 1.04) and amorphous Si (A-Si) (*S* ~ 1.03). An *S* parameter of ~ 1.04 has been shown to be the characteristic *S* of an isolated di-vacancy in Ge (normalised to bulk Ge), which is reduced to ~1.02 if normalised to bulk Si (previous measurements of the ratio of bulk Ge to bulk Si *S* parameters have been ~ 0.98).[32] It is extremely unlikely that there is just this single type of defect when the largest proportion of the sample is Si; therefore, a mixture of defect types are instead contributing to the *S* parameter.

To determine what these defect types could be, combinations of likely elements and states were compared to the measured spectral ratio data in order to gain a best fit. In this case amorphous Ge (A-Ge), Ge, Si, V_2 in Si and A-Si were considered. Examples can be seen in Fig. 5.3.3.

Data for the relaxed 10%Ge, relaxed 30%Ge and 30%Ge multi-layer samples at 6 keV had best fits of [15%Ge + 85%A-Si], [30%Ge + 70%A-Si] and [5%Ge + 95%A-Si], respectively. The uncertainties in these percentages can be up to ±5%, as fits are assessed by eye. The use of spectra ratio data for A-Si does not necessarily imply that the Si was amorphized by the

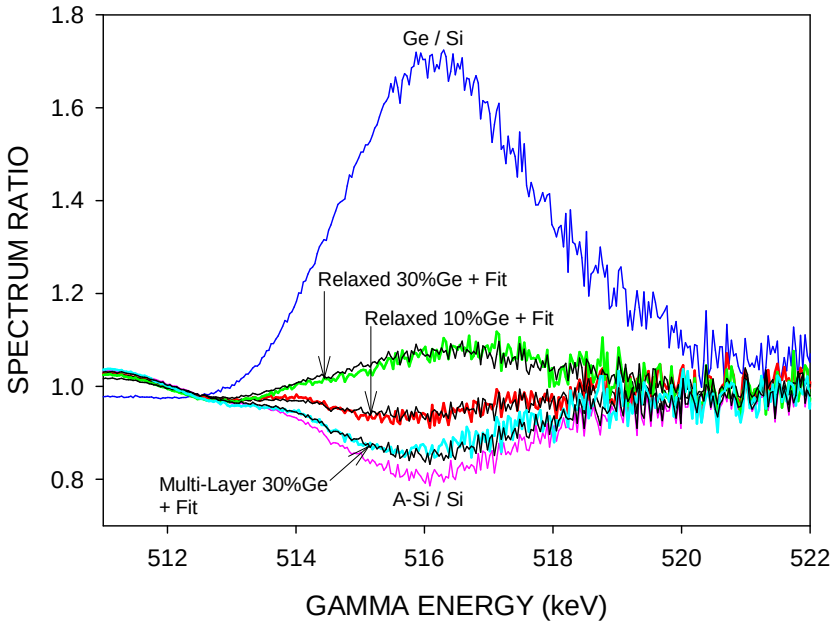

Figure 5.3.3: Ratios of the as-implanted samples of relaxed 10 and 30%Ge and multi-layer 30%Ge at 6 keV. Best fits are shown on top of data. Ratios of Ge/Si and A-Si are shown for reference. All spectra are divided by a Si spectrum.

implant, but rather that the Si structure was disordered – possibly containing V_n for which spectral data was not available. The positron sensitivity to Ge seems to remain unchanged and still looks like a Ge response rather than A-Ge. These fits imply an even distribution of vacancy defects within the material and are consistent with the $S(E)$ data, which can be reproduced using the fitted percentages and the characteristic S values for Ge and A-Si. The fits to the spectra for multi-layer samples have much lower Ge percentages because of the smaller overlap in the positron implantation profile with the thin SiGe layers.

C. Annealed Samples

After annealing the remaining damage can be seen as peaks (vacancy-rich defects) and dips (FV complexes),[25] at 3 and 6 keV, respectively, in the example *S*(*E*) data in Fig. 5.3.4.

This pattern can be seen in all samples, although there are slightly different apparent depths corresponding to the peaks and dips due to differences in sample density affecting the positron implantation profile. There appears to be little correlation between the peak/dip *S* parameters and the Ge content in all samples, so ratio curves were taken at each peak and dip

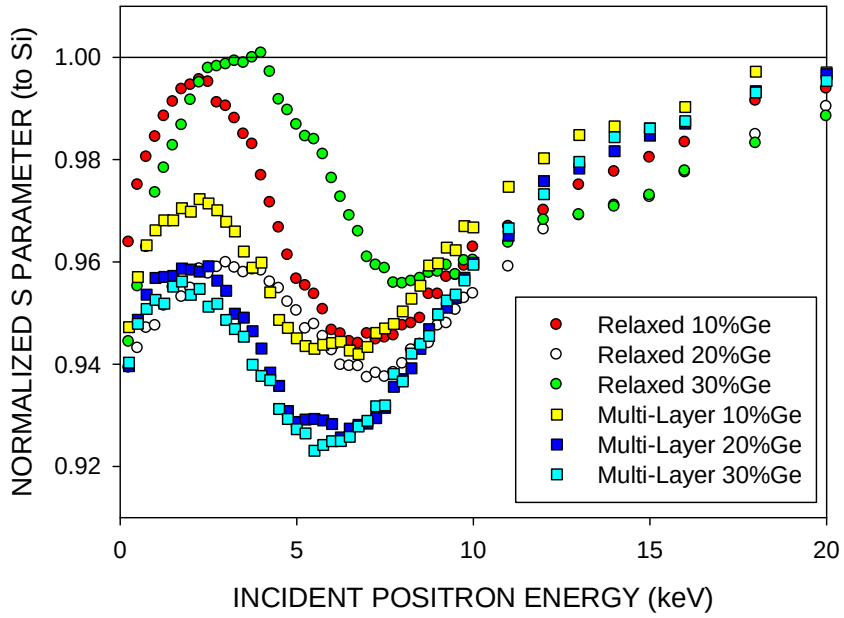

Figure 5.3.4: Normalized S(E) plot for annealed relaxed and multi-layer samples of 10-30%Ge.

to try to determine the nature of the defects and the reasons for the differences between samples. It is important to recognise that since ratio curves are taken at one implantation energy their response will be due to annihilations over the whole of the implantation profile, not just at the depth of interest, so the following fits can only give an idea of the defects' chemical composition.

Reference spectra for Ge, F, V_2 in Si, Si and implanted SiO_2 (for an O response) were used to fit the lower energy peaks seen in Fig. 5.3.5.

The relaxed samples had good fits with a large % of F and V_2 with the remaining contributions being from free positron annihilation in Ge and Si in their original ratios. For example, the 10%Ge sample could be fit well with [5%Ge + 45%Si + 23%F + 27%V_2] and the 30%Ge sample with [20%Ge + 40%Si + 10%F + 30%V_2]. The heights of the peaks in $S(E)$ seem to depend on the F content – i.e., there are FV complexes as well as divacancy defects in this region. The multi-layer samples, however, could not be fit well with the expected F, Si and V_2 curves; instead fits were found containing F, Si and O. For example the spectrum for the 30%Ge sample was fit well with [10%F + 64%Si + 26%O] (there is no Ge response since the first SiGe layer is deeper than the low-energy peak). The multi-layer

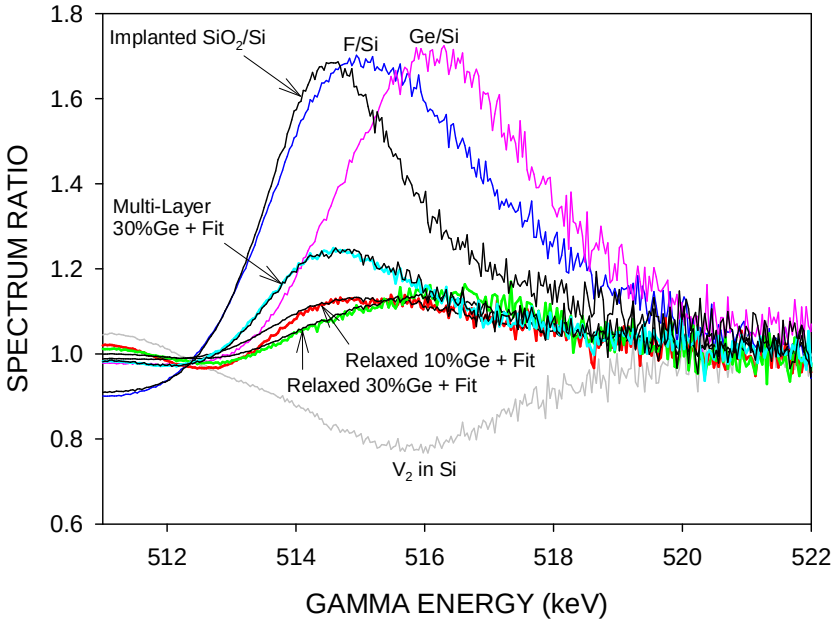

Figure 5.3.5: Ratios of the annealed samples of relaxed 10 and 30%Ge and multi-layer 30%Ge at ~2 keV. Best fits are shown on top of data. Ratios of implanted SiO_2/Si, F/Si, Ge/Si and V_2 in Si/Si are shown for reference. All spectra are divided by a Si spectrum.

samples appear to have an O response in this damaged region whereas the relaxed samples did not. The SIMS analysis did not include oxygen. The spectra ratios for the higher-energy dips seen in Fig. 5.3.6 were fit with Ge, F, and Si.

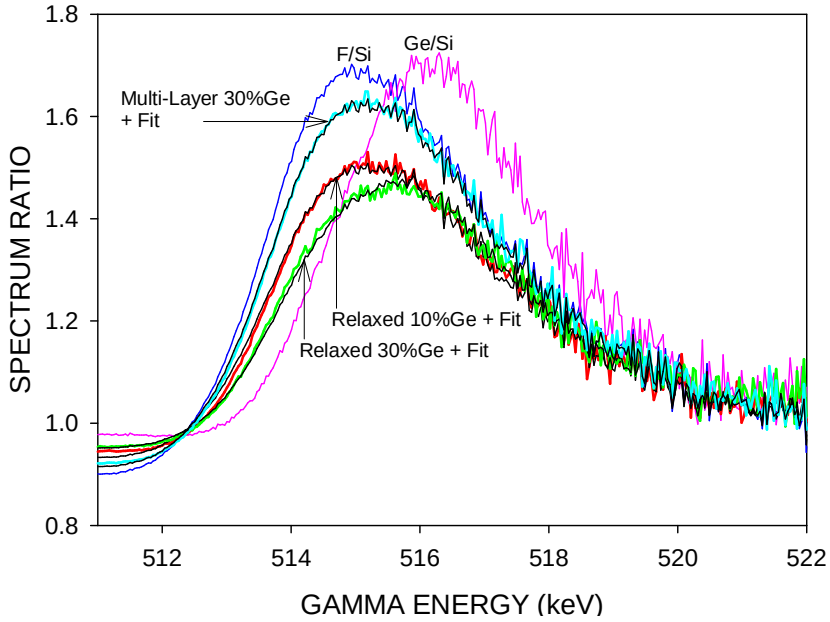

Figure 5.3.6: Ratios of the annealed samples of relaxed 10 and 30%Ge and multi-layer 30%Ge at ~7 keV. Ratios of implanted F/Si and Ge/Si are shown for reference. All spectra are divided by a Si spectrum.

This region is thought to be mainly populated by FV complexes. These spectra were successfully fit in both the relaxed and the multi-layer samples. Relaxed 10%Ge, for example, was fit by [10%Ge + 65%F + 25%Si] and 30%Ge by [30%Ge + 42%F + 28%Si]. These fits do not follow the same pattern as those for the lower-energy vacancy-rich peaks in that the Ge/Si ratio has changed. The fitted Ge% matches that of the as-grown samples, suggesting that, in this case, the F could be preferentially combining with vacancies in Si, since the positron response to Ge remains the same while some of the response to Si is replaced by F. The multi-layer samples were fit in the same way - e.g., 30%Ge had [10%Ge + 84%F + 6%Si]. All three multi-layer samples had this 10%Ge response with only the F content varying and changing the *S* parameter.

D. Comparison with SRIM and SIMS Results

The positron data can be further interpreted using information gained from SIMS. Fig. 5.3.7a and 5.3.7b show examples of VEPAS (with VEPFIT fits), SRIM and SIMS results plotted together.

The VEPAS depths are mean positron implantation depths, and at each depth the FWHM of the positron depth profile is approximately equal to the mean depth. Therefore, the response

becomes progressively more smeared as the depth increases. However, the fitting code VEPFIT takes this into account.

The following summarises the main elements of Fig. 5.3.7a and 5.3.7b, which are common to both relaxed and multi-layer samples.

VEPAS data (left-hand axis) are fit by VEPFIT into 3 distinct regions: the topmost region having a short positron diffusion length but high *S* parameter, suggesting a vacancy-rich region, most probably a mixture of undecorated vacancies and FV complexes. The second region has a short positron diffusion length and low *S*, suggesting a FV-rich region. The third region is the Si substrate.

SRIM simulations show the initial F implantation profile and the resulting Si and Ge vacancy profiles before annealing. SIMS intensity plots (right-hand axes) are shown for F after annealing. The double F-peak feature seen in the relaxed samples had similar profiles, an example of one can be seen in Fig. 5.3.7a. Originally a 9-region model was used in VEPFIT for the strained multi-layer samples, on the assumption that all the FV complexes were confined to the SiGe layers (as suggested by the SIMS F peaks). The model assumed zero diffusion in the SiGe layers – i.e., saturated positron trapping because of the high concentration of FV in these layers. However, the fitted *S* parameter for these layers was considerably higher (i.e., > 0.91) than that expected for 100% trapping in F complexes[33]. Also, the third SiGe layer from the surface always had the greatest SIMS F concentration but there was no response to it in any of the *S*(*E*) plots, as is demonstrated by the example data in Fig. 5.3.7b. An alternative VEPFIT model was therefore required in which the vacancies created by the implanted F form complexes with F in a similar region in each sample. The dip in the *S* parameter caused by the F is always seen in the middle of this region; this depth is that of the peak of Ge and Si vacancies caused by the initial F implantation damage as calculated by SRIM. The F SIMS for each of the multi-layer samples had very similar profiles, an example of one can be seen in Fig. 5.3.7b. In the first SiGe layer at ~150 nm there was almost no pile-up of F, the average concentration was similar to that in the surrounding Si. The second SiGe layer at ~300 nm always laid close to the center of the dip in the *S*(*E*) plots. The concentration of F in this layer was significantly higher than in the first and similar to that seen in the relaxed samples at the same depth (see Fig. 5.3.7a). Extra disorder in the SiGe layer may be trapping and localizing F but it is the initial implantation damage causing

the formation of FV complexes. The third SiGe layer at ~500 nm contained the greatest concentration of F, this layer becomes saturated with F atoms leaving few open volume defects effectively becoming invisible to VEPAS thereby showing a similar depth response to that in the relaxed SiGe samples.

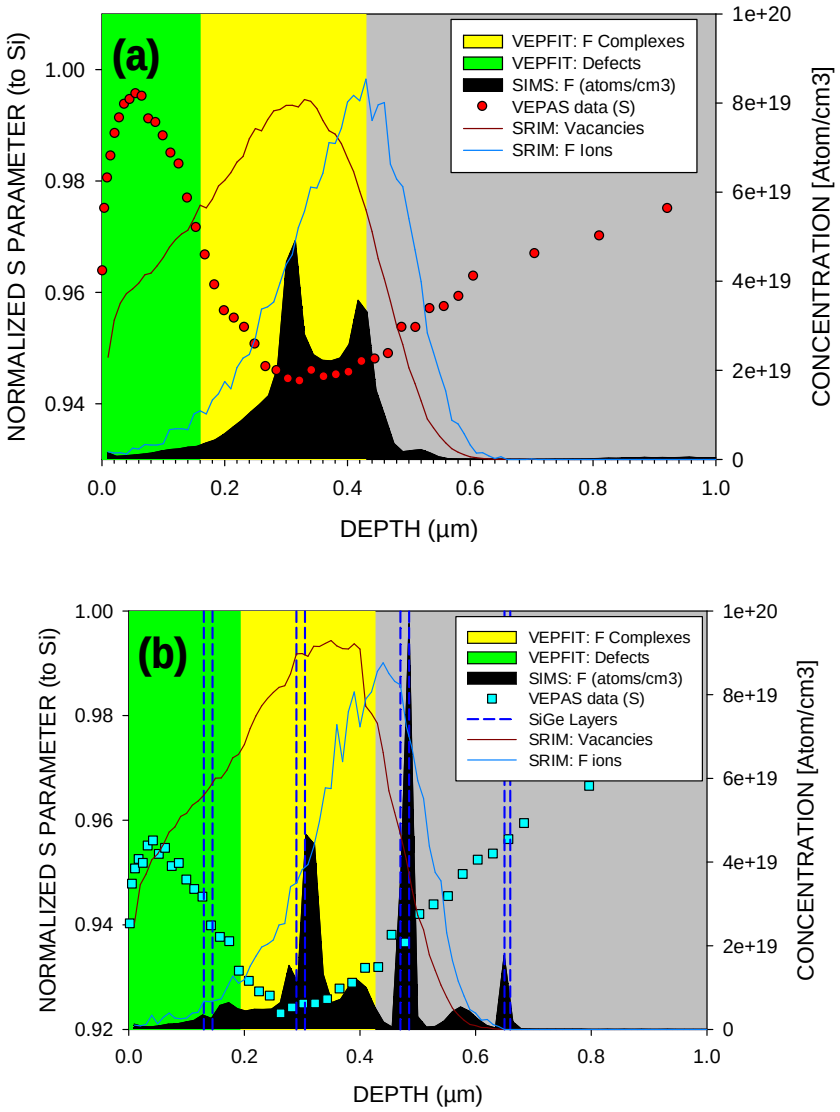

Figure 5.3.7: All depth dependent data is shown for the annealed relaxed sample of 10% Ge (a) and the multi-layer sample of 30% Ge (b). The left-hand axis corresponds to the normalized S(E) plot and the right-hand axis corresponds to the SIMS F concentration data. Other plots include the two VEPFIT regions of F complexes and vacancy-rich defects and the initial Si and Ge vacancy and F ion profiles.

A 3-region VEPFIT model was thus used for both the strained multi-layer and relaxed samples, fitting a region of vacancy defects ~200 nm wide followed by a ~240 nm wide FV complex region and bulk Si for all samples.

Using SIMS and VEPFIT data the 3-region model was further analysed to obtain average concentrations of V_2 (C_{V2}) and FV (C_{FV}) in the top region, and the ratio of F to V in the second region. To analyse the top region (~0-200 nm) the average concentration of F (C_F) was found from SIMS data in the same region. The average C_{FV} and C_{V2} were found using the ratio curve fits, from the fraction trapped in F and V_2, respectively. These can be used for the top region as the implantation profile lies completely within it. Both concentrations were derived using

$$C = 5x10^{22}[f\lambda_B/\nu(1-f)]\ \mathrm{cm}^{-3} \quad (1)$$

since there are multiple types of trapping defect, where *f* is the trapped fraction found from the ratio curves, λ_B is the positron annihilation rate in perfect Si (4.54 x 10^9 s^{-1}),[34] and ν is the specific trapping rate for positrons in a trapping defect which was assumed to be 10^{15} s^{-1} for the FV complexes and 7 x 10^{14} s^{-1} for divacancies. If the FV complexes were $F_{4n}V_n$ (where n is most likely to be 1 or 2) then for example in the relaxed 10%Ge sample 15-30% of the total F, according to SIMS, is in complexes, with the rest left as isolated F, agglomerates or precipitates, as seen before.[29] A summary of results for the relaxed samples' top region can be seen in Table 5.3.I.

Sample (Relaxed)	C_F from SIMS (10^{18} cm^{-3})	C_{FV} (10^{16} cm^{-3})	C_{V2} (10^{17} cm^{-3})	%F in $F_{4n}V_n$ n = 1/2
10%Ge	1.7	7	1	15/30 %
20%Ge	5.3	16	0.8	12/24 %
30%Ge	6.3	2.5	1.4	2/4 %

Table 5.3.I. Concentrations of F, FV and V_2 in the top region of relaxed samples

There appears to be little correlation between the Ge content and vacancy concentration. The low percentage of F in complexes in the relaxed 30%Ge sample is due to the low C_{FV} in the sample derived from the high *S* parameter.

The top region for the multi-layer samples was analysed in the same way but only C_{FV} was deduced as any V_2 response was masked by the O response. The concentration of oxygen complexes (C_O) was calculated assuming the trapping rate was the same as that used for FV complexes. The results are shown in Table 5.3.II.

Sample (Multi-Layer)	C_F from SIMS (10^{18} cm^{-3})	C_{FV} (10^{16} cm^{-3})	C_O (10^{16} cm^{-3})	%F in $F_{4n}V_n$ n = 1/2
10%Ge	2.1	7	4	13/26 %
20%Ge	2.4	2.5	8	4/8 %
30%Ge	2.7	2.5	8	4/8 %

Table 5.3.II. Concentrations of F, FV, and O in the top region of multi-layer samples

F is possibly being displaced by the presence of more oxygen in the 20 and 30% multi-layer samples causing fewer F to complex with vacancies.

The ratio curve fits cannot be used to find C_{FV} in the second region since the fraction trapped is in the region of the implantation profile, not just the second region. They can however be used to find S for FV complexes (S_D). Knowing the S parameter for Ge (0.98) and Si (1) and finding the total S from the $S(E)$ data at the energy measured the S parameter for the FV complexes in all samples was found to be 0.91 ± 0.01.

Analysing the second region in the relaxed samples again required the C_F for the region (~ 200-440 nm) to be found from SIMS. The C_F in the multi-layer samples also includes the whole region, including the peak, as the two contributions cannot be distinguished is the present samples. To do so would require samples with SiGe layers outside the region of ion damage. The C_{FV} was derived using the S parameter fitted for the region, rather than using the ratio fits as the implantation profile now extends beyond the limits for the region and there is only one type of trapping defect thought to be in this region. Using

$$C_D = 5\,x\,10^{22}[\lambda_B(S - S_B)/\nu(S_D - S)]\ \text{cm}^{-3} \qquad (2)$$

where ν is the specific trapping rate for positrons in a FV defect which again was assumed to be 10^{15} s^{-1}, S_B is the bulk S parameter (~1) and S_D is assumed to be 0.91. To find the S parameter for the second region VEPFIT was used to fit the S with the constraint that it was

Sample	C_F from SIMS (10^{19} cm^{-3})	C_{FV} (10^{18} cm^{-3})	F:FV
10%Ge (Relaxed)	1.8	7	3:1
20%Ge (Relaxed)	3.0	5	6:1
30%Ge (Relaxed)	1.3	2	7:1
10%Ge (Multi-Layer)	1.0	6.5	2:1
20%Ge (Multi-Layer)	1.1	41	1:4
30%Ge (Multi-Layer)	1.3	41	1:3

Table 5.3.III. Concentrations of F and FV in the second region of all samples

consistent with the positron diffusion length L fitted for the same region. A summary of results for the second region of each sample is given in Table 5.3.III.

The ratios of F per FV complex for the relaxed samples and the 10%Ge multi-layer sample are consistent with $F_{4n}V_n$ (where n=1 and/or2). The 20 and 30% multi-layer samples, however, have unrealistic ratios. It is believed this is caused by the increased uncertainty in the fitted S_D with high concentrations of $C_{FV} - L$ can vary significantly with small changes in S when close to saturation.

5.3-IV Conclusions - Fluorine-Vacancy Complexes in Si and SiGe

The positron results presented here suggest that for all samples, both relaxed and multi-layer, there exist two regions defined by the depth profile of the implanted F ions. The first, shallower region (from the surface to ~200 nm) contains a mixture of undecorated vacancies (possibly V_2) and FV complexes; there is no correlation between the vacancy or F concentrations in this region and the %Ge. The multi-layer samples may have an O contamination that is not present in the relaxed samples. The second region (from ~200-440 nm) contains primarily FV complexes. Interestingly, the positrons appear to be relatively insensitive to the highest concentrations of F in the third SiGe layers – ie, the FV complexes do not reside primarily in this layer, but instead are distributed over depths similar to those in the relaxed samples as it is the initial damage caused by the F implant that facilitates the formation of FV rather than the SiGe layers as previously thought. The F:FV ratios are approximately 3-7:1 in the relaxed samples, and 2:1 in the 10%Ge multi-layer sample, consistent with $F_{4n}V_n$ (where n=1 and/or 2) as has been seen before. However, ratios cannot

be calculated with precision for the 20 and 30%Ge multi-layer samples due to large uncertainties in C_{FV} close to saturation.

5.4 Direct observation of electron capture and re-emission by the silicon divacancy via charge transient positron spectroscopy

5.4-I Introduction

The emission and capture of charge carriers in silicon is well-described by Shockley-Reed statistics,[35] whereas Simmons and Taylor expanded these ideas to a system of arbitrary traps in a semiconductor subjected to non-equilibrium conditions.[36] ENREF 41 For a single trap there are four possible transitions, electron capture, electron emission, hole capture and hole emission described respectively by the rates $\upsilon\sigma_n n N_t(1-\alpha)$, $e_n N_t \alpha$, $\upsilon\sigma_p p N_t \alpha$ and $e_p N_t(1-\alpha)$. Here n is the electron density, p the hole density, N_t the defect concentration, α is the probability of defect occupation by an electron, υ is the electron thermal velocity, σ_n is the capture cross-section for electrons at the defect and σ_p is the capture cross-section for holes; e_n and e_p are the probabilities for the emission of electrons and holes respectively. It can be shown that the fraction of occupied defect sites is given by[36] ENREF 41 ENREF 41

$$\alpha = \frac{\bar{n} + e_p}{e_n + \bar{n} + \bar{p} + e_p} \qquad (1)$$

where $\bar{n} = \upsilon\sigma_n n$ and $\bar{p} = \upsilon\sigma_p p$.

In a p-n diode under forward bias, minority carriers are injected across the junction. If the device contains defects in the region of the junction, occupancy for minority carrier trapping defect sites will be non-zero. The direct measurement of the occupancy fraction for these defects is non-trivial. However, the measurement of the emission rate from the filled defects does not normally depend on the occupancy fraction and thus the filling of minority trapping defects using a forward bias pulse, and their subsequent emptying via the removal of that forward bias, allows information on the nature of the trap to be obtained via transient charge measurement. The neutral silicon divacancy has an associated energy level which resides in the upper half of the bandgap and thus divacancies on the p-side of a p-n junction may be considered minority trapping defects.

There exists a number of studies of the silicon divacancy using transient charge measurement, most often Deep-Level-Transient-Spectroscopy (DLTS).[37] A selection of these studies provides values for σ_n which can vary from 10^{-15} to $3x10^{-15}cm^{-2}$ (e.g., Refs. [38], [39]) and an energy level of ~E_c - 0.4eV [e.g., Ref. [40]]. In a study primarily aimed at understanding the annealing behavior of V_2 in silicon and V_2O formation Markevich et al.[41] measured emission rates at low temperatures for the singly and doubly negatively-charged V_2 (i.e., -/0 and --/-), again using DLTS and LDLTS, for electron-irradiated silicon, the two trap levels being 0.41 and 0.23eV below the conduction band, respectively. Using their results and extrapolating to room temperature yields mean state lifetimes of 33 μs and 13 ns, respectively.

Because positrons are efficiently trapped by divacancies in silicon, and their trapping rate depends on the charge state of the defect,[42, 43] VEPAS is a strong candidate for probing changes in the V_2 charge state in the depletion region of Si diode structures under different bias conditions. Beling et al., recognizing this potential, proposed an approach they termed positron-DLTS, which involved the measurement of positron mobilities and lifetimes in metal-semiconductor structures.[44] Kauppinen et al.[45] used positron spectroscopy to observe the photo-ionization of V_2^- and V_2^{2-} at 15K and noted that the specific positron trapping rates ν for V_2, V_2^- and V_2^{2-} at 20K were in the ratio 1:35:70. Whereas ν for neutral vacancies is almost temperature-independent, those for negatively-charged vacancies fall considerably as temperature increases so that for example the calculated values of ν for V^0, V^- and V^{2-} at room temperature the ratio is approximately 1:6:15.[42] Mascher et al.[43] experimentally determined that this ratio at room temperature for V_2 is approximately 1:3.5:7, whereas in a later paper Kawasuso et al.[46] reported a ratio closer to 1:12:36.

5.4-II Experimental Procedure

The sample used in the present study is shown in Fig. 5.4.1.

The diode structure was formed by a phosphorus-doped (>$10^{19}cm^{-3}$ peak concentration) Si region 5mm in diameter and 600nm in depth from the top surface of a 4μm thick boron-doped ($10^{15}cm^{-3}$) Si layer epitaxially-grown on a similarly doped substrate. A 100nm-thick SiO_2 layer surrounds the diode. The bias was applied across the diode by a sprung wire to a

300nm-thick Al contact on the n-type Si surface, the gold-coated back surface of the Si substrate being permanently grounded. The depletion region extends from the n-Si/p-Si interface for approximately 0.5 to 1μm at zero bias. Divacancies were introduced into the diode by blanket 1.5 MeV B^+ ion implantation at a dose of $10^{13}cm^{-2}$; their presence is denoted by the small open circles on the diagram, and their depth distribution is represented by the simulation results from the program SRIM[47] (Stopping and Range of Ions in Matter). The B^+ ion dose was chosen so as not to destroy the diode properties of the structure – i.e., to create an average divacancy concentration in the depletion region of no more than a few x 10^{17} cm^{-3}, guided by the expression of Coleman et al.[48]

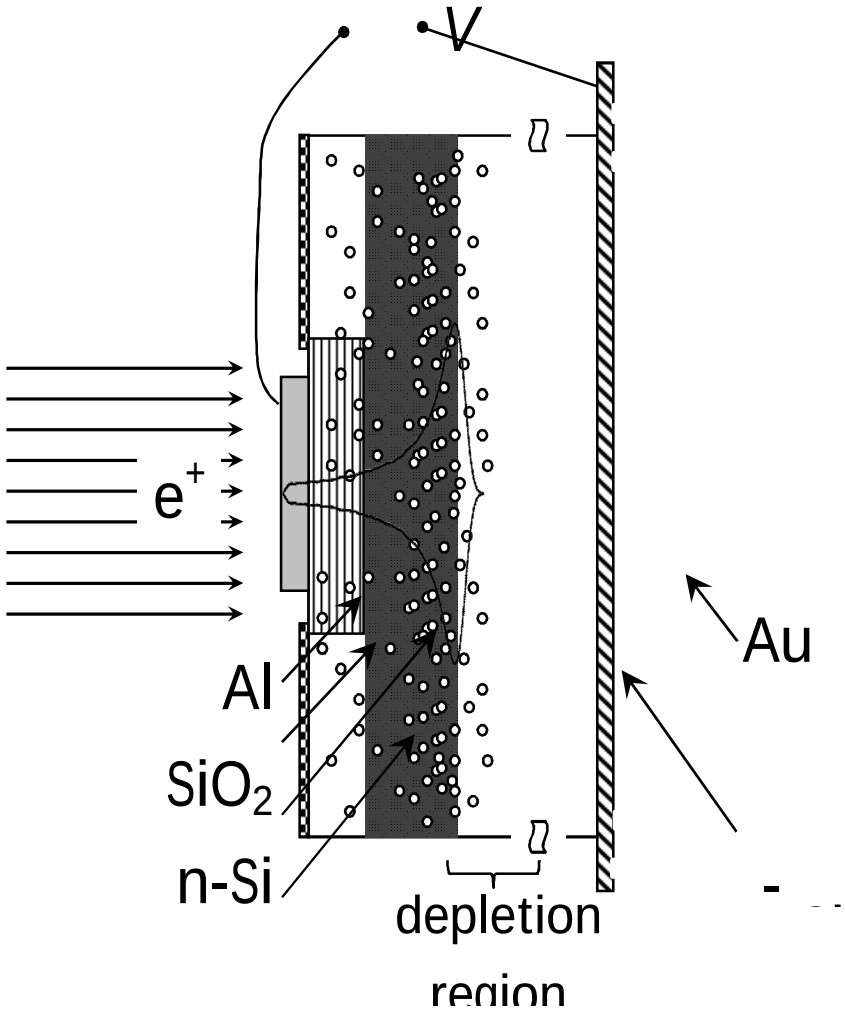

Figure 5.4.1: Schematic sample diagram. Horizontal dimensions are to scale; on the same scale, vertical dimensions are reduced by a factor of 10^3. The bell-shaped curve represents the results of a SRIM simulation of vacancy depth profile.[37] The small circles are sketched to represent vacancy-type damage.

This was verified by measuring the *I-V* characteristics of identical diodes with and without B implantation; in reverse bias (here corresponding to the application of positive potentials on the front surface) the current increased to 320 and 50μA at 5V, and in forward bias to –1mA at -0.3 and -0.6V, respectively. VEPAS was performed on the unimplanted and implanted diodes using a 4mm-diameter positron beam. Initial measurements of the Doppler-broadened lineshape parameter, *S*,[49] as a function of incident positron energy, *E*, demonstrated that at *E* = 18keV the measured value of *S* represented the mean value characteristic of the depletion region.

5.4-III Results and Discussion

With *E* fixed at 18keV, *S* was then measured for diode bias voltages from -1 to +10V, and the results are shown in Fig. 5.4.2.

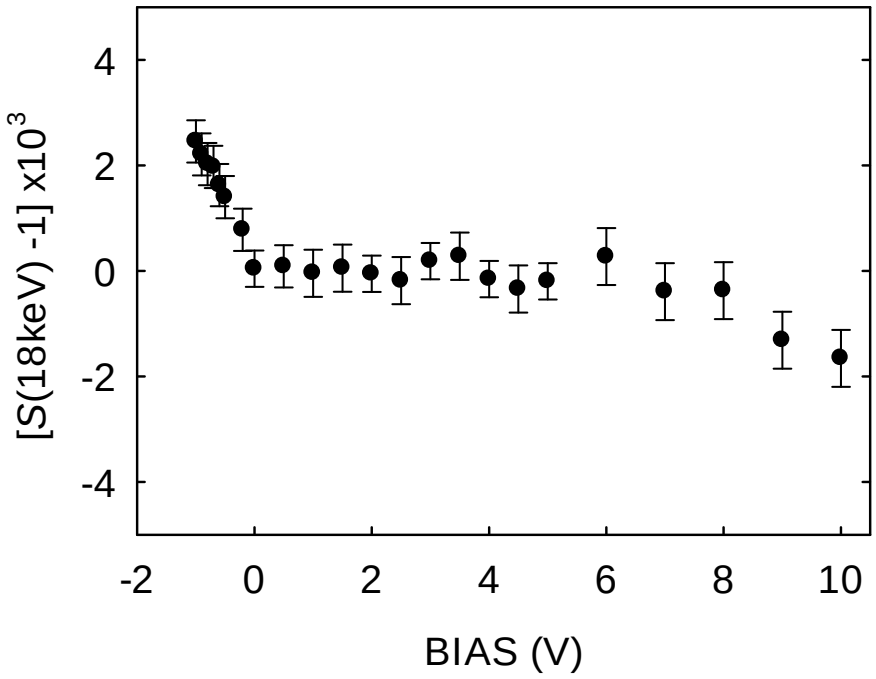

Figure 5.4.2: ΔS(18keV) for the implanted diode as a function of bias. ΔS is the difference between S(18keV) for the implanted diode and its mean value under low reverse bias conditions, multiplied by 10^3.

The small decrease in *S* at high reverse bias reflects the decrease in the positron trapping rate as the positron (drift) velocity increases. However, the significant change in *S* seen from 0 to -1V (forward) bias reflects the increase in the fraction of divacancies which have trapped one

or two electrons as the diode current increases. The increase in S shows an approximately linear dependence on diode current above ~ 1mA, as shown in Fig. 5.4.3.

The values of S characteristic of positrons trapped in charged and neutral V_2 are essentially the same; the observed increase in S reflects the increase in the trapped positron fraction resulting from the higher specific trapping rate for positrons in negatively-charged V_2.

It is possible to estimate the fraction of V_2 which become charged under forward bias conditions as follows. The mean (neutral) V_2^0 concentration C in the depletion region for the implanted diode under zero bias is $(\lambda/\nu_0)[(S_0-S_B)/(S_D-S)]$, where λ is the positron decay rate in

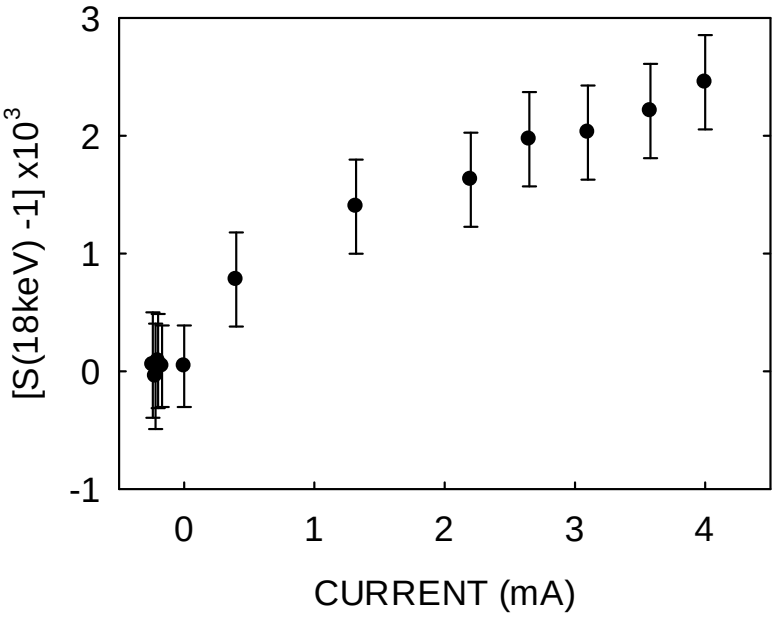

Figure 5.4.3: ΔS(18keV) for the implanted diode as a function of current. ΔS is the difference between S(18keV) for the implanted diode and its mean value under low reverse bias conditions, multiplied by 10^3.

undefected Si ($4.54 \times 10^9 s^{-1}$), ν_0 is the specific positron trapping rate for V_2^0 ($6.8 \times 10^{14} s^{-1}$), S_0 is the measured S value for the defected region normalized to the bulk value (1.020), S_B is the bulk Si parameter (1.000), and S_D is the S value characteristic of V_2 (1.036). Hence C = 8.7 x 10^{-6} per atom, or 4.4 x 10^{17} cm^{-3}, in line with expectations.

The fraction of positrons trapped in V_2^0, f_0, is thus $(S_0 - S_B)/(S_D - S_B)$ = 57%. When -1V bias is applied, S increases to 1.0223(5) and, assuming that S_D remains unchanged, the trapped

fraction *f* increases to 64%.

Now, considering $f = f_0 + f_C$, where f_o and f_C are the fractions trapped in neutral and charged V_2, respectively, and using the alternative expression for $f = [1+\lambda/(\nu C)]^{-1}$, it can be written that $f_0 = [1+\lambda/(\nu_0(1-\alpha)C)]^{-1}$ and $f_C = [1+\lambda/(n\nu_0\alpha C)]^{-1}$, where n is the factor by which ν_0 is increased for negatively-charged V_2 and α is the fraction of V_2 which are charged. Note that it is not assumed that the charge state is V_2^- or V_2^{2-} ; the value of n is thus an average for both states. If one then substitutes the values above for f, λ, ν_0 and C, one can solve the resulting quadratic equation to obtain α as a function of n, as shown in Fig. 5.4.4.

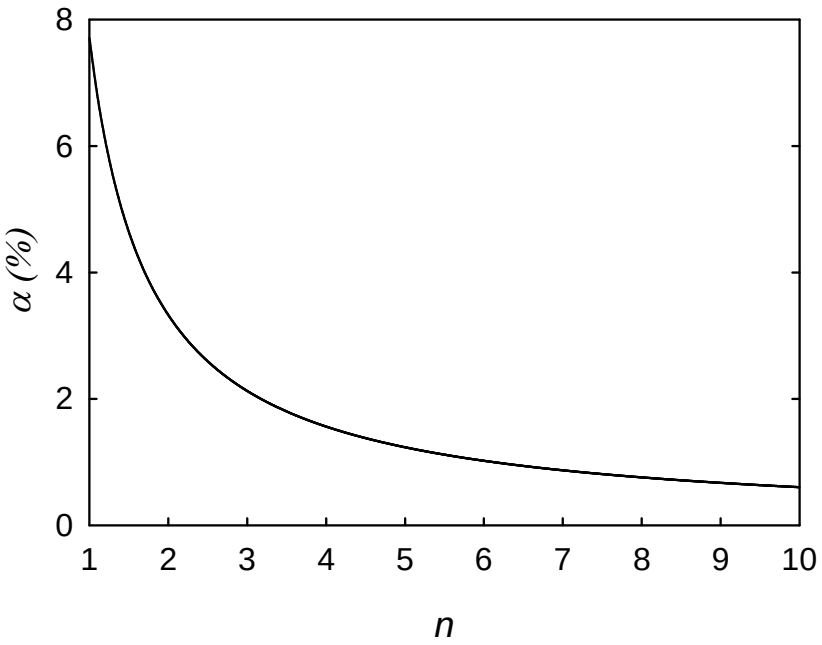

Figure 5.4.4: The fraction of V_2 which are negatively charged plotted as a function of the prefactor n for the specific positron trapping rate ν ; $\nu = n\nu_0$, where ν_0 is the rate for neutral V_2.

Here one can see that the fraction of V_2^0 which become charged in order to give the higher measured *S* value under forward bias of -1V is only of the order of a few percent – e.g., if $\bar{\nu} \geq 10$, as suggested by Kawasuso et al.,[46] then α is below 1%.

In principle, it should be possible to estimate the fraction of charged defects under the experimental conditions described using equation (1) for comparative purposes. In practice this is difficult given that it would require knowledge of both σ_n and σ_p, while any solution

should be specific to the device structure (including defect concentration) and bias conditions used. However, by using commercial device simulation software such as the code ATLAS by Silvaco, the structure described here has been simulated under bias of -1V. ATLAS calculates the fraction of charged defects in a manner consistent with Ref. [36]. The sensitivity in defect occupancy is dominated in this case by the coupled parameters representing the electron and hole capture cross-sections (σ_n and σ_p). If it is assumed that the dominant defect is the neutral divacancy (in the unbiased case), then σ_n = 2x10^{-15}cm^{-2},[38, 39] with a trap level of 0.4eV below the conduction band.[40] The defect concentration (supplied by the inactivated B^+ implantation) is fixed in the

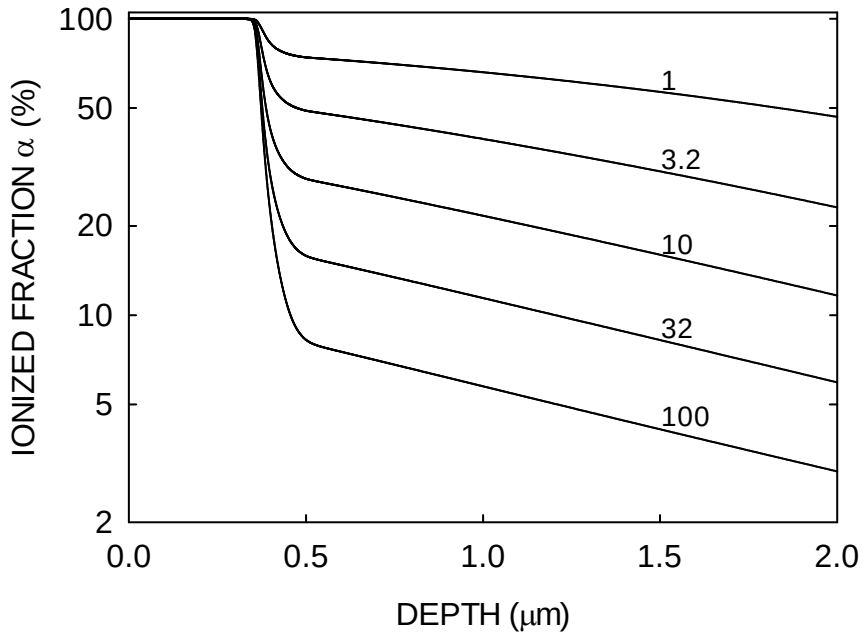

Figure 5.4.5: Simulation results, for the diode structure used in these studies under a bias of -1V, for the fraction of charged V_2 as a function of depth: plot labels are hole capture cross sections in $10^{-17}cm^2$: trap energy level = 0.4eV: trap (V_2) concentration = $5x10^{17}cm^{-3}$: electron capture cross section = $2x10^{-15}cm^2$.

simulation at 5x10^{17}cm^{-3} throughout the sample. Fig. 5.4.5 shows the concentration of ionized defects as a function of depth for a range of values of σ_p.

It is clear that for consistency with the experimental result (i.e. that the fraction of charged

divacancies ~1%) σ_p ~ 1x10^{-15}cm^{-2} or greater; a value at the upper end of expectation, but not unreasonable.

First measurements of the de-filling rate of charged V_2 have been made by applying a square-wave bias to the diode, as shown schematically in Fig. 5.4.6.

-1V was applied for 20% of the duty cycle, as the filling rate is considered to be so fast (~ns) that the V_2 can be considered to be in the equilibrium charged state throughout this part of the cycle. When the bias is removed, for a preset time *T*, the number of charged V_2 decreases

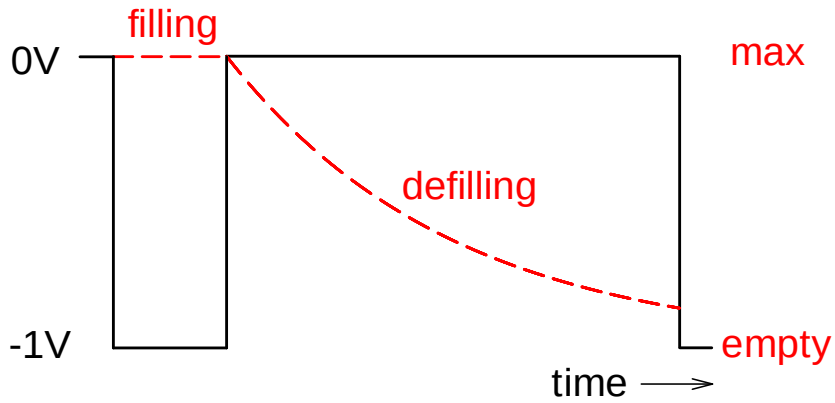

Figure 5.4.6: Solid (black) line: diode bias, with a duty cycle of 1:4 (on:off). Typical time periods: 1-50 μs. Filling in the 'on' state is assumed to be essentially instantaneous in the time scales used, and de-filling in the 'off' state is represented by an exponential decrease of charged V_2 concentration, represented by the broken (red) line.

exponentially with a time constant τ whose value depends on the charge state. This occurs as a result of electron emission and hole capture in the now present depletion region. $\Delta S(0)$ (= 0.0023(1)) was measured at regular intervals by alternating the diode bias (in dc mode) between -1 and 0V and measuring *S* in each state to a high level of accuracy, multiplying by 80% before using as the $T = 0$ value on a plot of $\Delta S(T)$ values determined using the square-wave bias technique.

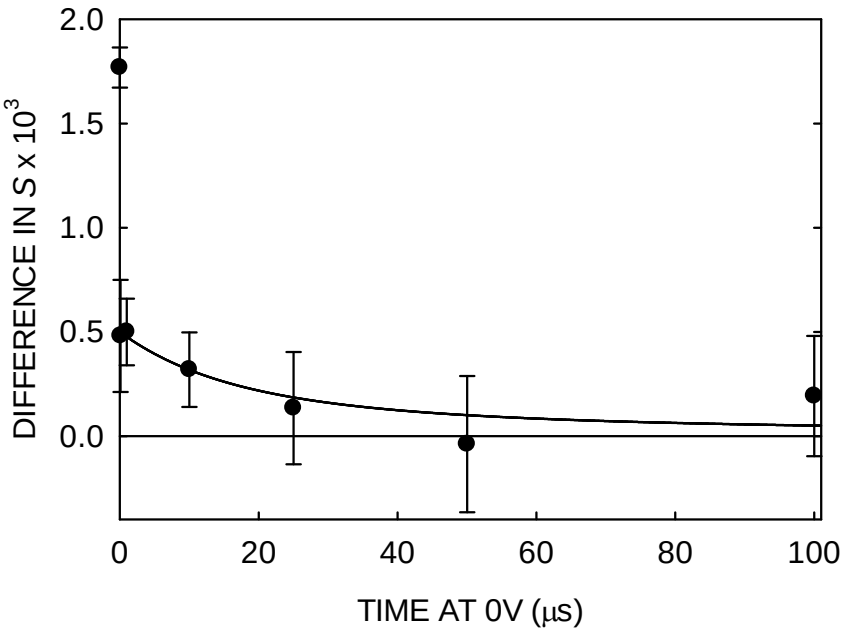

Figure 5.4.7: ΔS(18keV) as a function of time spent at 0V (in each duty cycle – see Fig. 5.4.6). The solid line represents a de-filling time constant (for singly-charged V_2) of 10 μs.

Fig. 5.4.7 shows the experimental results for the square-wave measurements. $\Delta S(T)$ shows an almost immediate and significant decrease, falling to 0.0005 for T = 100ns. This is consistent with the de-filling of V_2^{2-} to V_2^- (or --/- in the accepted notation) with a decay time of 13ns, and on the time scale used in the present study can be considered as instantaneous. τ_2 = 13ns is the time constant at room temperature predicted by extrapolating low-temperature Arrhenius plots using data from Refs. [37] and [41]. Therefore a model can be constructed by which $\Delta S(T)$ is computed using the following approach, considering all the charged V_2 to be in the singly-charged state at T = 0 and emptying with a single time constant τ_1. During any given de-filling time period T, with reference to Fig. 5.4.6, the fractional positron response to charged V_2 is determined by $F_C(T)$, the fractional area of the de-filling rectangle beneath the exponential: $F_C(T)= (\tau_1/T)[1-\exp(-T/\tau_1)]$. The change in S parameter $\Delta S_C = [S - S(0)]$ is proportional to the fraction f of positrons trapped in V_2^-. Thus $\Delta S(T)/\Delta S(0) = [1+\lambda/(n\nu_0\alpha C)]/[1+\lambda/(n\nu_0\alpha C F_C(T))]$. The solid line in Fig. 5.4.7 uses τ_1 = 10 μs in the expression for $F_C(T)$.

A de-filling time constant of ~10 μs is consistent with the V_2^- to V_2^0 (-/0) transition; extrapolation of the low-temperature DLTS data of Ref. [41] yields the room-temperature value τ_1 = 33 μs. It should be stressed that the present data only suggest that $\tau_1 \sim 10^1$ μs; the non-

zero measurement at T = 100 μs suggests that a τ_1 of ~ 30 μs is possible.

Information can be extracted from Fig. 5.4.7 about the specific positron trapping rates for, and the relative populations of, singly- and doubly-charged V_2. The relatively instantaneous decrease of ΔS near T = 0 corresponds to the transition from doubly- to singly-charged V_2; let this decrease be represented by the ratio $R = \Delta S(0)/\Delta S(100\text{ns})$. Now ΔS is here proportional to the fraction of positrons trapped in the charged defects, i.e. $[1+\lambda/\nu C_C]$, where ν is the appropriate specific trapping rate and C_C the corresponding concentration of charged defects. If C_C is small – as is indicated by Fig. 5.4.4 – then $\lambda/\nu C_C \gg 1$ and $\Delta S \propto \nu C_C$. It can therefore be written $R \approx [n\nu_1(1\text{-}\beta)C_C + \nu_1\beta C_C]/[\nu_1 C_C] = [n + \beta\,(1\text{-}n)]$, where ν_1 is specific positron trapping rate for V_2^-, $n\nu_1$ the rate for V_2^{2-}, and β is the fraction of charged defects in the V_2^- state at T = 0. In general, if it is assumed that $n \approx 3$ (the highest value of n expected from earlier measurements)[39] then measurement of R (in the range 1 to 3) yields a value for β. Fig. 5.4.7 gives R = 3.5; this suggests n = 3.5 and β = 0 – that is, all of the charged defects at T = 0 are in the doubly-charged state. In this case a value of $\beta < 1$ would require $n > 3.5$, which is not consistent with earlier evidence.

5.4-IV Conclusions - Electron Capture and Re-Emission in Si

In summary, charge transient positron spectroscopy has yielded information on negatively-charged V_2 in a silicon diode structure. In forward bias the positron response increases as ≤ 1% of the defects become negatively charged. By applying a square-wave bias to the diode the emptying of the divacancies at room temperature was studied and the results were consistent with V_2(--/-) having a time constant τ ~ 13ns followed by the much slower V_2(-/0) with $\tau \sim 10^1$ns. This ac technique allows direct estimation of the relative populations of singly- and doubly-charged V_2 in the biased diode. This is the first demonstration of a technique which provides both structural information on a defect (i.e. the positron response provides evidence for the type and size of the open volume defect) and the electrical properties (i.e. the carrier capture and emission rates). This method may be applied to a range of defects in various semiconductor structures. Further, with the extension to temperature variable measurements, the energy of the level within the bandgap may be extracted.

5.5 Probing the formation of Silicon nano-crystals (Si-ncs) using Variable Energy Positron Annihilation Spectroscopy

5.5-I Introduction

Low dimensional silicon continues to be of considerable interest for applications such as silicon based solid state lighting, non-volatile memories and dielectric engineering.[50] Specifically, silicon nanocrystals (Si-ncs) formed in the dielectric material SiO_2 or Si_3N_4 have been shown to possess a range of properties not usually associated with the silicon bulk. Such nano-crystals are formed via phase separation in silicon-rich dielectric. This precursor material may be fabricated using a number of standard processes such as plasma enhanced chemical vapour deposition[51] or sputtering, both suitable for high-volume, large area applications. The most controllable fabrication technique (and thus the preferred method for the methodical study of Si-ncs) is ion implantation.[52] In this case, excess silicon is introduced into stoichiometric, thermally grown SiO_2, with phase separation taking place during a subsequent high temperature (>1000ºC) annealing step. This work shows the significant potential of VEPAS for obtaining novel information on the formation and light emitting potential of Si-ncs formed via high dose Si^+ ion implantation of SiO_2. It is demonstrated that VEPAS shows a strong relationship between the damage contained in the SiO_2 (resulting from the implantation process) and the formation mechanics of the Si-ncs. Previous hypotheses are confirmed that the interface plays a significant role in the light emission from Si-ncs. This is achieved through the observation of the VEPAS signal for Si-ncs with and without interface passivation.

5.5-II Experimental Procedure

All of the samples reported here were prepared via high dose ($>1x10^{16}cm^{-2}$) Si^+ ion implantation into thermally grown SiO_2 thin films on a low-doped *p*-type silicon substrate; followed by a high temperature (>1000ºC) anneal in N_2. A fraction of the films were subsequently annealed at 500ºC for 10 minutes in forming gas (N_2:H_2 95:5).

Confirmation of the presence of Si-ncs was obtained via Transmission Electron Microscopy (TEM) using a conventional CM-12 microscope operated at 120 kV. Cross-sectional

specimens oriented along the {110} zone axis were prepared by mechanical polishing, followed by ion milling. Dark-field examinations were carried out with two beam diffraction condition (***g*** = 220) relative to the Si substrate.

Photoluminescence (PL) measurements were performed using the 405 nm line of an InGaN/GaN laser diode operating at 50 mW. The spectra were collected using a CCD array. VEPAS spectra were analysed in terms of *S*-parameter for incident positron energies ranging from 0.1-30keV.

5.5-III Results and Discussion

Fig. 5.5.1 shows an example of a TEM image of a collection of Si-ncs, in this case for a sample prepared using an implantation dose of $8x10^{16}cm^{-2}$ and energy of 80 keV.

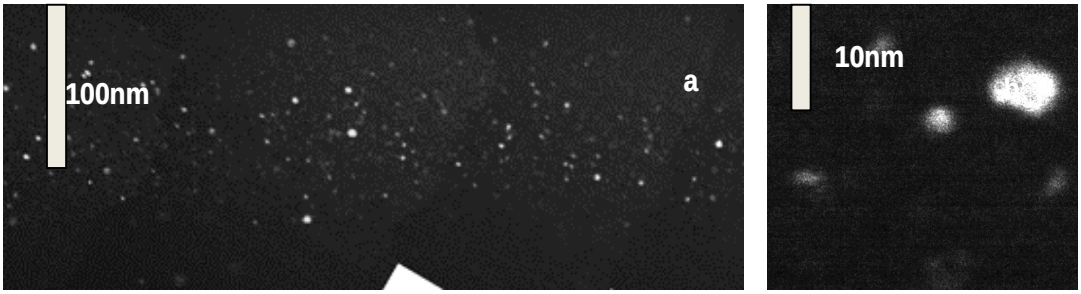

Figure 5.5.1: Dark field TEM image of Si-ncs in SiO_2; (a) wide view of distribution; (b) enlarged view of Si-nc.

Following ion implantation the sample was annealed at a temperature of 1150ºC for 50 s. The phase separation leading to the formation of the Si-ncs is confirmed, with the Si-ncs showing as light regions (in the dark field image). In this case the mean diameter of the Si-ncs was approximately 3 nm.

The structure of Si^+ ion implanted SiO_2/Si (SiO_2 film thickness = 500 nm) as a function of annealing time was characterized using VEPAS for a sample set again prepared using an implantation energy and dose of 80 keV and $8x10^{16}cm^{-2}$ respectively. The annealing was performed at 1100ºC for times ranging from 1-100 seconds. The *S* parameter (normalized to bulk silicon) versus incident positron energy is shown in Fig. 5.5.2.

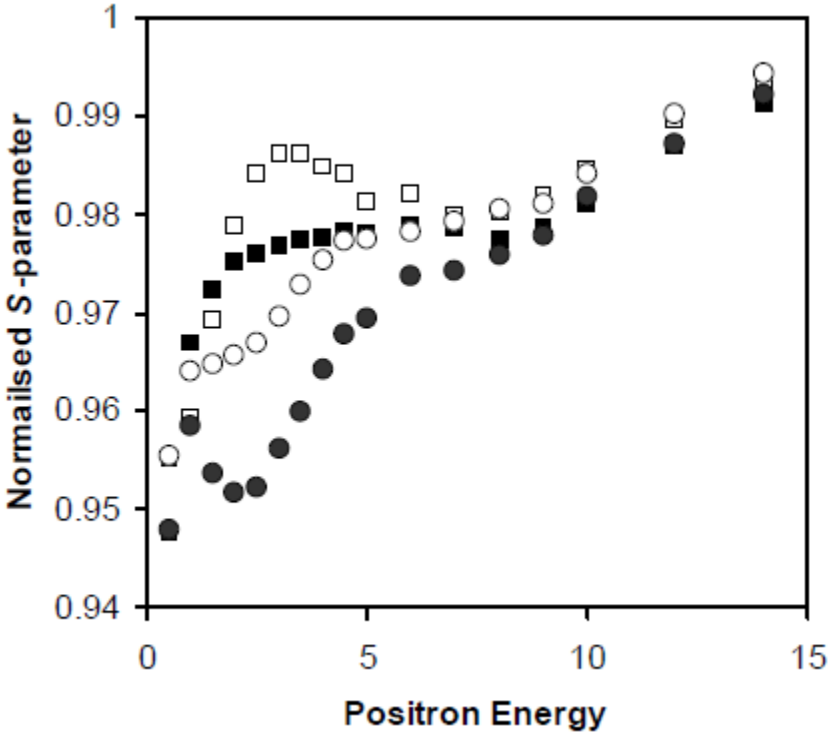

Figure 5.5.2: Normalized S parameter versus positron energy (and mean positron implantation depth) for samples implanted with $8x10^{16}$ cm^{-2} at an ion energy of 80 keV and annealed at 1100^{o}C for 1 s (open circles) and 100 s (closed circles). Data for the unimplanted film shown as closed squares, and for the as-implanted (unannealed) shown as open squares.

Data for annealing times between 1 and 100 seconds (exclusive) showed a slowly varying trend of reduction in *S* parameter for the region between 1-7 keV, and is not shown in order to maintain clarity.

The data for the unimplanted SiO_2/Si film is consistent with a film thickness of 500 nm with strong positron trapping at the SiO_2/Si interface. Following the relatively high dose ion implantation the *S* parameter corresponding to the end of range of the implanted ions increases (positron energy ~3.5 keV), signifying the likely introduction of large open volumes. Somewhat remarkably, even for an annealing time of 1 s, there is a significant drop in *S* parameter at an energy (1-5 keV) which would be consistent with the expected phase separation of the excess implanted Si. This reduction in *S* parameter continues to an annealing time of 100 s, after which negligible evolution in the shape of the *S-E* data is observed (data not shown for clarity). Consistent with a previous report[53] the 'dip' in the

VEPAS data at ~2.5 keV comes from annihilations which take place at the interface of the Si-ncs and the host SiO_2.

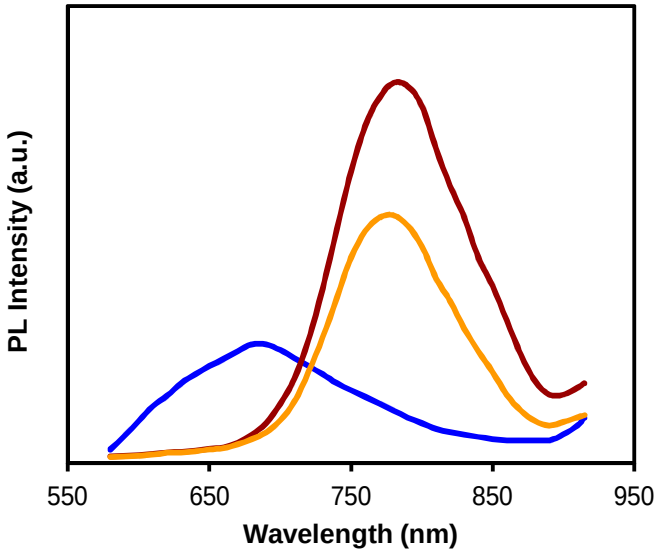

Figure 5.5.3: Photoluminescence data for samples implanted with $8x10^{16}$ cm^{-2} and annealed at 1100ºC for 1 s (orange line) and 100 s (red line). Data for the as-implanted sample is also shown (blue line). The as-implanted data has been multiplied 10 times to allow comparison.

Photoluminescence data shown in Fig. 5.5.3 was obtained from the same samples as those used to obtain the VEPAS data. For the as-implanted sample there is a measurable but small luminescence signal centred at 670 nm which likely results from luminescent defects. After annealing for 1 s the formation of Si-ncs is confirmed by the large increase in signal strength and the shift in emission wavelength to ~770 nm. Further annealing for 100 s results in a small red-shift of emission wavelength (consistent with an increase in size of the average diameter of the Si-ncs) and a significant increase in luminescence intensity. This intensity increase occurs with concomitant reduction in structural damage of the SiO_2 shown by Fig. 5.5.2. This is likely then due to the removal of non-radiative recombination centres. The VEPAS technique thus provides an important method through which the removal of luminescence suppression may be monitored.

Despite the importance of the Si-nc/SiO_2 interface to luminescence[50] there remain few techniques which may be used to probe the bonds between the oxide and silicon directly. Fig. 5.5.4 shows data similar to that in Fig. 5.5.2.

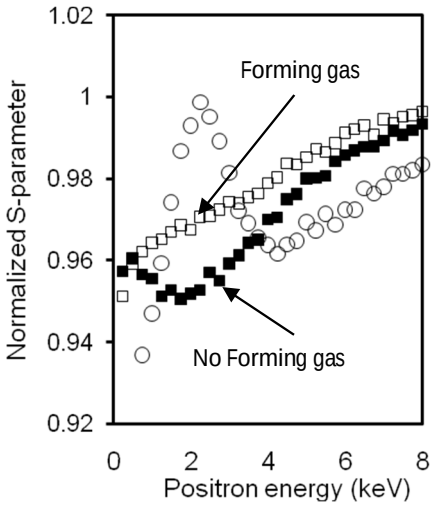

Figure 5.5.4: Normalized S parameter versus positron energy for samples implanted with $4x10^{16}$ cm^{-2} at an ion energy of 40 keV and annealed at 1100°C for 100 s in N_2 (closed squares); 1100 °C for 100 s N_2, followed by forming gas anneal at 500 °C for 600 s (open circles). Data for as-implanted (unannealed) is shown as open circles.

In this case though, the excess silicon has been introduced via a 40 keV Si^+ ion implantation to a dose of $4x10^{16}cm^{-2}$. The thickness of the SiO_2 film was nominally 100 nm. The implantation again induces structural damage to the oxide film indicated by an increased *S* parameter in the energy range 1.5-3 keV. Following annealing at 1100ºC for 100 s in N_2 the formation of Si-ncs results in a 'dip' in the data, centred at ~2 keV, associated with trapping of positrons at the Si-nc/oxide interface. Following a second anneal at 500ºC for 600 s in forming gas (containing 5% H_2), the trapping of positrons at the interface is significantly suppressed, and hence the 'dip'is removed. This is consistent with the passivation of defects at the Si-nc surface, an effect which has been documented as inducing a large increase in the luminescence yield.[54]

5.5-IV Conclusions - Formation of Silicon Nano-Crystals

Preliminary data has been presented on the use of VEPAS to probe the formation of Si-ncs in SiO_2. There are few techniques which can provide similar depth-resolved information on this technologically important system. VEPAS monitors the removal of luminescence suppressing defects following high dose ion implantation. Further, it is able to sensitively probe the interface of Si-ncs and the host SiO_2. Significant work is planned in the near future

combining VEPAS, electron microscopy and photoluminescence on similar material systems and those doped with rare-earths such as erbium and cerium.

5.6 Silicon Quantum Well Interfaces

5.6-I Introduction

The silicon-silicon dioxide interface is one of the most important interfaces in the infrastructure of modern society on which much of modern information and communication technology is built. Recent experiments, however, have unexpectedly revealed that certain preparation conditions lead to a new type of interface at which the electronic properties are profoundly altered.[55]

Smart Cut technology, developed at CEA-LETI, was used to transfer ultra-thin single crystal layers of wafer substrate material (such as silicon) onto another surface. Differing from traditional layer-transfer techniques, which are based mainly on wafer bonding and etch-back or epitaxial lift-off, the Smart Cut approach uses a thermal activation process as an "atomic scalpel". It slices the wafer horizontally, lifting off a thin layer from the donor substrate and placing it onto a new substrate. Inherently, this process offers better control, and a single donor substrate can be reused many times for further layer transfers. UNIBOND is a line of SOI wafers created using the Smart Cut process technology.

A SIMOX SOI substrate is prepared by ion implantation of oxygen into a {100} silicon wafer followed by high-temperature annealing, leading to a buried layer of SiO_2 or BOX (buried oxide). Despite the initial continuous spatial distribution of implanted oxygen atoms, annealing at high temperature for a prolonged period of time is known to yield abrupt Si/SiO_2 interfaces and recrystallization of the implantation-damaged silicon. MOSFET's fabricated on these SOI substrates lead to $SiO_2/Si/SiO_2$ quantum wells where the BOX acts as an intrinsic back-gate insulator.

It is the interfaces of the $SiO_2/Si/SiO_2$ quantum wells created by both methods that are of interest in this study. The unique electronic properties at each interface can cause valley splitting, the reason for this is still not fully understood. Oxidised SOI wafers were created by Dr Akira Fujiwara at NTT Basic Research Laboratories using the Smart Cut process

(UNIBOND) or SIMOX (separation by implantation of oxygen)[56,57,58] and have been studied using VEPAS. Positrons are particularly sensitive to interfaces and can diffuse freely through Si making them ideal SOI probes.

5.6-II Experimental Procedure

The $SiO_2/Si/SiO_2$ quantum well interfaces, interfaces 1 and 2 in Fig. 5.6.1, are of prime interest with interface 3 studied as an aside.

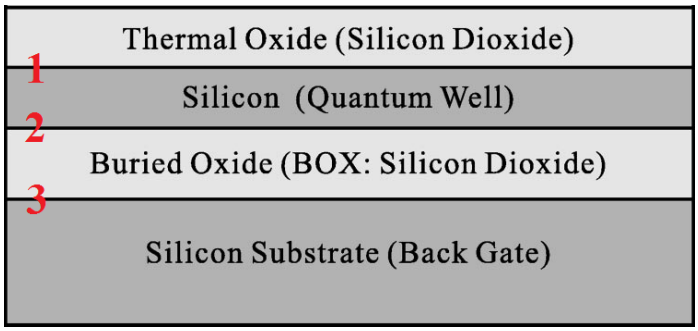

Figure 5.6.1: A schematic diagram of both the UNIBOND and SIMOX sample structures with each interface numbered.

The UNIBOND sample has $SiO_2/Si/SiO_2$ layer thicknesses of 28nm/29nm/400nm respectively. Interface 1 was created between thermal SiO_2 and standard Si layers, formed during a 900-1100ºC anneal in 100% O_2. The morphology of interface 1 is random, as measured by atomic force microscopy at NTT. Interface 2 was created in the same way as 1 but has also undergone extra annealing during bonding.

The SIMOX sample has $SiO_2/Si/SiO_2$ layer thicknesses of 232nm/104nm/387nm respectively. It is important to note that the interfaces are buried much deeper than in the UNIBOND sample, affecting the sensitivity of the positrons to them. Interface 1 was created during the BOX anneal. Currently, the electronic transport properties of this interface are unknown. The interface has a stop-terrace morphology. Interface 2 is between the Si and BOX layers, formed during a 1350ºC anneal for 48h in 5% O_2, 95% Ar. It is known to have large valley splitting.

An 8nm quantum well behaves as a single layer of two-dimentional electrons at accessible gate voltages and arises due to the topological differences between the two interfaces.

However, it is unknown how these microscopic differences lead to the observed differences causing the valley splitting. It is predicted that interface 1 and 2 should be the same within each sample but different between samples, due to the different creation techniques.

VEPAS spectra were analysed in terms of *S* and *W*-parameters for incident positron energies ranging from 0.25-20keV.

5.6-III Results and Discussion

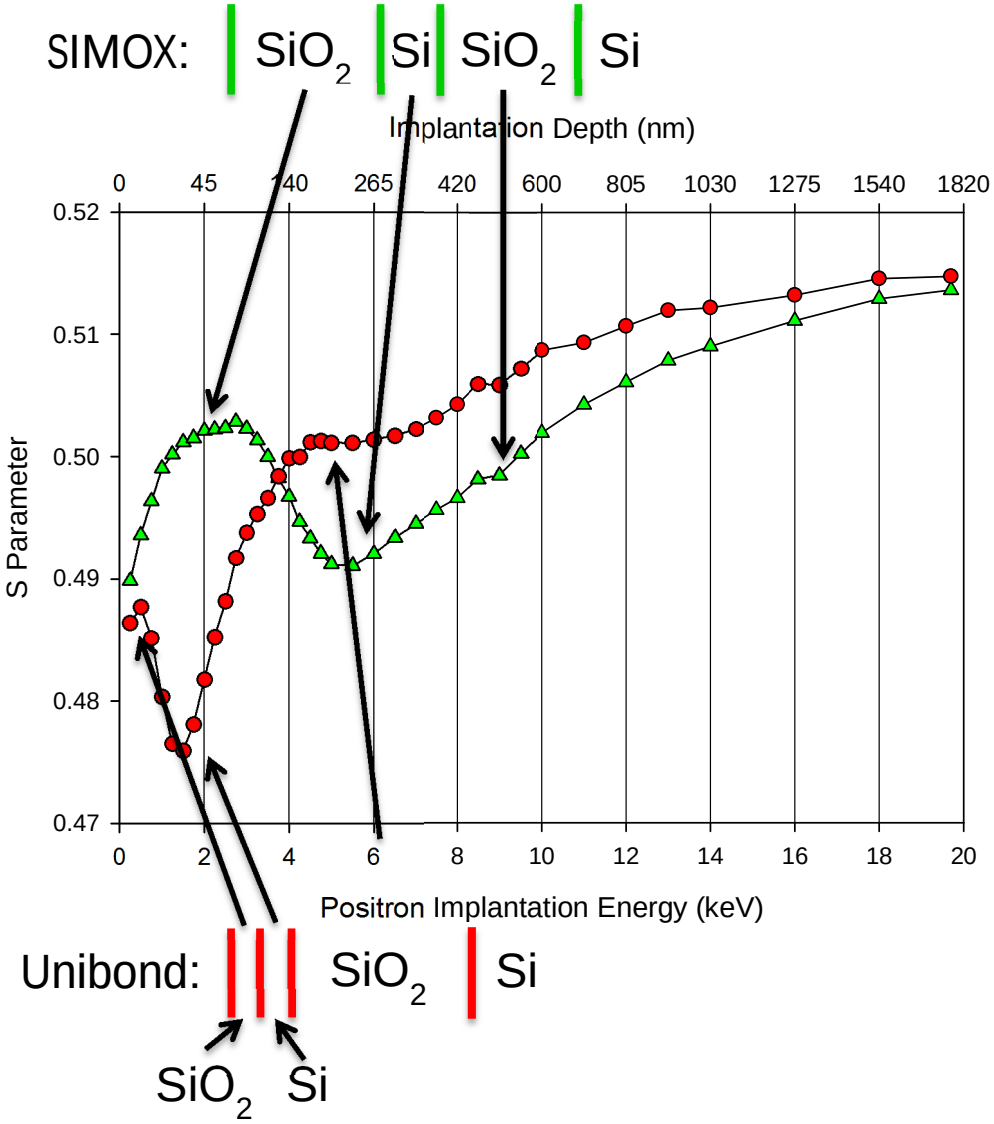

Figure 5.6.2: S(E) plot for the UNIBOND and SIMOX samples. Mean positron implantation depth and S(E) features corresponding to sample layers are also shown.

Figure 5.6.2 shows the *S*(*E*) plot for the two samples. Each layer of the samples (SiO2/Si/SiO2/Si) can be seen, with the difference in shape arising from the different layer thicknesses.

While the layers themselves are clearly visible in Fig. 5.6.2, the interfaces are not. Plotting the data as an *S*-*W* plot, seen in Fig. 5.6.3, reveals these interfaces as additional positron trapping sites.

Samples of Si, SiO_2 and damaged SiO_2 were also measured and plotted with the two samples to reveal these pure states on the *S*-*W* plot. After normalisation the data for the samples can be seen to go between these points with an additional trapping site marked interface 3 in Fig. 5.6.3. Interface 3 appears to look like slightly damaged SiO_2, with no Si response. Each site is marked with a circle as a separate trapping layer fitted with VEPFIT. Both samples have the

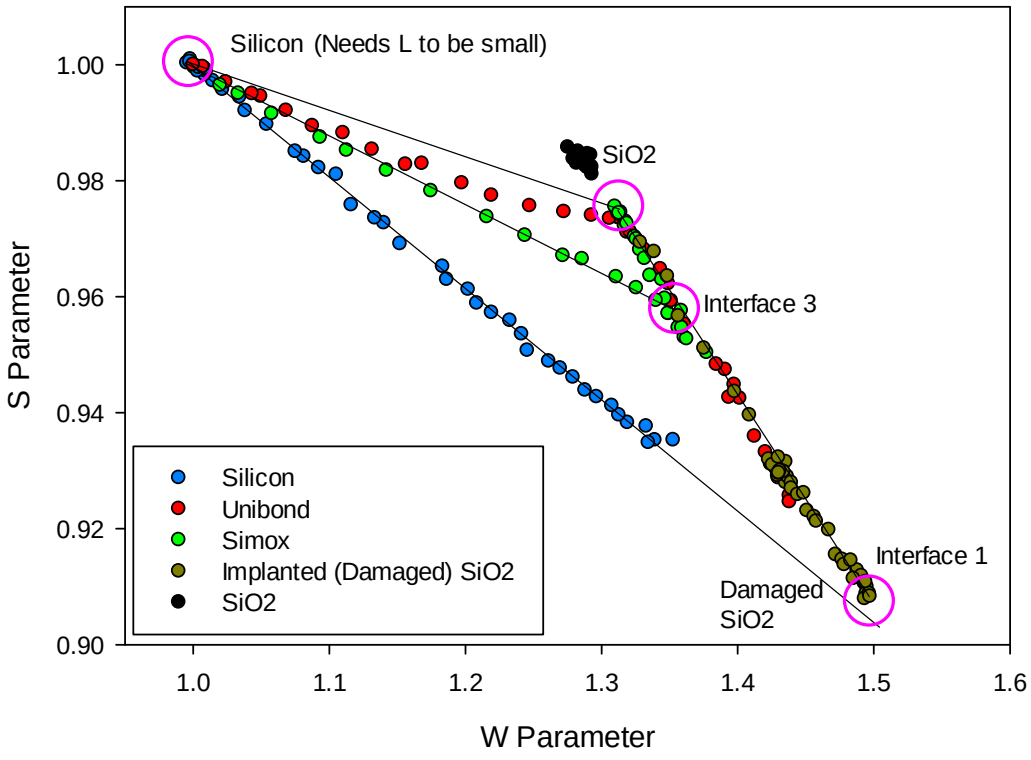

Figure 5.6.3: Normalised S-W plot for the UNIBOND and SIMOX samples. Plots for Si, SiO_2 and implanted SiO_2 are shown for reference. Circles indicate different states.

same interface fits. While interface 1 is marked on the graph as very damaged SiO_2, it is difficult to determine the *S*-*W* point for interface 2. This is due to the free positron diffusion

length being longer than Si layer width meaning it is difficult to distinguish between interfaces 1 and 2.

Both samples were plotted separately to distinguish any additional features. Fig. 5.6.4 shows the *S-W* plot for the SIMOX sample.

The implantation energies for the different features are shown on the graph and correspond to the following:

2.75 keV = ~115 nm (middle of shallow SiO_2 layer)
5.5 keV = ~230 nm (interface 1 - shallow SiO_2 / Si boundary)
6.5 keV = ~330 nm (interface 2 - Si / buried SiO_2 boundary)

Interface 1 can be seen at 5.5 keV but interfaces 2 and 3 appear to be same. Interface 3 should

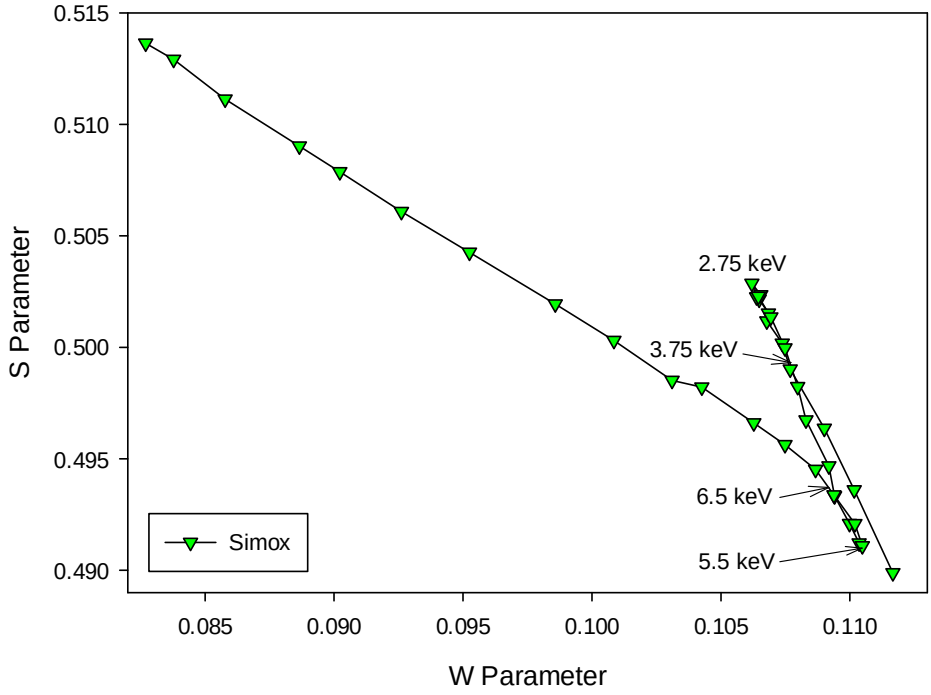

Figure 5.6.4: S-W plot for the SIMOX sample. Implantation energies are shown for different features.

be clearly visible with back-diffusion in the bulk Si, so either interface 2 and 3 are the same or interface 2 cannot be seen.

The UNIBOND sample has a similar *S-W* plot, shown in Fig. 5.6.5.

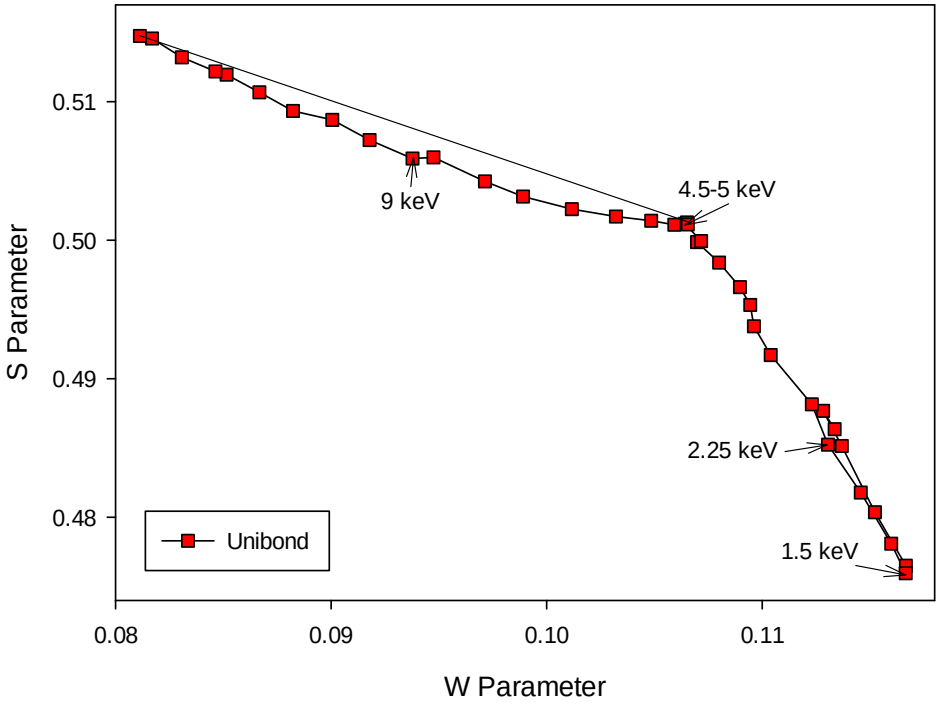

Figure 5.6.5: S-W plot for the UNIBOND sample. Implantation energies are shown for different features.

The implantation energies for the different features are shown on the graph and correspond to the following:

1.5 keV = ~28 nm (interface 1 - shallow SiO_2 / Si boundary)

2.25 keV = ~57 nm (interface 2 - Si / buried SiO_2 boundary)

4.5-5 keV = middle of buried SiO_2 layer

9 keV = (interface 3 - buried SiO_2 / Si boundary)

The buried SiO2/Si boundary (interface 3) never quite reaches 100% annihilations in this region. The reason for this is not fully understood as this interface is much shallower than the same interface in the SIMOX sample and so the sensitivity to it should be greater. One possible reason is the positron diffusion in the bulk Si is low, reducing the response to interface 3. This is backed up by VEPFIT which needs a small diffusion length, *L*, to fit the data. The cause of this is currently unknown.

In order to see interface 2, an 5% HF solution was used to etch off the top SiO_2 in both samples. This process would reveal the Si removing interface 1 and leaving just interfaces 2

and 3. Fig. 5.6.6 shows the results before and after the HF etch. Si, SiO_2 and damaged SiO_2 are again displayed for reference. The initial slight deviation from the Si-damaged SiO_2 *S-W* line in the etched data is thought to arise from H-passivation. A new interface can clearly be seen along the Si-damaged SiO_2 line, which is believed to be interface 2. Unlike interface 1 it has some Si reponse. The SIMOX sample now has a reduced interface 3 reponse – similar to the original UNIBOND sample.

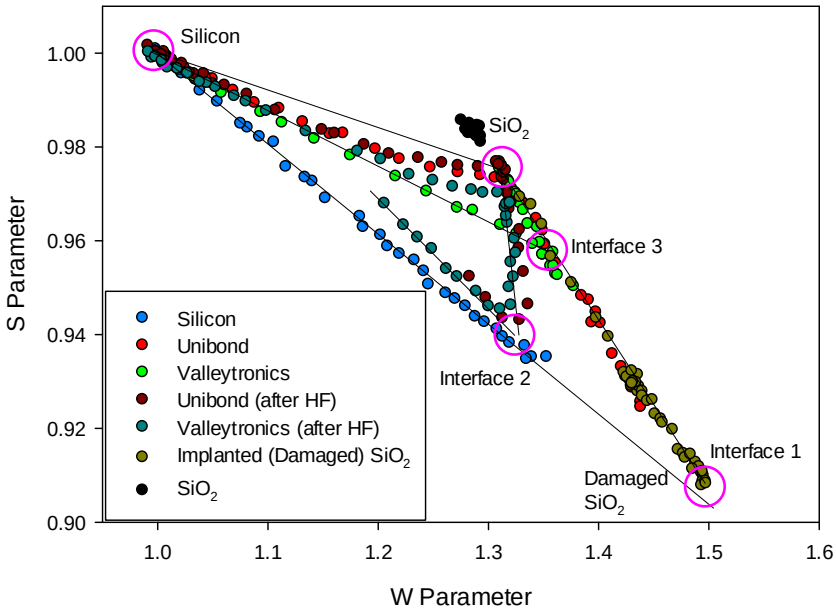

Figure 5.6.6: S-W plot for the UNIBOND and SIMOX samples before and after HF etching. Plots for Si, SiO_2 and damaged SiO_2 are shown for reference. Circles indicate different states.

5.6-IV Conclusions - Silicon Quantum Well Interfaces

Originally it was preddicted that interface 1 and 2 should be the same within each sample. Initial results however, indicate that there is a significant difference between the two Si/SiO_2 interfaces within each sample but between samples created by the two processes the corresponding interfaces are similar. The reason for this is that both interface 1s have undergone a similar high temperature anneal. Additionally, UNIBONDs interface 2 has undergone extra annealing which, possibly by coincidence, has the same effect as a BOX anneal. Valley splitting, therefore, is not due to any physical defects that positrons can detect. Another possible way to distinguish between interface 1 and 2 would be to apply bias to both samples to sweep positrons to either interface.

[1] D. A. Abdulmalik and P. G. Coleman, Phys. Rev. Lett. **100**, 095503 (2008).

[2] E. Chason, S. T. Picraux, J. M. Poate, J. O. Borland, M. I. Current, T. Diaz de la Rubia, D. J. Eaglesham, O. W. Holland, M. E. Law, C. W. Magee, J. W. Mayer, J. Melngailis, and A. F. Tasch, Journal of Applied Physics **81** (10), 6513 (1997).

[3] D. A. Brett, D. J. Llewellyn, and M. C. Ridgway, Applied Physics Letters **88** (22), 222107 (2006).

[4] X.-Q. Feng and Y. Huang, Int. J. Solids Struct. **41**, 4299 (2004).

[5] N. E. B. Cowern, B. Colombeau, J. Benson, A. J. Smith, W. Lerch, S. Paul, T. Graf, F. Cristiano, X. Hebras, and D. Bolze, Applied Physics Letters **86** (10), 101905 (2005).

[6] H. A. W. El Mubarek and P. Ashburn, Applied Physics Letters **83** (20), 4134 (2003).

[7] D. A. Abdulmalik, P. G. Coleman, N. E. B. Cowern, A. J. Smith, B. J. Sealy, W. Lerch, S. Paul, and F. Cristiano, Applied Physics Letters **89** (5), 052114 (2006).

[8] R. Kalyanaraman, T. E. Haynes, O. W. Holland, H.-J. L. Gossmann, C. S. Rafferty, and G. H. Gilmer, Applied Physics Letters **79** (13), 1983 (2001).

[9] R. Kalyanaraman, T. E. Haynes, M. Yoon, B. C. Larson, D. C. Jacobsen, H.-J. Gossmann, and C. S. Rafferty, Nucl. Instrum. Methods Phys. Res. B **175-7**, 182 (2001).

[10] A. J. Smith, R. M. Gwilliam, V. Stolojan, A. P. Knights, P. G. Coleman, A. Kallis, and S. H. Yeong, Journal of Applied Physics **106** (10), 103514 (2009).

[11] J. F. Ziegler, M. D. Ziegler, and J. P. Biersack, Nucl. Instrum. Methods Phys. Res. B **268**, 1818 (2010).

[12] P. J. Simpson, A. P. Knights, M. Chicoine, K. Dudeck, O. Moutanabbir, S. Ruffell, F. Schiettekatte, and B. Terreault, Appl. Surf. Sci. **255**, 63 (2008).

[13] M. Eldrup and K. O. Jensen, Phys. Status Solidi A **102**, 145 (1987).

[14] P. J. Schultz and K. G. Lynn, Rev. Mod. Phys. **60**, 701 (1988).

[15] Cowern N E B, Colombeau B, Benson J, Smith A J, Lerch W, Paul S, Graf T, Cristiano F, Hebras X, and Bolze D, Appl. Phys. Lett. **86**, 101905 (2005).

[16] Ziegler J F, Ziegler M D, and Biersack J P, Nucl. Instrum. Methods B **268**, 1818 (2010).

[17] Chilton N B and Coleman P G, Meas. Sci. Technol. **6**, 53 (1995).

[18] Coleman P G, Burrows C P, and Knights A P, Appl. Phys. Lett. **80**, 947 (2002).

[19] Coleman P G, Mason R E, van Dyken M, and Knights A P, J. Phys.: Condens. Matter **17**, S2323 (2005).

[20] Coleman P G, Harding R E, Davies G, Tan J, and Wong-Leung J, J. Mater. Sci: Mater. Electron. **18**, 695 (2007).

[21] Watkins G D and Corbett J W, Phys. Rev. **138**, A543 (1965).

[22] van Veen A, Schut H, de Vries J, Hakvoort R A, and Ijpma M R, AIP Conf. Proc. **218**, 171 (1990).

[23] Coleman P G and Burrows C P, Phys. Rev. Lett. **98**, 265502 (2007).

[24] H. A. W. El Mubarek and P. Ashburn, Appl. Phys. Lett. **83**, 4134 (2003).

[25] X. D. Pi, C. P. Burrows, and P. G. Coleman, Phys. Rev. Lett. **90**, 155901 (2003).

[26] F. Schäffler, Semicond. Sci. Technol. **12**, 1515 (1997).

[27] R. Kogler, A. Mucklich, W. Skorupa, A. Peeva, A. Y. Kuznetsov, J. S. Christensen, and B. G. Svensson, J. Appl. Phys. **101**, 033508 (2007).

[28] J. Slotte, Nucl. Instr. and Meth. in Phys. Res. B **253**, 130 (2006).

[29] D. A. Abdulmalik, P. G. Coleman, H. A. W. El Mubarek, and P. Ashburn, J. Appl. Phys. **102**, 013530 (2007).

[30] J. F. Ziegler, J. P. Biersack, and U. Littmark, The Stopping and Range of Ions in Matter (Pergamon, New York, 1985).

[31] P. J. Simpson, Z. Jenei, P. Asoka-Kumar, R. R. Robison, and M. E. Law, Appl. Phys. Lett. **85**, 1538 (2004).

[32] J. Slotte, M. Rummukainen, F. Tuomisto, V. P. Markevich, A. R. Peaker, C. Jeynes, and R. M. Gwilliam, Phys. Rev. B **78**, 085202 (2008).

[33] D. A. Abdulmalik, P. G. Coleman, N. E. B. Cowern, A. J. Smith, B. J. Sealy, W. Lerch, S. Paul, and F. Cristiano, Appl. Phys. Lett. **89**, 052114 (2006).

[34] S. Dannefaer, J. Phys. C **15**, 599 (1982).

[35] W.Shockley and W.T. Read, Phys. Rev. **87**, 835 (1952).

[36] J.G. Simmons and G.W. Taylor, Phys. Rev. B. **4**, 502 (1971).

[37] N. Zangenberg, J.-J. Goubet, and A. Nylandsted Larsen, Nucl. Instr. Meth. B **186**, 71 (2002).

[38] J.R. Troxell, Sol. State Elec. **26**, 539 (1983).

[39] P. Hazdra and V. Komarnitskyy, Mat. Sci. Eng B **159-160**, 346 (2009).

[40] S. Libertino, J.L. Benton, D.C. Jacobson, D.J. Eaglesham, J.M. Poate, S. Coffa, P. Kringhoj, P.G. Fuochi, and M. Lavalle, Appl. Phys. Lett. **71**, 389 (1997).

[41] V.P. Markevich, A.R. Peaker, S.B. Lastovskii, L.I. Murin, and J.L. Lindström, J. Phys.: Condens. Matter **15**, S2779 (2003).

[42] M. J. Puska, C. Corbel, and R. M. Nieminen, Phys. Rev. B **41**, 9980 (1990).

[43] P. Mascher, S. Dannefaer, and D. Kerr, Phys. Rev. B **40**, 11674 (1989).

[44] C.D. Beling, S. Fung, H.L. Au, C.C. Ling, C.V. Reddy, A.H. Deng, and B.K. Panda, Appl. Surf. Sci. **116**, 121 (1997).

[45] H. Kauppinen, C. Corbel, J. Nissilä, K. Saarinen, and P. Hautojärvi, Phys. Rev. B **57**, 12911 (1998).

[46] A. Kawasuso, M. Hasegawa, M. Suezawa, S. Yamaguchi, and K. Sumino, Jpn. J. Appl. Phys. **34**, 2197 (1995).

[47] www.SRIM.org, (author: J.F. Ziegler).

[48] P.G. Coleman, C.P. Burrows, and A.P. Knights, Appl. Phys. Lett. **80**, 947 (2002).

[49] P.G. Coleman, in Encyclopedia of Applied Spectroscopy, edited by D.L. Andrews (Wiley-VCH, 2009).

[50] N. Daldosso and L. Pavesi, Laser Photonics Rev. **3**, 508 (2009).

[51] J. N. Milgram, J. Wojcik, P. Mascher, and A. P. Knights, Opt. Express **15**, 14679 (2007).

[52] A. P. Knights, J. N. Milgrarn, J. Wojcik, P. Mascher, I. Crowe, B. Sherliker, M. P. Halsall, and R. M. Gwilliam, Phys. Status Soidi. A **206**, 969 (2009).

[53] X. D. Pi, P. G. Coleman, R. Harding, G. Davies, and R. M. Gwilliam, J. Appl. Phys. **12**, 8155 (2005).

[54] D. Comedi, O. H. Y. Zalloum, J. Wojcik, and P. Mascher, IEEE J. Sel. Top.Quantum Electron. **12**, 1561 (2006).

[55] K. Takashina, A. Fujiwara Y. Ono, Y. Takahashi, and Y. Hirayama, Phys. Rev. Lett. **96**, 236801 (2006).

[56] K. Izumi, M. Doken, and H. Ariyoshi, Electron. Lett. **14**, 593 (1978).

[57] T. Ishiyama and M. Nagase, Jpn. J. Appl. Phys., Part 1 **34**, 6019 (1995).

[58] Y. Takahashi, A. Fujiwara, M. Nagase, H. Namatsu, K. Kurihara, K. Iwadate, and K. Murase, Int. J. Electron. **86**, 605 (1999).

Chapter 6

Studies of Other Materials

"Creative work is play. It is free speculation using materials of one's chosen form."

- Stephen Nachmanovitch

While positron spectroscopy has primarily been used to study defects in semiconductor-type devices, it is also a useful technique in other materials as well. In this chapter, insulator-type materials are studied where the positronium formation is enhanced and can be used to investigate the structure of these materials in a unique way. More exotic materials, such as superconductors, have also been studied with the VEPAS technique to reveal how surface defects can be linked to unexplained phenomena.

6.1 Positron and positronium studies of silica aerogel

6.1-I Introduction

Aqueous colloids (suspensions) of gold nanoparticles in water have attracted attention because of applications in photonics technologies such as ultrafast switching, surface-enhanced Raman scattering, and plasmonic sensing.[1] Silica aerogel is a highly porous form of silica glass made of a rigid, open network of tiny intersecting silica strands about 5 nm thick. The average size of the pores between the strands is 40 nm, and over 90% of the total volume is air. The refractive index of aerogel is ~ 1.05 and the optical loss due to Rayleigh scattering can be as low as 0.1 dB/cm at a wavelength of 900 nm.[2]

Gold nanoparticle-implanted aerogels can be incorporated into waveguides using techniques developed by Bath's Centre for Photonics and Photonics Materials (CPPM);[3] [4] the resulting devices are stable with time, as the nanoparticles are 'locked in' by the silica network.

Past positron studies such as those by Hyodo and colleagues have looked at silica aerogel surface and bulk positronium (Ps) interactions using positron age–momentum correlation[5] as well as angular correlation of annihilation radiation, positron lifetime and Doppler broadening.[6] Other studies have used silica aerogel as a Ps formation medium.[7] The study described here uses VEPAS to investigate the gold nanoparticles within the aerogel medium and how they effect positronium formation.

6.1-II Experimental Details

In previous reports, doped aerogels have suffered from nanoparticle aggregation or other limitations. The CPPM group made sol using aqueous gold colloid, resulting in a purple-looking wet gel and aerogel, Fig. 6.1.1 (middle).

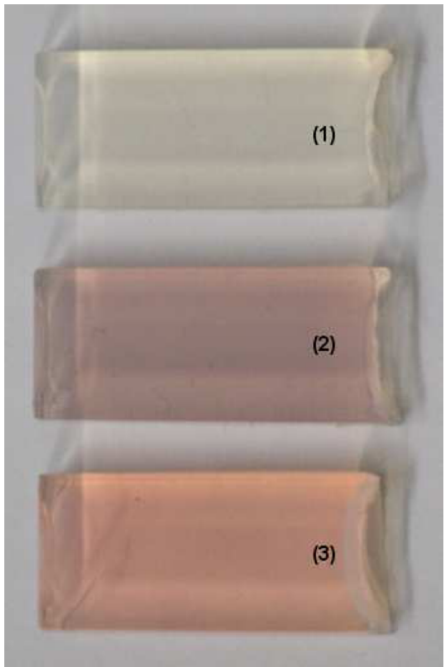

Figure 6.1.1: Aerogel samples: (1) (top) with no nanoparticles: (2) (middle) with clustered nanoparticles: (3) (bottom) with ~ 40nm diameter spherical nanoparticles.

Using TEM it was confirmed that the purple colour is correlated with nanoparticle aggregation due to the presence of methanol. A two-step procedure was developed to stop this in wet gels of the same composition. Using the modified wet gel process prevents aggregation while retaining control over gel time, allowing nanoparticles of diameter ~ 40 nm

to be embedded at various concentrations in aerogel, Fig. 6.1.1 (sample (3), bottom) and Fig. 6.1.2.

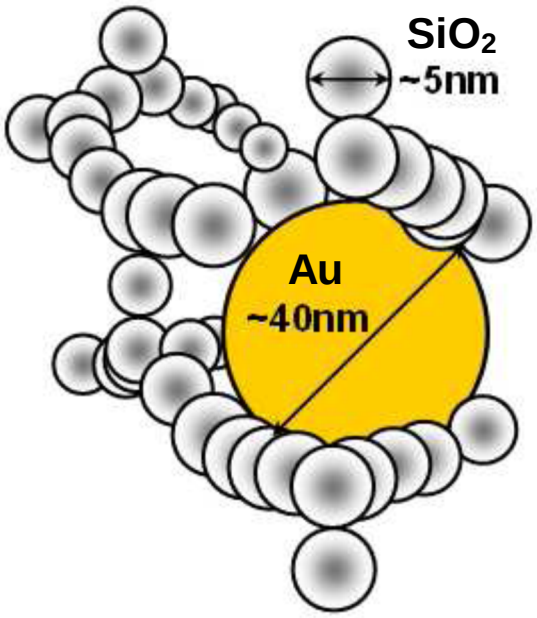

Figure 6.1.2: Aerogel: a rigid open network of tiny intersecting silica strands with air-filled pores between them (on average about 40 nm across). Over 90% of the total volume is air.

The samples used during this experiment were those shown in Fig. 6.1.1, with ~30% gold in (2) and (3). The samples were all initially cleaved in half down their lengths to reveal as clean a surface as possible for the measurements.

6.1-III Data Analysis

To account for drifts in *S* Parameter over time, data were normalised to the average bulk *S* value for sample (1) using the alternating sample method described in Chapter 3.2. Figs. 6.1.3 and 6.1.4 show the difference between the results before and after this procedure.

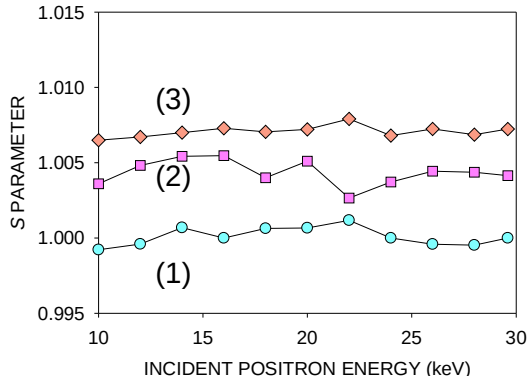

Figure 6.1.3: S parameters for samples (1)-(3) normalised to bulk S value for sample (1).

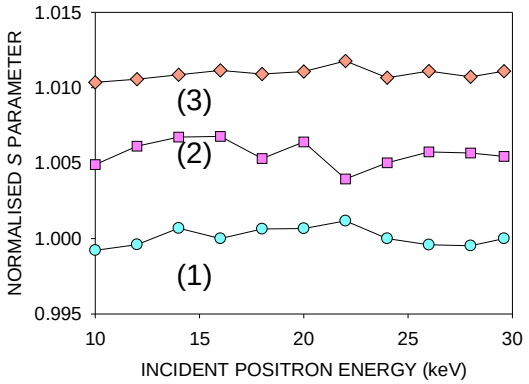

Figure 6.1.4: S Parameter data normalised using the alternating sample method.

The *P:V* ratio was also used to characterise samples by their ortho-positronium (o-Ps) formation. A description of the *P:V* ratio and its correction method can also be found in Chapter 3.4. Fig. 6.1.5 shows the raw *P:V* ratios for the three samples. The corrected ratios in Fig. 6.1.6 show a fourfold increase in sensitivity to o-Ps annihilation between samples 1 and 2. The raw *P:V* for Cz Si had an average *P:V* = 8.4, the corrected ratio was 18.9.

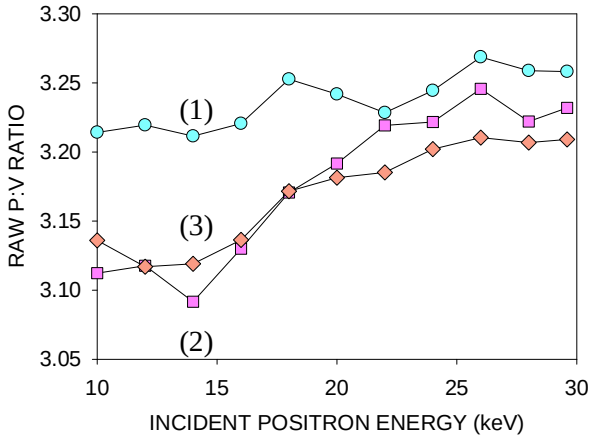

Figure 6.1.5: Raw bulk measurements for P:V ratio for all samples.

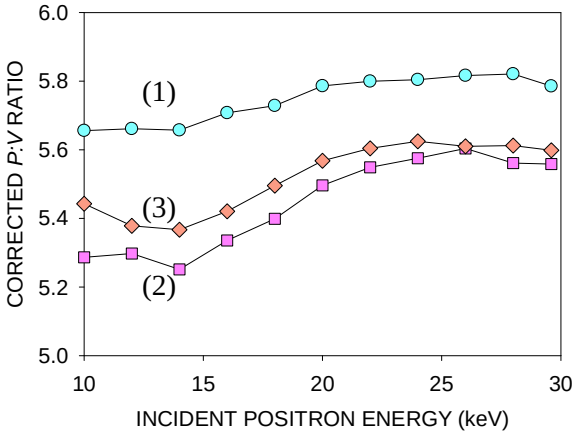

Figure 6.1.6: P:V ratios after correction method was applied.

6.1-IV Results

Charging effects in sample (1) were investigated by consecutively repeating one *S*(*E*) run (*E* = 0.5 to 30 keV) ten times (Fig. 6.1.7).

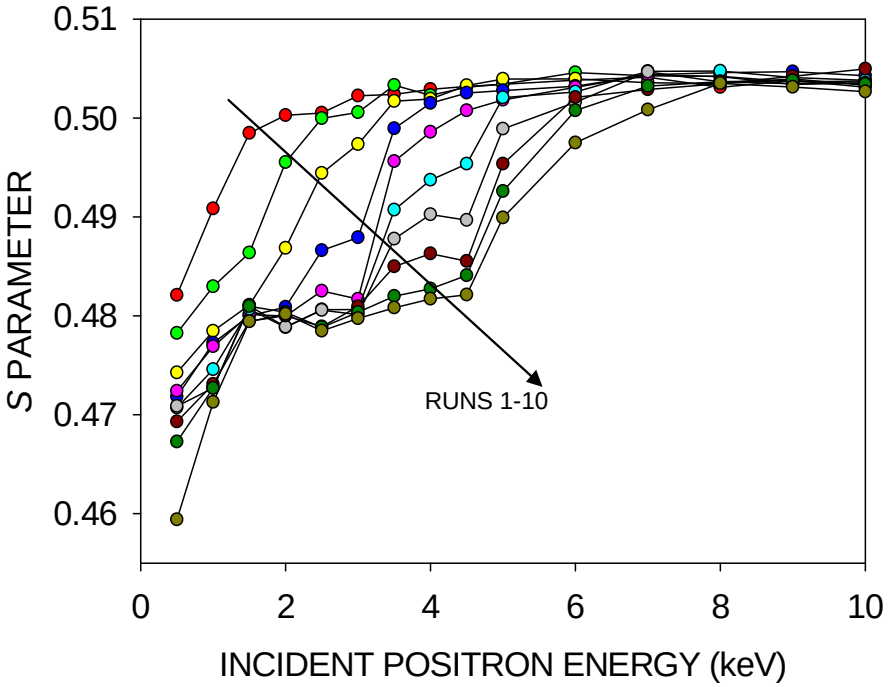

Figure 6.1.7: Repeated S(E) measurements. Each run lasted 12.5 h.

Each run took 12.5 h. The lower *S* parameters at $E < 1.5$ keV are associated with epithermal positron annihilation. Over time the charging effect increased, with the formation of a saturated state in the 1.5–4.5 keV region, shown also in the *S*-*W* plot in Fig. 6.1.8.

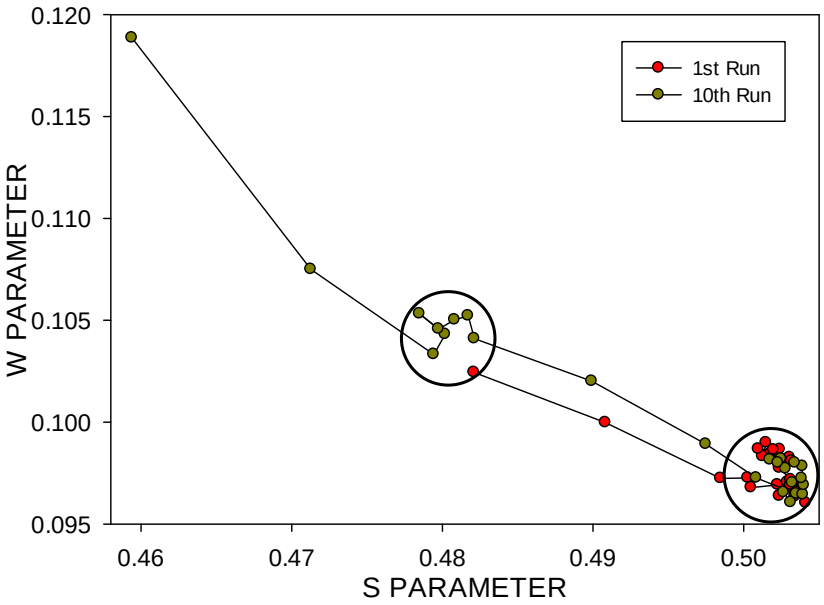

Figure 6.1.8: S-W plots for the first and last runs of Fig.6.1.7.

This effect causes the *P:V* ratio to increase (and o-Ps formation to decrease) dramatically with time in the 1.5–4.5 keV region. The subsurface field appears to be drifting positrons toward the surface at epithermal energies, with a consequently lower Ps formation probability.

Whereas there is a real difference between the normalized *S* Parameters for the three cleaved aerogel samples (Fig. 6.1.4), there is a much smaller difference between corrected *P:V* ratios the two gold samples (Fig. 6.1.6), but there is a difference between the gold and plain silica aerogel sample.

To test whether the gold nanoparticles could be a catalyst for increased o-Ps formation, more samples were obtained with various gold nanoparticle concentrations between 0 and 29% (Fig. 6.1.9).

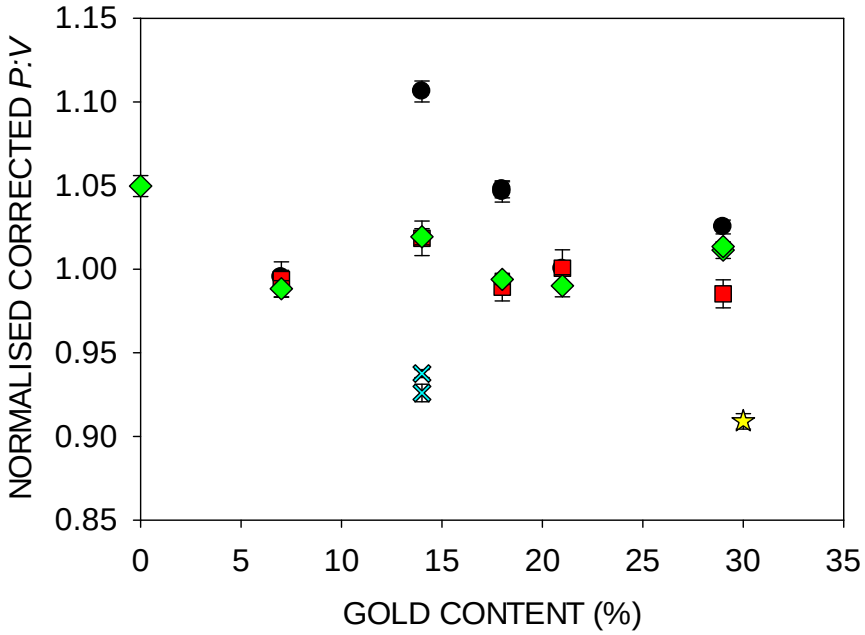

*Figure 6.1.9: Normalized P:V ratios for different concentrations of gold nanoparticles and for different locations on the samples. ● – sample ends; □ - individual runs; ◊ - sample centres; **x** – repeats on sample ends; ☆- cleaved sample.*

The first set of results used the standard normalization method described above. In the second set measurements were made separately at the centre of the samples with no normalization. The third set is identical to the first except that the centres of each sample are measured rather than the ends. The fourth set comprises two repeats of the first measurement of the 14% Au

sample. The fifth set is a data point from normalization run of the original cleaved sample (3). The data point at 0% Au refers to original sample (1).

Some of these results show agreement but there are also points which have differences far outside statistical fluctuations. These data suggest that positrons and Ps are very sensitive to differences in the structure of the silica aerogel itself.

6.1-V Conclusions – Silica Aerogel

Doped silica aerogel was investigated initially to look at the positron response to the gold nanoparticles, the *P:V* ratio being the parameter of choice. Techniques were developed to improve both the sensitivity and reliability of the *P:V* ratio and *S* Parameter. The findings suggest, however, that while *P:V* was sensitive to the presence of the nanoparticles, there is little or no sensitivity to aggregation. Further investigations with different concentrations of gold nanoparticles revealed that the differences and similarities originally found appear to be dependent upon the on the face and lateral part of sample probed by the positrons. The structure of the silica aerogel itself dominates the VEPAS results, and further work may lead to information on aerogel structure of importance to its novel applications in photonics and other fields.

6.2 The effect of vacancies on the microwave surface resistance of niobium revealed by positron annihilation spectroscopy

6.2-I Introduction

The ultra-low electrical resistivity of a superconducting material allows a radio frequency (RF) resonator to obtain an extremely high quality factor, Q. A high Q resonator has very low power dissipated in the cavity to maintain the energy stored. This property can be exploited for a variety of applications, including high-performance particle accelerator structures. Accelerators typically use resonant RF cavities formed from superconducting materials, such as niobium. Electromagnetic fields are excited in the cavity by coupling in an RF source with an antenna. When the RF frequency fed by the antenna is the same as that of a cavity mode,

the resonant fields build to high amplitudes. Charged particles passing through apertures in the cavity are then accelerated by the electric fields and deflected by the magnetic fields.

Instead of remaining ideally constant with increasing RF field, the Q of a superconducting RF niobium cavity exhibits interesting changes above 80 mT - the Q falls sharply; this is called the high field Q-slope (HFQS), or Q-drop.

To understand the reason for this Q-drop the physical changes which occur in near-surface (10-20 nm) niobium during baking must first be understood. Most studies have focused on the presence of a high concentration of interstitial impurities, such as oxygen, in the near-surface region of niobium as a possible reason for the Q-drop at high magnetic fields. In support of this idea, the diffusion constant of O at 120ºC is sufficient for a decrease in O concentration in the first tens of nanometers.[8] However, recent cavity experiments[9] and surface studies[10] have eliminated interstitial oxygen as a likely cause of the HFQS. Recent experimental data has shown that near-surface dislocations, vacancies, and vacancy-hydrogen complexes caused by different treatments are a more likely cause.[11, 12] It is proposed that a 120ºC bake prevents the formation of small nanoscale hydrides (NbH_x), which could cause the Q-drop, by either binding hydrogen with vacancies or removing nucleation centers for hydrides.

The following experiments use positron spectroscopy to look at the near surface region of samples extracted from different treatment/baking/grain size superconducting RF niobium cavities and to determine the structural changes on them caused by mild baking at 120ºC.

6.2-II Experimental Procedure

The effects of two different polishing techniques were investigated with two sets of samples.

The first set was electropolished (EP) whose samples contained cavities of any grain size. The 120ºC bake effect always effectively removes the high field Q-slope in this set, requiring ~48h baking for the full effect. Two curved samples were cut from a real niobium cavity, which was not 120ºC baked. One of them (EP-high) exhibited high RF losses, and one (EP-low) low RF losses. A further curved sample (EP-none) was cut from a region with no RF losses from a 120ºC baked cavity. Two flat samples, baked (EP-b) and unbaked (EP-ub) were

also studied, for which the correlation to the RF performance was much weaker since they were not parts of the real niobium cavity.

The second set was buffered chemically polished (BCP) and contained cavities with either single grain or fine grain sizes with a baked and unbaked sample for each. For the single grain cavities (BCP-SG-b and BCP-SG-ub) baking is always effective and requires less time (~12h) than EP. For the fine grain cavities (BCP-FG-b and BCP-FG-ub) baking is not effective and the high field Q-slope remains.

Samples were measured before, during and after baking at 120ºC in vacuum for 48h. The after baking measurement was done by exposing the baked sample to air and remeasuring at room temperature. The importance of the exposure to air is that it is known that the performance of the sample in RF does not change (decrease) due to air exposure at RT. The reason is that there may be slight changes in the oxide structure due to the 120ºC bake but these changes are reversed by the air exposure while the benefit in the RF performance is maintained. Samples are exposed to air to reduce seeing any irrelevant effects.
The first 40 nm in each sample is probed by the positrons with incident energies up to ~4 keV. The full energy range up to 30 keV probes up to ~1 μm in Nb.

6.2-III Results and Discussion

For interpretation of the following results it is important to consider the vacancy-hydrogen interaction. It has been discovered[13] that, in the presence of hydrogen, the vacancy formation energy in many metals is strongly lowered. The phenomenon was named “superabundant vacancies" (SAV) and found in many M-H systems.[14, 15] V-H complexes were also observed in large concentrations in H-loaded niobium.[16, 17] Theoretical calculations[18] show that the number *n* of hydrogen atoms trapped at each of the vacancies in niobium may range from one to six and the *S* parameter response in Doppler broadening PAS of V-*n*H complexes is a function of *n*. Higher *n* corresponds to lower *S* due to the lower effective open volume available to positrons. Furthermore, V-H complexes can be introduced into Nb by diffusion from the surface at elevated temperatures.[19] Such diffusion was found to happen via “fast" and “slow" processes, believed to be due to diffusion along dislocations and to bulk diffusion.

Electropolished Samples

Fig. 6.2.1 shows sample EP-ub before and during baking. Four runs were taken over the first 19h with each energy point running for 950s. The effect of baking appears to be almost immediate. Another run was taken towards the end of the baking session (not shown) which is again identical to baking data below.

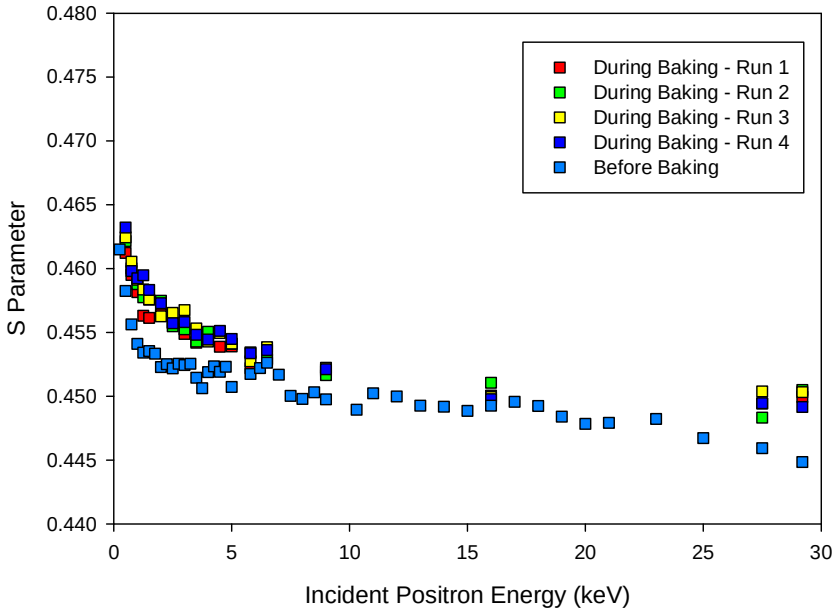

Figure 6.2.1: Sample EP-ub before and during baking. Each data point during baking was collected for 950s.

Since the effects of baking are immediate and sustained only one data set will be taken during the course of baking for future results.

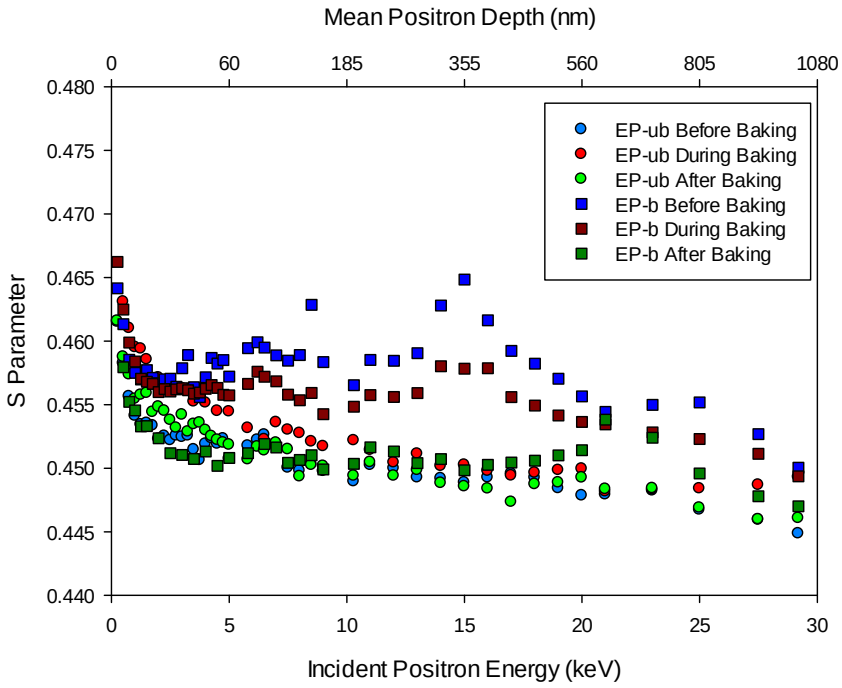

Figure 6.2.2: Samples EP-ub and EP-b - before, during and after baking.

Unusual peaks appear at 8.5 and 15 keV in sample EP-b, seen in Fig. 6.2.2. These abrupt features are not very trapping-like – the response does not extend far either side of the feature – but have a high *S* response usually associated with open volume defects. Although they do not appear real at first sight, these peaks in *S*(*E*) were reproducible; further, the process of baking reduces the positron response to them and after baking they appear to be completely removed. Their source is unknown but may not be directly relevant to the current study of the subsurface region.

Looking at the first 40 nm, the effect of baking in sample EP-ub raises the *S* parameter in this region. After baking and air exposure the *S* then falls to a response similar to that before baking. In sample EP-b, however, baking does little to effect the *S* parameter. It is only after being let up to air and re-measured that the *S* falls in a similar way to EP-ub. Further insight into this changing *S* parameter can be seen in *S*-*W* plots and, later, spectra ratios.

Fig. 6.2.4 uses both *S* and *W* data to form a state map. Straight lines usually join two states as the percentage of the positron implantation profile overlapping with each change with implantation energy. Key points have their corresponding energies attached.

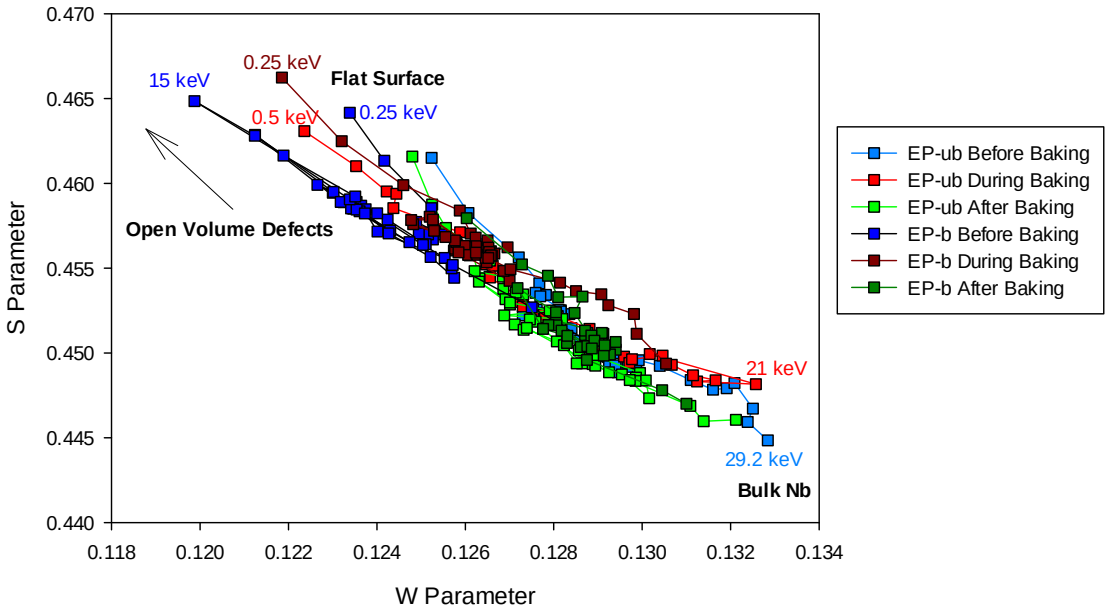

Figure 6.2.4: S-W plot for samples EP-ub and EP-b.

The first 4 or so points, up to ~5 nm deep, correspond to a surface response. The lower near-surface *S* response after baking, particularly in the EP-b sample, still lies on the bulk Nb-open volume in Nb *S*-*W* line implying that the same type of defects exist but either fewer of them exist or there is just a lesser positron response to them. In sample EP-b the position of the main cluster of points shifts towards a purer form of Nb after baking and air exposure. EP-ub has little to no change in the bulk response after baking.

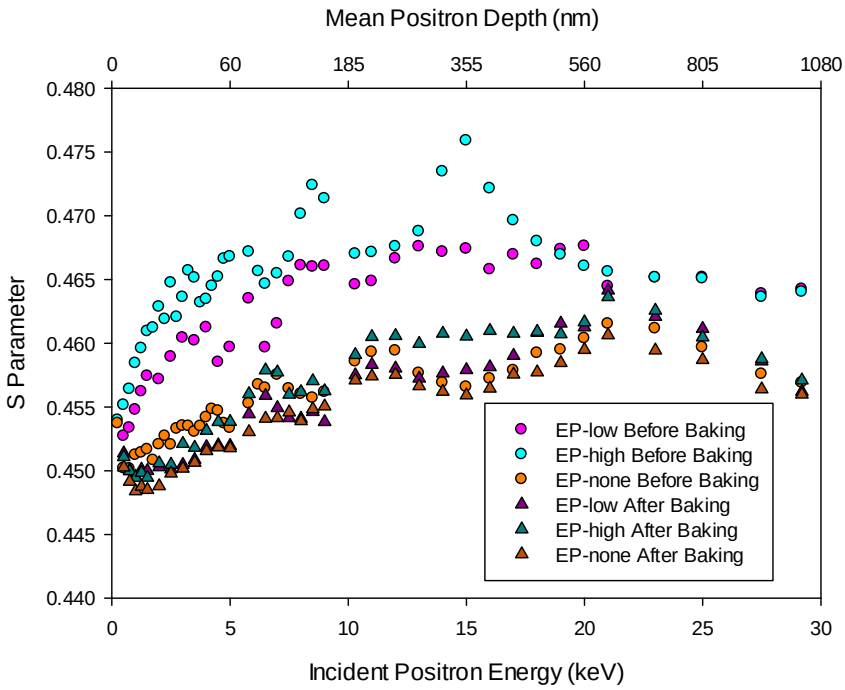

Figure 6.2.3: Samples EP-low, EP-high and EP-none – before and after baking.

The shapes of the *S*-*E* curves in Fig. 6.2.3 differ to those in Figs. 6.2.1 and 6.2.2 due to the different surfaces. Again, before baking, peaks appear in the same places in sample EP-high as in sample EP-b. The process of baking removes these features. There is a distinct correlation between RF losses and positron diffusion length, *L*. Before baking, *L* in the first 40 nm is shortest in the sample with the highest RF losses (EP-high) and longest in the no RF losses sample (EP-none). Between 23 and 30 keV the bulk *S* parameter of samples EP-low and EP-high is also much higher than in EP-none. After baking and air exposure, all three samples have *S*(*E*) curves that resemble sample EP-none, including the high energy points, which had been previously baked.

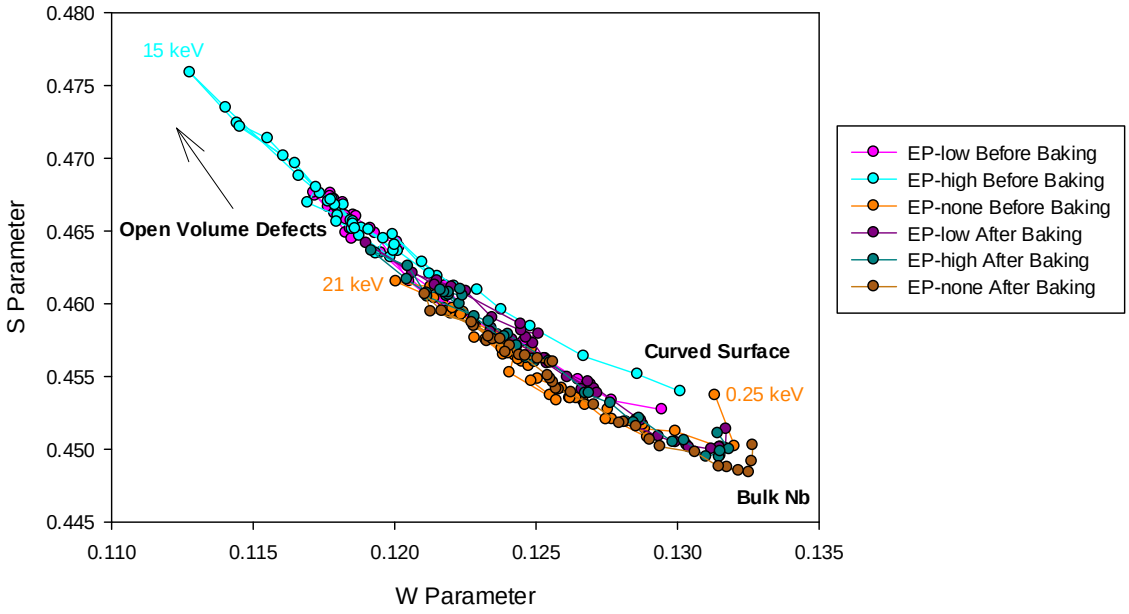

Figure 6.2.5: S-W plot for samples EP-low, EP-high and EP-none.

S-*W* curves reveal that the surface in the EP-high sample contains more open-volume defects than in the other samples. It is these defects that could be giving rise to the RF losses. All samples in Fig. 6.2.5 show some improvement with baking, containing fewer open volume defects and a less defective Nb response.

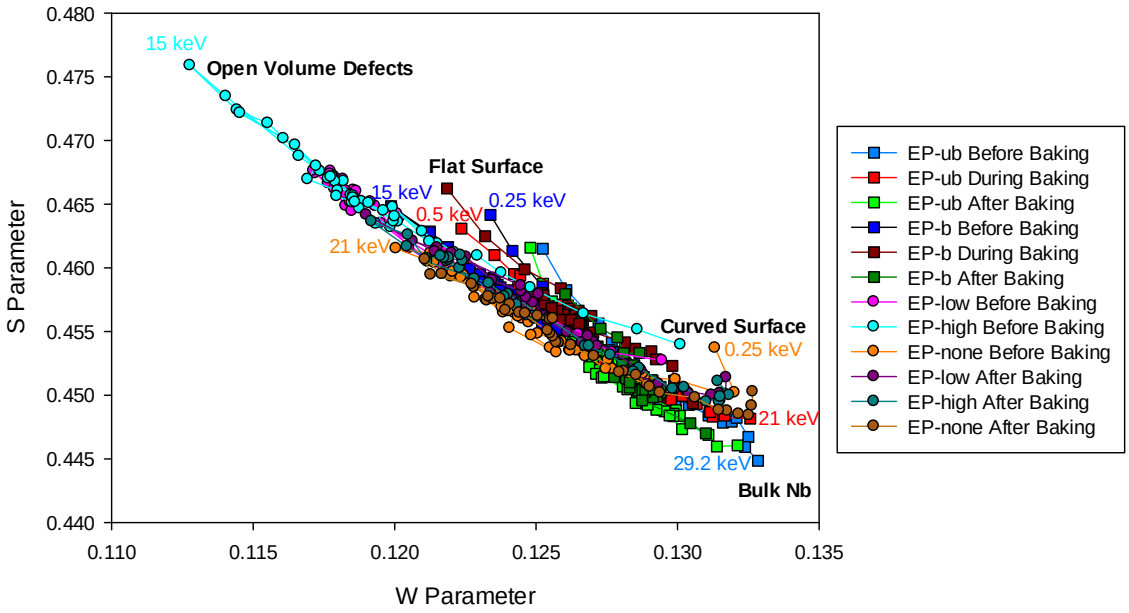

Figure 6.2.6: S-W plot for all EP samples.

Spectra were taken at 3 keV for a maximum response to the first 40 nm. They were then divided by a reference spectrum (for Si) to reveal any differences in the high momentum content associated with different electronic environments.

The samples all show peaks at ~514.4 keV, shown in Fig. 6.2.7. An oxygen response has a peak at 514.6 keV. It is unclear whether this response is due to an oxygen presence or if it is an Nb-related response. The response increases after baking.

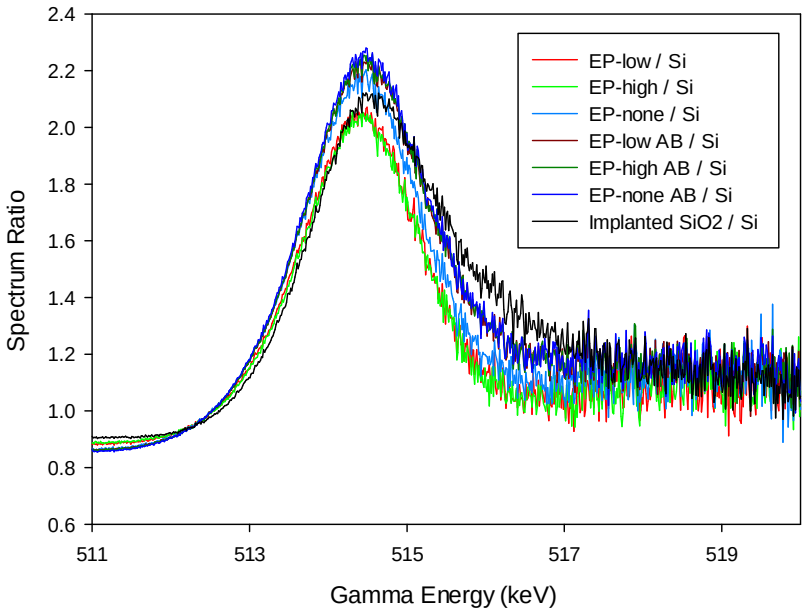

Figure 6.2.7: Spectra ratios for samples EP-low, EP-high and EP-none (divided by c-Si), before and after (AB) baking. Implanted SiO2 is shown for an oxygen response.

To determine whether the peaks in Fig. 6.2.7 are oxygen- or Nb- related, a reference spectrum for pure Nb is needed. In the absence of a pure Nb sample a spectrum for sample EP-ub, after annealing, was measured for E = 30keV. The ratios are shown in Fig. 6.2.8:

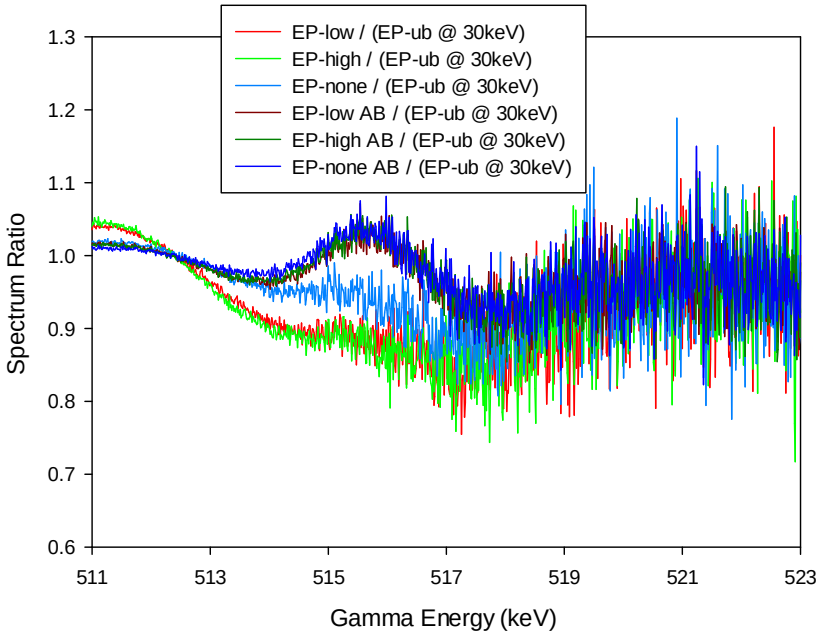

Figure 6.2.8: Spectra ratios for samples EP-low, EP-high and EP-none (divided by spectrum taken of sample EP-ub (after baking) at 30 keV).

The ratios show a combination of peaks at ~ 515.5 keV and a broad dip centred at ~ 517.5 keV. While the latter could be related to vacancy-type defects, the source of the former is still open to interpretation. However, these measurements (Fig. 6.2.8) may be flawed if the reference EP-ub sample is not defect-free pure Nb, and thus re-measurement using such a sample might be useful.

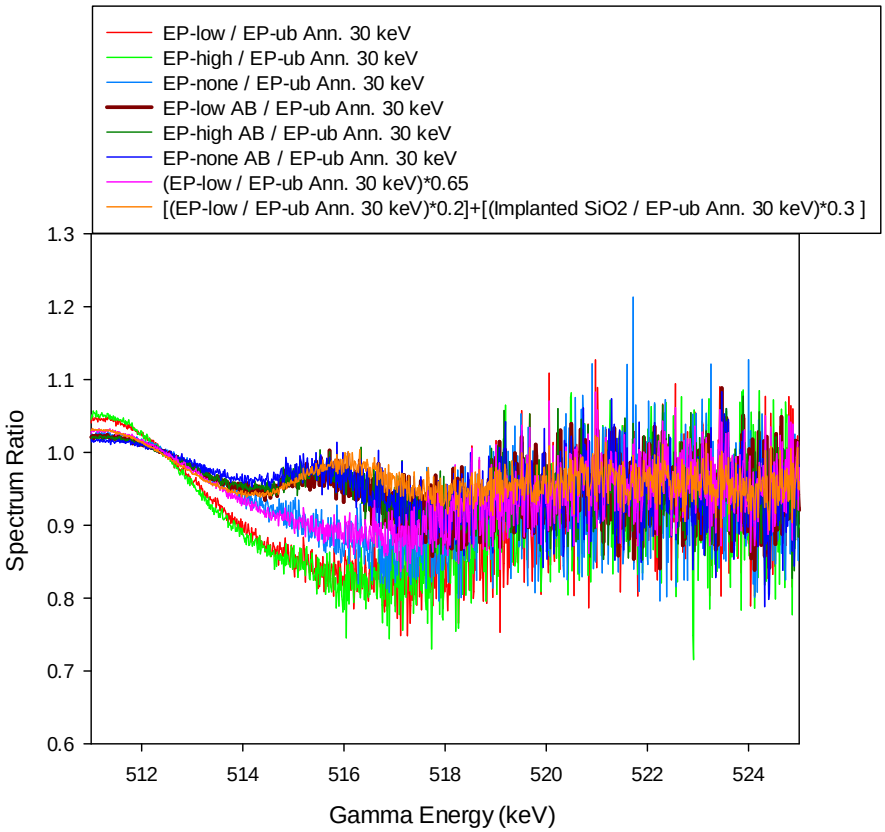

Figure 6.2.9: Spectra ratios for samples EP-low, EP-high and EP-none, before and after baking. Spectra are divided by a spectrum taken of sample EP-ub (after baking and annealing at 1000ºC for 2h) at 30 keV. Includes combination fits of sample EP-low and implanted SiO_2 spectra for sample EP-none.

To determine the nature of the defects in samples EP-low, EP-high and EP-none before and after baking spectra ratios were taken of Nb (sample EP-ub @ 30 keV - ann. at 1000ºC for 2 hours) and implanted SiO_2 (for an oxygen response). The spectrum for sample EP-low was used as an open-volume response. All spectra were divided by the annealed EP-ub spectrum which is assumed now to be defect-free Nb.

Linear combinations of spectra have been seen before to be an accurate way to estimate relative concentrations of defects and elemental types.[20] Sample EP-none before baking can

be fit with ~65% of sample EP-low's (or EP-high's) spectrum. This means that ~65% of the concentration of these open-volume defects found in EP-low (or EP-high) are found in EP-none. The baked samples can be fit with a combination that suggests ~20% of sample EP-low's (or EP-high's) spectrum [open-volume response] and ~30% of implanted SiO_2's spectrum [oxygen response].

In the EP samples the higher $S(E)$ before baking is attributed to open-volume defects introduced by the EP treatment itself. As a result of baking, the S parameter at all E up to 30 keV is decreased, which may be explained by either elimination or transformation of these pre-existing defects. Under the assumption that EP-introduced defects are of the V-nH type, the transformation may correspond to the increase of n, which will lead to the decrease in S. V-nH can also be introduced by surface diffusion but is difficult to observe as these defects are nucleated in the H-rich layer and therefore may be of higher n value with lower S. Still, the change in the shape of $S(E)$ is consistent with the presence of this surface process since the relative change in S parameter is depth-dependent.

Buffered Chemically Polished Samples

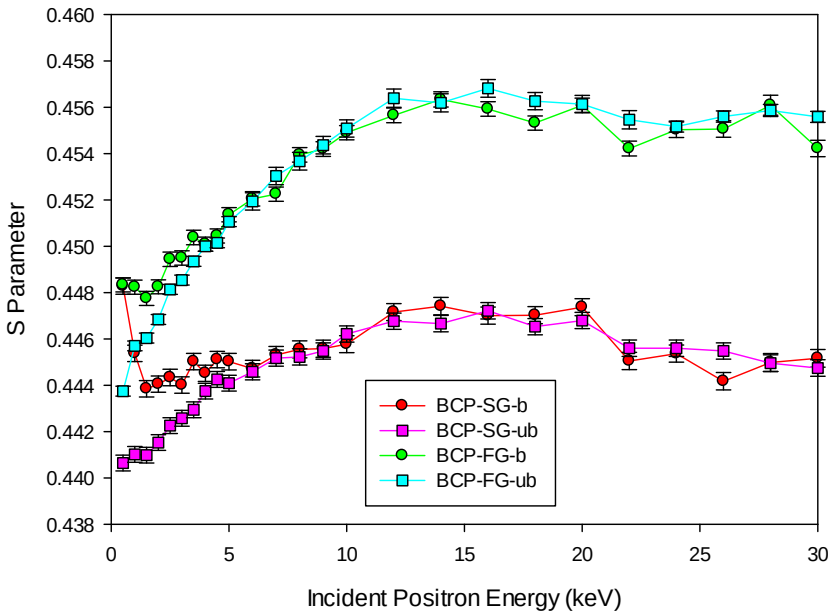

Figure 6.2.10: S(E) data for all BCP samples as-received.

Samples “BCP-SG-b” and “BCP-FG-b” show a very similar surface response up to ~1.5 keV (= ~9 nm average positron implantation depth). This response is not seen in the other two samples and appears to be the only change caused by baking at 120ºC.

The lower bulk *S* Parameter for the single grain samples show that there are fewer sub-surface and bulk defects than in the fine grain samples and all of the EP samples. This could be why baking is always effective for the single grain cavities and requires less time (~12h) than EP. For the fine grain cavities baking is not effective and the high field Q-slope remains, this could be because of the higher initial defect concentration due to grain boundaries and baking is not sufficient to remove them.

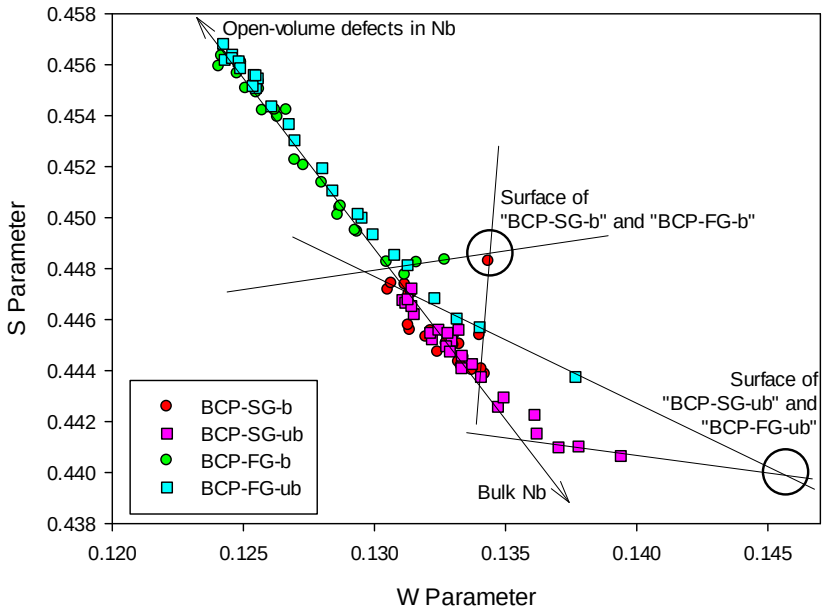

Figure 6.2.11: S-W data for all BCP samples as-received.

Plotted in the *S*-*W* format in Fig. 6.2.11, it can be easily seen that there are two different surface states depending on whether the sample has been baked or not. The 1.5 – 5 keV increase *S* response seen in Fig. 6.2.10 lies on the (‘pure Nb’)-(‘defected Nb’) line suggesting a higher concentration of open-volume defects near the surface formed after baking.

Near-surface hydrogen segregation has been experimentally observed[21, 22] on similar samples. Hence, V-H formation should be energetically favourable if kinetics allow. It is therefore plausible that the *S* parameter increase at $E \leq 4$ keV after baking in the BCP samples can be attributed to V-H complexes introduced by diffusion from the surface.

6.2-IV Conclusions – Defects in Niobium

The superconducting surface resistance of the investigated samples strongly correlates with the shape of the $S(E)$ curve. The presence of a near-surface layer rich in V-type defects of a particular kind, arguably V-H complexes, leads to the absence of a strong rf dissipation at high magnetic fields. Doping of a thin surface layer of ~ 50 nm with stable V-H complexes may therefore be a major mechanism behind mild baking.

It has recently[23] been proposed that free interstitial hydrogen segregated near the surface can form niobium hydrides upon cooldown to typical cavity operating temperatures below 4.4 K. Such proximity-coupled nanohydrides may be major field-dependent contributors to the surface resistance of niobium. The findings in this study suggest that the benefit of the 120ºC baking effect may come from the trapping of interstitial hydrogen by vacancies, suppressing niobium hydride formation. Impurity trapping has been shown to prevent the formation of large hydrides in cavities made out of dirty, low residual resistivity ratio niobium.[24] Similarly, trapping all near-surface H by vacancies may explain the elimination of strong high field losses (high field Q-slope) in cavities by mild baking.

Finally, these results may help to explain the superiority of EP over BCP treated fine grain niobium cavities if the nanohydride origin of the high field degradation (Q-slope) is assumed. Unlike BCP, in EP-treated niobium, vacancy-like defects are introduced by the EP process itself. Therefore some fraction of near-surface interstitial H atoms may be already trapped, with the net result of less H available for precipitation upon cooldown. This will lead to smaller average hydride size in EP with a higher proximity breakdown field, which may explain the observed higher field onset of the high field losses. The superior effectiveness of mild baking on EP surfaces may stem from the availability of vacancy-type defects to trap more hydrogen which, in the BCP case, have all to be introduced by diffusion.

[1] R. F. Souza, M. A. R. C. Alencar, E. C. da Silva, M. R. Meneghetti, and J. M. Hickmann, Appl. Phys. Lett. **92**, 201902 (2008).

[2] M. D. W. Grogan, M. D. Rollings, L. M. Xiao, W. J. Wadsworth, R. England, S. A. Maier, and T. A. Birks, Quantum Electronics and Laser Science, OSA Technical Digest (CD), JThE21 (2010).

[3] M. D. W. Grogan L. Xiao and S. G. Leon-Saval et al., Opt. Lett. **34**, 2724 (2009).

[4] M. D. W. Grogan, S. G. Leon-Saval, R. Williams, R. England, and T. A. Birks, CLEO, OSA Technical Digest (CD), CMW3 (2009).

[5] N. Suzuki, T. Oonishi, and T. Hyodo et al, Appl. Phys. A **74**, 791 (2002).

[6] H. Saito and T. Hyodo, Phys. Rev. B **60**, 11070 (1999).

[7] Y. Nagashima, Y. Morinaka, and T. Kurihara et al, Phys. Rev. B **58**, 12676 (1998).

[8] G. Ciovati, Appl. Phys. Lett. **89**, 022507 (2006).

[9] G. Eremeev, PhD Thesis Cornell University (2008).

[10] A Romanenko, PhD Thesis Cornell University (2009).

[11] A. Romanenko and H. Padamsee, Supercond. Sci. Technol. **23**, 045008 (2010).

[12] B. Visentin, M. F. Barthe, V. Moineau, and P. Desgardin, Phys. Rev. ST Accel. Beams **13**, 052002 (2010).

[13] Y. Fukai and N. Okuma, Phys. Rev. Lett. **73**, 1640 (1994).

[14] Y. Fukai, The Metal-Hydrogen System (Springer, Berlin-Heidelberg, 2005).

[15] Y. Fukai, J. Alloys Compd. **356-357**, 263 (2003).

[16] J. Cizek, I. Prochazka, F. Becvar, R. Kuzel, M. Cieslar, G. Brauer, W. Anwand, R. Kirchheim, and A. Pundt, Phys. Rev. B **69**, 224106 (2004).

[17] J. Cizek, I. Prochazka, R. Kuzel, F. Becvar, M. Cieslar, G. Brauer, W. Anwand, R. Kirchheim, and A. Pundt, J. Alloys Compd. **404-406**, 580 (2005).

[18] J. Cizek, I. Prochazka, S. Danis, G. Brauer, W. Anwand, R. Gemma, E. Nikitin, R. Kirchheim, A. Pundt, and R. Islamgaliev, Phys. Rev. B **79**, 054108 (2009).

[19] H. Koike, Y. Shizuku, A. Yazaki, and Y. Fukai, J. Phys. Cond. Matt. **16**, 1335 (2004).

[20] C. J. Edwardson, P.G. Coleman, H. A. W. El Mubarek, and A. S. Gandy, J. Appl. Phys. **111**, 073510 (2012).

[21] T. Tajima, R. L. Edwards, F. L. Krawczyk, J. Liu, D. L. Schrage, A. H. Shapiro, J. R. Tesmer, C. J. Wetteland, and R. L. Geng, in Proceedings of the 11th Workshop on RF Superconductivity (2003).

[22] A. Romanenko and L. V. Goncharova, Supercond. Sci. Tech. **24**, 105017 (2011).

[23] A. Romanenko, F. Barkov, L. D. Cooley, and A. Grassellino, Supercond. Sci. Tech. **26**, 035003 (2013).

[24] K. Saito and P. Kneisel, in Proceedings of the 5th Workshop on RF Superconductivity (DESY, Hamburg, Germany, 1991) pp. 665-679.

Chapter 7

Summary and Conclusions

"People don't like to think, if one thinks, one must reach conclusions.
Conclusions are not always pleasant."

- Helen Keller

The Doppler broadening of annihilation radiation (DBAR) technique has been used and its methods and parameters have been developed and applied to the study of oxide films, semiconductor structures and unique materials.

Normalisation methods for the DBAR parameters *S* and *W* have been developed, allowing for direct comparisons of the results for different samples taken over long periods of time. This was done by deflecting the positron beam using trim coils, enabling two samples to be measured almost simultaneously, one being a standard reference sample.

The evaluation of the *P*:*V* ratio has been improved via a correction method that produced a fourfold increase in sensitivity to o-Ps annihilation. Background and contributions from non-Ps sources were removed to leave a response due only to positronium.

The spectrum ratio curve technique was improved and developed to investigate the chemical composition of the environment surrounding a positron-trapping defect. It was found that the heights of the ratio curve peaks contain information about the strength of the response. The ratios of the sample peak height to a corresponding element or defect-type peak height are equivalent to the percentage of that particular element or defect contained within the sample. By fitting to multiple-element and/or defect-type responses a more detailed picture of the vacancy complexes could be found in the region of interest. This technique was found to rely on the positron affinity to different vacancy types; for example, during the work described in this thesis it was found that positrons have the same affinity to defects surrounded by Si or by Ge.

Beam-based Doppler broadening spectroscopy, usually called variable-energy positron annihilation spectroscopy (VEPAS) was used as a probe of oxide film and film/substrate interface characteristics. Different film growth methods were found to play a significant role in defining the features of films and their interfaces. For example, thermal ALD creates an $AlO_x/SiO_x/Si$ interface with a high negative charge density in the AlO_x within ~1 nm of the interface, inducing positive charge in the Si next to the interface. The positive charge reduced positron diffusion into the oxides and increases annihilation in the Si. Positrons simulated hole diffusion here to show how this pacification reduced surface recombination, improving solar cell efficiency. In TiO_2 films it was found that electroluminescence (EL) efficiency increases with film thickness and after annealing in vacuum or hydrogen. The presence of oxygen vacancies, readily probed by positrons, was linked to EL efficiency. $SrTiO_3$ film growth parameters were assessed to obtain a film of the optimum structural quality.

Vacancies have a profound effect on the properties of semiconductor-type devices. In this thesis a range of different structures and the effects of implantation have been investigated. The recombination behaviour of vacancies and interstitials was found to be different in Si and SOI structures; damage could survive longer in the Si layer of the SOI samples compared to the Si samples. Divacancies can survive more readily in chain-implanted samples than in single-shot-implanted samples as recombination of vacancies and interstitials is reduced. The depth profile of implanted ions in SiGe was found to have two regions, one of undecorated vacancies and fluorine-vacancy (FV) complexes and one of just FV complexes, independent of sample structure. Lifetimes and populations of different charge states in V_2 in a biased Si diode have been estimated. Passivation of defects at a Si-nc surface has been observed, an effect which is then linked to a large increase in the luminescence yield. It was identified that there are significant structural differences between the two Si/SiO_2 interfaces in a quantum well.

VEPAS has been found to be useful in studying other materials. Silica aerogel, as an insulator, enhanced positronium formation so the improved *P*:*V* ratio parameter was used. It was found that while the *P*:*V* ratio was sensitive to doped nanoparticles, the structure of the aerogel itself dominated the response. The superconducting material niobium exhibits a currently unexplained phenomenon at high magnetic fields, reduced just by baking at 120ºC. It was revealed that H-trapping via vacancies may be the cause of this reduction. It was also discovered how different surface treatments can introduce defects which in turn trap H.

It is clear that variations and developments of the basic VEPAS technique hold continuing promise for the characterisation of a wide range of materials of scientific and technological interest and importance.